INVESTIGATION OF THE SURFACE MECHANICAL PROPERTIES OF SINGLE CRYSTAL ZnO BY NANOINDENTATION

By

RUDY GHISLENI

Bachelor of Science

Politecnico di Milano

Milano, Italy

1998

Submitted to the Faculty of the
Graduate College of the
Oklahoma State University
in partial fulfillment of
the requirements for
the Degree of
MASTER OF SCIENCE
August, 2001

INVESTIGATION OF THE SURFACE

MECHANICAL PROPERTIES OF

SINGLE CRYSTAL ZnO BY

NANOINDENTATION

Thesis Approved:

Don A. Gregg

Thesis Adviser

Dean of the Graduate College

ACKNOWLEDGEMENTS

I would like to thank my adviser Professor Don A. Lucca, a dedicated professor that taught me the fundamentals so important to original scientific thought, and a gentleman that gained my trust and never left me alone during this study. I wish to thanks him for his guidance, support, patience and encouragement. I would also like to thank my committee members, Prof. Afshin J. Ghajar and Prof. Eduardo A. Misawa, and Prof. Peter M. Moretti for their valuable comments and suggestions.

The financial support of the National Science Foundation, Division of Design, Manufacture and Industrial Innovation, and the Oklahoma Center for the Advancement of Science and Technology (OCAST) is gratefully acknowledged. I would like to thank Mr. Gene Cantwell of Eagle-Picher Technologies for his assistance and support.

I would like to thank my colleagues, Mr. Matthew J. Klopfstein, and Mr. David W. Hamby for all their help and valuable suggestions.

Un ringraziamento particolare va ai miei genitori, papá Mauro e mamma Lory, per il costante supporto ed incoraggiamento mostratomi durante questi due anni lontano da casa. I loro insegnamenti di vita mi hanno consentito di raggiungere questo traguardo e di realizzarmi come uomo. A loro dunque dedico questo mio lavoro.

Per finire vorrei ringraziare Marie, compagna insostituibile, per avermi incoraggiato nei momenti difficili incontrati durante questi due anni.

TABLE OF CONTENTS

LIST OF TABLES

LIST OF FIGURES

NOMENCLATURE

a	distance between slip planes
a	lattice parameter
a	radius of contact circle
A	projected area
AFM	atomic force microscopy
b	Burgers vector
b	distance between atoms in the slip direction
c	lattice parameter
c_{ij}	elastic moduli
c_{ij}	Schmid factors
C_f	machine compliance
C_s	sample compliance
C_{tot}	total compliance
E	elastic modulus
E_g	band gap energy
E_r	reduced modulus
EFC	electrostatic force constant
G	shear modulus
h	elastic displacement
h_c	contact depth

h_{crit}	critical depth
h_f	final depth
h_{max}	maximum depth
h_p	width of the pop-in
H	hardness
K_f	machine stiffness
LED	light emitting diode
LEED	low energy electron diffraction
n	unit normal vector normal to the slip plane
p	pressure applied by the indenter
p_o	maximum pressure under the indenter
P	load applied to the indenter
P_{crit}	critical load
P_{max}	maximum load applied to the indenter
PL	photoluminescence
PPE	photo-plastic effect
r	radial coordinate
r	radius of a dislocation loop
r_c	critical radius for a dislocation loop
r_o	dislocation core radius
R	radius of the indenter
R^*	upper limit of the stress field integration

R_{rms}	roughness (root mean square)
s_{ij}	compliance moduli
s	slip direction
S	stiffness
SCVT	seeded chemical vapor transport
TEM	transmission electron microscopy
V_{CP}	potential of the center plate
UHV	ultrahigh vacuum
UV	ultraviolet
XPD	photoelectron diffraction
XTEM	cross-sectional transmission electron microscopy
ρ	distance from the point where the load is applied and a arbitrary point
σ_{ij}	components of stress
σ^*_{ij}	components of stress solution for the Boussinesq problem
τ_{crit}	critical shear stress
τ_{max}	maximum shear stress
τ_p	Peierls Nabarro stress
τ_r	resolved shear stress
τ_{theo}	theoretical shear strength
ν	Poisson's ratio

Chapter 1

Introduction

1.1 Motivation for the Present Study

The very recent availability of high quality bulk single crystal ZnO has the potential to make a significant impact on the development of short wavelength (blue/UV) LEDs and lasers. One of the major limitations to producing the needed epitaxial-ready substrates however, is subsurface damage introduced by final finishing. Development of fundamental understanding of the surface mechanical properties of this unique material may enable progress towards the creation of final finishing techniques capable of minimizing the subsurface damage. However, a basic understanding of the mechanical response of ZnO to loading does not exist, and little has been reported on its near surface mechanical properties. In the present work, the near surface mechanical response of single crystal ZnO has been investigated by nanoindentation.

1.2 Objectives

The objectives of this work are: 1) characterization of the surface mechanical properties of hardness and elastic modulus for the four principal planes of ZnO, i.e., (0001), $(000\bar{1})$, $(10\bar{1}0)$ and $(11\bar{2}0)$, 2) evaluation of the possible differences between

the Zn-terminated and O-terminated polar faces, 3) examination of the occurrence of "pop-in" and the onset of plasticity for the principal planes studied.

1.3 Approach

At first, the differences in the surface mechanical properties between the polar faces were investigated. The study of the mechanical properties was then extended to the prismatic planes, i.e., $(10\bar{1}0)$ and $(11\bar{2}0)$ planes. To determine the critical resolved shear stress, the critical conditions for the occurrence of pop-in on all four principal planes indented was measured. Along with the estimates made for the critical resolved shear stress, a prediction of the likely active slip systems at the onset of plasticity was reported.

Chapter 2

Literature Review

2.1 ZnO

ZnO is the material investigated in this study. It is a II-VI wide band gap semiconductor (E_g=3.3 eV at room temperature [1]), with a hexagonal wurtzite structure shown in Fig. 2-1. Polycrystalline ZnO has been used for a variety of applications, i.e., ceramics, piezoelectric transducers, chemical sensors, varistors, phosphors, transparent conducting films, thyristors, catalysis, optical coatings and photovoltaics [2]. It has also found application in flat panel displays, solar cells, surface acoustic wave (SAW) devices and oxygen gas sensors [3]. Recent success in producing high quality single crystal ZnO has opened the possibility to produce blue and UV light emitters and high temperature, high-power transistors [4].

Whereas GaN-based devices capable of producing blue and UV light are already in use, ZnO may serve as an excellent alternative due to its many advantages over GaN. For example, ZnO has an higher exciton binding energy (60 meV) when compared to GaN (28 meV), and a higher optical gain (300 cm^{-1}) compared to GaN (100 cm^{-1}) [5]. A result of the large binding energy is that excitons are stable at high temperature (at or above room temperature) which is important for nonlinear optical effects [6]. Recently, room temperature optically pumped lasing of ZnO thin films has

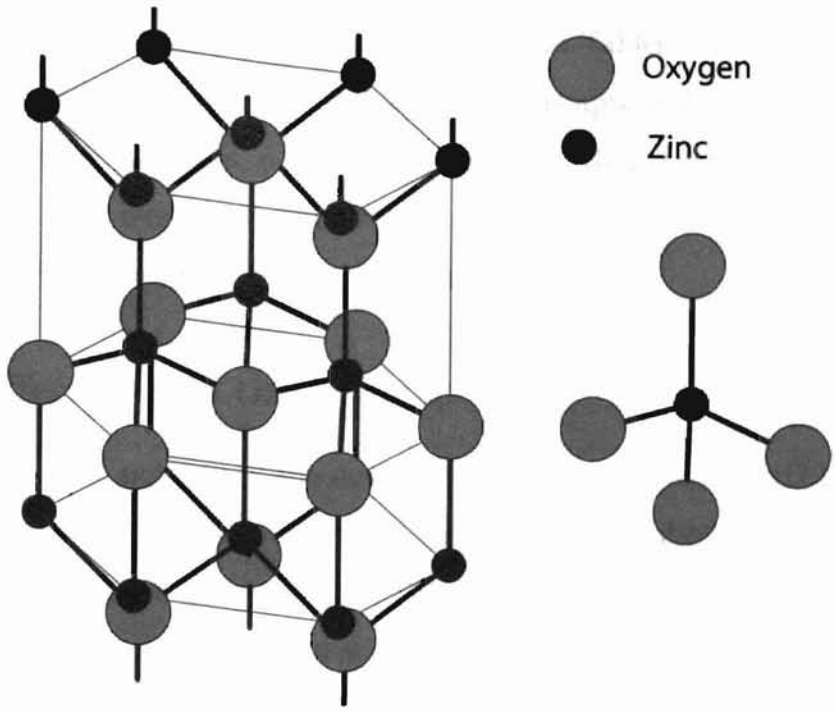

Figure 2-1: ZnO wurtzite structure

been obtained [7][8]. This result showed that the laser emission threshold intensity for ZnO compares favorably with GaN [7]. The lasing threshold at room temperature for ZnO ranges from 40-240 kW/cm^2 whereas for GaN it is greater than 400 kW/cm^2 [9]. As a results of its hardness (ZnO is one of the hardest materials in the II-VI compound family) degradation of the material due to the generation of dislocations during device operation is thought to be minimal [10]. With its large bond strength, ZnO also ensures a large damage threshold for laser irradiation [11].

As mentioned ZnO has the potential to make a significant impact on the development of short wavelength (blue/UV) LEDs and lasers, but at present one of the major limitations to its success is the inability to produce epitaxy-ready substrates due to introduction of subsurface damage by final finishing.

2.1.1 Characteristics

The principal characteristics of ZnO are tabulated in Tables 2.1, 2.2, 2.3 and 2.4.In Table 2.3 the value of s_{44} reported by Bateman [19] is apparently in error and should be 2.357 $Mbar^{-1}$.It has been reported by Jaffe [21] that ZnO undergoes a phase transformation from wurtzite to rocksalt structure at a pressure between 9-9.5 GPa as experimentally determined and 8.57 GPa as calculated.

2.1.2 Differences in the polar faces

The crystallographic polarity of the noncentrosymmetric material ZnO has been determined by several techniques including the rapid x-ray absorption edge method [22], low energy electron diffraction (LEED) [23], photoelectron diffraction (XPD) [24], and coaxial impact-collision ion scattering spectroscopy [25]. The differences in polar face behavior of ZnO as measured with the above techniques was predicted by the early surface bonding model presented by Gatos [26], a model inspired by the differences in etching of the polar faces of InSb and GaAs both possessing zinc-blende structure. The polarity results have been correlated to the different etching behavior, topography, abrasion resistance, photoluminescence response, activation energy, and electrical conductivity of the two faces (Table 2.5).

During the etching of ZnO it has been observed that the O face etches more rapidly in oxidizing etchants than the Zn face [22]. The same has been observed for HCl and HNO_3 etchants, where it was found that the O face etches one order of magnitude faster than the Zn face [27]. This is in agreement with an earlier study on the wurtzite structure [28]. Different behavior during the etching process has also been detected in GaN another wurtzite, polar material [29] very similar to ZnO. The topography of the two faces as measured by atomic force microscopy (AFM) has been analyzed at different conditions, i.e., uncleaned as-received polished, after a solvent cleaning step, and after progressive O_2-atmosphere annealing ranging from 500 to 900°C [30]. These images showed clearly a difference between the Zn and the O face. In particular the Zn

Physical Properties	Symbols	Value	Units	Reference
Molecular Weight		81.38		[12]
Density		5.665	g/cm^3	[12]
Symmetry		hexagonal, wurtzite		[13]
Lattice Parameters	a_0	3.24265 ± 0.0001	Å	[12]
	c_0	5.1948 ± 0.0003	Å	[12]
	Zn-O	1.98	Å	[12]
	Zn-Zn	3.25	Å	[12]
(Experimental)	c/a	1.602		[14]
(Experimental)	volume	23.796	Å^3/f.u.	[14]
(Calculated)	c/a	1.59		[2]
(Calculated)	volume	23.62	Å^3/f.u.	[2]
Hardness	H	2	GPa	[15]
Energy Gap at 1.2 K	E_g	3.3435	eV	[16]
Energy Gap at room temperature	E_g	3.3	eV	[1]
Exciton Binding Energy		60	meV	[5]
Optical Gain		300	cm^{-1}	[5]
Lasing Threshold at room temperature		40-240	kW/cm^2	[9]
Dark Conductivity (undeformed)		10^{-5}	$\Omega^{-1}m^{-1}$	[17]
Melting Point		1975±25	°C	[12]
Dark conductivity (after 5% strain)		10^{-7}	$\Omega^{-1}m^{-1}$	[17]
Photo-conductivity (after 5% strain)		10^{-5}	$\Omega^{-1}m^{-1}$	[17]
Mobile dislocation type		β		[17]
Mean charge in the dark (qb/e)		-0.54		[17]

Table 2.1: ZnO Characteristics

Physical Properties	Symbols	Units	Voigt*	Reuss**	Reference
Elastic Modulus	E	GPa	124.2	123.0	[18]
Shear Modulus	G	GPa	45.8	45.3	[18]
Poisson's Ratio	ν		0.356	0.357	[18]

Table 2.2: ZnO Elastic Properties. (*) averaged according to Voigt's method. (**) averaged according to Reusst's method.

Compliance moduli	Bateman [19]	Simmons [18]	Kobiakov [20]
s_{11}	0.7858	0.7855	0.791
s_{12}	-0.3432	-0.3431	-0.33
s_{13}	-0.2206	-0.2205	-0.235
s_{33}	0.6940	0.6939	0.72
s_{44}	0.2357	2.3546	2.23

Table 2.3: Compliance Moduli in 1/Mbar=1/100GPa

Elastic moduli	Bateman [19]	Simmons [18]	Kobiakov [20]
c_{11}	2.097	2.0970	2.07
c_{12}	1.211	1.2110	1.177
c_{13}	1.051	1.0510	1.061
c_{33}	2.109	2.1090	2.095
c_{44}	0.4247	0.4247	0.448
Bulk Modulus	1.436	1.436	1.426

Table 2.4: Elastic Moduli in Mbar=100GPa

face was found to be much smoother than the O face for all conditions except for the surfaces annealed process at 500 °C for which bumps on the Zn face were observed. During the annealing process, except for the samples annealed at 500 °C, the Zn face decreased its roughness whereas the roughness of the O face remained about constant and always rougher than the Zn surface. Another physical property, the abrasion resistance, was found to be different on the two faces, where it was observed that the O face abraded more rapidly then the Zn face [22]. Photoluminescence (PL) measurements revealed noticeable differences in the two faces [31]. In a study conducted by Lucca et al. [32] PL of the two polar faces for etched surfaces and for surfaces polished under different conditions was reported. In this study it was found that for the etched, the mechanical and chemomechanical polished surfaces the O face had a relative PL intensity higher than the Zn face. The PL intensity was seen to decrease from the chemomechanical polished and etched surfaces, which were comparable, to the 1/4 μm and finally the 1 μm mechanical polished surfaces. The two polar faces have also been shown to have a difference in their activation energies [33], where the Zn face had an higher activation energy (85 kcal/mole) than the O

Physical Properties	Units	Zn Face	O Face	References
Etching Rate		lower	higher	Mariano [22]
Etching Rate (HCl)	μm/min	0.75	30	Matsuoka [27]
Etching Rate (HNO_3)	μm/min	.1	9.1	Matsuoka [27]
Roughness		lower	higher	Suscavage [30]
Abrasion Resistance		higher	lower	Mariano [22]
Relative PL Intensity		lower	higher	Lucca [32]
Activation Energy	kcal/mole	85	71	Kohl [33]
Electrical Conductivity*	A/V	10^{-4}	4×10^{-12}	Heiland [34]

Table 2.5: Differences between the Zn and O faces of ZnO. * values after transient heating in vacuum.

face (71 kcal/mole). Finally, Heiland [34] studied the electrical conductivity of the two polar faces of ZnO prepared by cleavage in ultrahigh vacuum (UHV) between 90 - 600 K. Both clean surfaces exhibited an upper limit of 4×10^{-12} A/V, but during transient heating in vacuum the Zn face showed a much higher surface conductivity of 10^{-4} A/V whereas the O face did not change from its value for a clean surface. In this study the surfaces were subjected to absorption of atomic hydrogen and oxygen. From these experiments it was noted that the atomic hydrogen acts much faster on the O face than on the Zn face, and that the depletion layer caused by the adsorption of oxygen is more evident on the Zn face.

2.1.3 Dislocations in the Wurtzite Lattice

Perfect [35] and partial [36] dislocations in the wurtzite lattice have been studied by Osip'yan in the late 1960s. The five most likely activated slip systems for a wurtzite structure have been determined by etching bent crystals of CdS [37]. These five slip systems are observed at ambient temperature to be the $(0001)[11\bar{2}0]$, $(0001)[10\bar{1}0]$, $(10\bar{1}0)[1\bar{2}10]$, $(1\bar{2}10)[10\bar{1}0]$ and $(10\bar{1}0)[0001]$. Other slip systems were also activated at higher temperature (700-740°C).

2.1.4 Photoplastic Effect in ZnO and Other Materials

Using the compression test Petrenko and Whitworth [17] and Carlsson [38] studied the flow of charge, which the found to be related to basal plane dislocations in ZnO. Both in darkness and under illumination, light was seen to change the carrier concentration, as was reported by Gorid'ko et al. [39]. In the study of Petrenko et al. [17] an increase in dislocation charge and flow stress (shear stress) along the basal plane with illumination was observed. In the study conducted by Carlsson [38] the first slip system activated (with glide dislocations) was identified as a basal plane: $\{0001\}<2\bar{1}\bar{1}0>$, and the second slip system activated at 75°C was identified as a prismatic plane: $\{1\bar{1}00\}<2\bar{1}\bar{1}0>$. The illumination had an effect on the basal plane dislocations but not those on the prismatic plane. In fact it was observed that light was able to stop dislocations on the basal plane, increasing the shear stress needed to move them, but not so on the prismatic plane. In the same work Carlsson investigated the influence of temperature on the shear stress in which he reported that the critical shear stress along the basal plane did not change with temperature but the critical shear stress along the prismatic plane decreases with the increase of temperature. This explained why by increasing temperature it was possible to have slip on the prismatic plane before the basal plane. To understand the influence of light an explanation of why the flow of charge is linked to basal dislocations is needed. The dislocations which lie in a plane can be seen as a succession of broken bonds, and as Shockley [40] reported, these dangling bonds can trap electrons, such that a n-type semiconductor can trap electrons and gain a negative charge. In a compound semiconductor such as ZnO, this trapping of electrons can occur for the basal plane since a the dislocation has its extra half plane ending with like atoms. However for the prismatic plane this is not the case [35] in that a dislocation has its extra half plane ending with alternating kinds of atoms which results in the broken bonds being eliminated through an interlock [38]. This can explain the absence of an influence of light on prismatic plane slip.

The photoplastic effect in the plastic deformation of CdS during compression has also been detected [41]. In addition, the effect of X radiation on the plastic deformation of II-VI compounds including CdTe, CdS, ZnS and ZnSe has also been investigated [42]. In addition to compression testing, the hardness test has also been used to study the photoplastic effect in Ge [39][43].

2.2 Nanoindentation

This work is focused on the investigation of the "surface" mechanical properties which may be significantly different from the bulk mechanical properties. To characterize the near surface mechanical properties significant efforts, in the development of new methods have been made in the last fifteen years. Whereas at first the microindentation method was used improvements have lead to the development of nanoindentation for the characterization of the near surface.

Conventional microindentation has long been employed to measure surface mechanical properties, however there are significant limitations with this technique when attempting to characterize thin films or surface regions less than several micrometers. Driven by an increasing need to characterize surface regions in the nanometer range [44], e.g., ultraprecision components, thin films on the order of 100 nm thick or less, etc., significant efforts in the development of indentation instruments that measure load versus depth have been made. Nanoindentation instruments not only provide information on surface hardness, but also offer the ability to obtain information on the elastic and time-dependent material properties of the surface. Their sensitivity is very high and allows for total penetration depths as small as 5 nm at loads of no more than 50 μN. Nanoindentation has also recently been used to determine the resolved shear stress under the indenter. the near surface residual stress state, the viscoelastic-plastic properties of glasses and polymers. and the fracture toughness of thin coatings, although fundamental understanding of these measurements is still

being developed.

2.2.1 History

The measurement of hardness can be divided into three main categories: 1) scratch hardness; 2) rebound or dynamic hardness; and 3) static indentation hardness [45].

Scratch hardness is the oldest form of hardness measurement. It depends on the ability of one material to scratch another. Friedrich Mohs first put the method on a semi-quantative basis in 1822 by establishing a scale of 10 minerals as standards, from talc as the softest to diamond as the hardest [46].

Rebound or dynamic hardness involves the dynamic deformation or indentation of the surface. For this measurement, a diamond-tipped hammer (known as a "tup") is dropped from a fixed height onto the test surface and the hardness is expressed in terms of the energy of impact and the size of the remaining indentation.

(Quasi)static indentation methods are the most widely used in determining the hardness of materials. Indentation hardness is essentially a measure of the plastic deformation properties and, to a secondary extent, the elastic properties of a material. This method is performed by pressing an indenter into the material and evaluating the hardness as the ratio of the load applied to the indenter to the area of the imprint left by the indenter. The material and shape of the indenter as well as the area considered in evaluating the hardness has undergone a progressive evolution by the use of various indentation techniques. The most important indentation techniques in chronological order (from the oldest to the most recent) are: Brinell, Meyer, Vickers, Rockwell, Knoop (microindentation) and Berkovich (nanoindentation).

In the early twentieth century, Brinell introduced indentation with a steel ball. From this test a single number, the hardness, was obtained as the ratio of the load applied to the indenter to the surface area of the residual impression measured by optical devices. After the first indentation technique was introduced by Brinell, a variety of improvements were introduced to arrive to the Berkovich hardness testing

technique. The material of the indenter went from steel to diamond, which due to its greater stiffness was able to characterize a much broader range of materials. The shape of the indenter went from spherical to a three-sided pyramid which is easier to obtain (note that a spherical shape in diamond is very difficult to obtain) and due to its well-defined geometry, able to leave a well-defined imprint. The area used to obtain the hardness evolved as well going from the surface area measured by optical devices, to the projected area of the residual impression obtained by the load-displacement curve.

2.2.2 Analysis of Indentation Data

Evaluation of Hardness and Elastic Modulus from the Indentation Test

In the last two decades significant efforts have been made to develop a method of testing the surface mechanical properties of materials on the submicron scale. As a result, this has been made possible by the development of instruments that continuously measure force and displacement [45][47][48]. The mechanical properties can be obtained from the loading [49] or unloading [48][50][51] portion of the force-displacement curve irrespective of the small size of the indentation imprint. In the present work, the Oliver and Pharr model [50] was used for the reduction of the force-displacement data. The steps employed are described below.

The elastic modulus (E) is the most commonly measured mechanical property along with the hardness (H). To do so, the unloading data are analyzed according to a model relating the contact area at the peak load to the elastic modulus by considering the deformation of an elastic half space by an elastic punch. Then the needed contact area is estimated from the indenter shape function. Once the contact area is known, it is possible to obtain a separate measurement for E and H.

The elastic contact problem, of fundamental importance in the analysis procedure, was originally considered in the late 19th century by Boussinesq [52] and Hertz [53]. Boussinesq developed a method based on potential theory for computing the stresses

and displacements in an elastic body loaded by a rigid, axisymmetric indenter. His method was used to derive the solutions of several indenter geometries such as cylindrical and conical indenters [54]. Hertz analyzed the problem of the elastic contact between two spherical surfaces with different radii and elastic constants. The work of Hertz was used as a model to remove the assumption of a rigid indenter. Another major contribution was made by Sneddon, who derived general relationships between the load, displacement, and contact area for any punch that can be described as a solid of revolution of a smooth function [55]. His results show that the load-displacement relationship for a simple punch geometry can be written as:

$$P = \alpha h^m \tag{2.1}$$

where P is the load applied to the indenter, h is the elastic displacement of the indenter, and α and m are constants where m depends on the geometry of the indenter.

To consider the plastic effect on the above elastic problem involves dealing with nonlinear constitutive equations and a number of material parameters describing the material behavior. An early experiment of Tabor [56][57] concerning the shape of the indentation imprint after the elastic recovery of the material sheds considerable light on the effects of plasticity in indentation. Tabor's experiments showed that, at least in metals, the imprint left by a spherical indenter is still spherical with a slightly larger radius than the indenter, and the imprint left by a conical indenter is still conical with a larger included tip angle. The significance of these experiments is that since the elastic contact solution exists for several geometries, the ways in which plasticity affects the indentation of elastic unloading data can be dealt with by taking into consideration the shape of the perturbed surface in the elastic analysis. Tabor used this result to relate the elastic modulus to the size of the impression left after indentation. This intuition was further resolved in the early 1970's, by the work of

Bulychev, Alekhin. and Shorshorov into the following equation

$$S = \frac{dP}{dh} = \frac{2}{\sqrt{\pi}} E_r \sqrt{A} \tag{2.2}$$

where $S = dP/dh$ is the experimentally measured stiffness obtained from the unloading data, E_r (or E^*) is the reduced modulus, and A is the projected area of the elastic contact. The reduced modulus is another result of Tabor's experiments, and was defined to account for the non-rigidity of the indenter. It is defined as

$$\frac{1}{E_r} = \frac{(1-\nu^2)}{E} + \frac{(1-\nu_i^2)}{E_i} \tag{2.3}$$

where E and ν are the elastic modulus and Poisson's ratio for the specimen and E_i and ν_i are the same parameters for the indenter. The early equation Eqn. (2.2) which relates the elastic modulus to the measured stiffness and to the projected area was developed for a cone indenter. It has been shown, however, to apply to not only indenters generated by a solid of revolution but for pyramidal indenters as well [58].

To obtain E_r from Eqn. (2.2), A must also be determined. The projected area can be measured optically, but for small dimensions this is a time consuming and difficult task. To avoid measurement of the imprint, Oliver et al. [59] suggested a simple method to evaluate the projected area based on the load-displacement data and a knowledge of the indenter area function (or shape function), i.e., the cross-sectional area of the indenter as a function of the distance from its tip. This method is based on the assumption that at the peak load the material deforms conformally to the shape of the indenter, as can be seen in Fig. 2-2 where the behavior of the indenter-surface during indentation is shown. From Fig. 2-2 three depths can be distinguished: $h_{\max}$ the maximum depth which the indenter reaches at maximum load evaluated from the undeformed surface; h_f the final depth left once the load is completely released; and h_c the contact depth evaluated at the peak load and the maximum depth but considering the deformation undergone by the surface (curvature

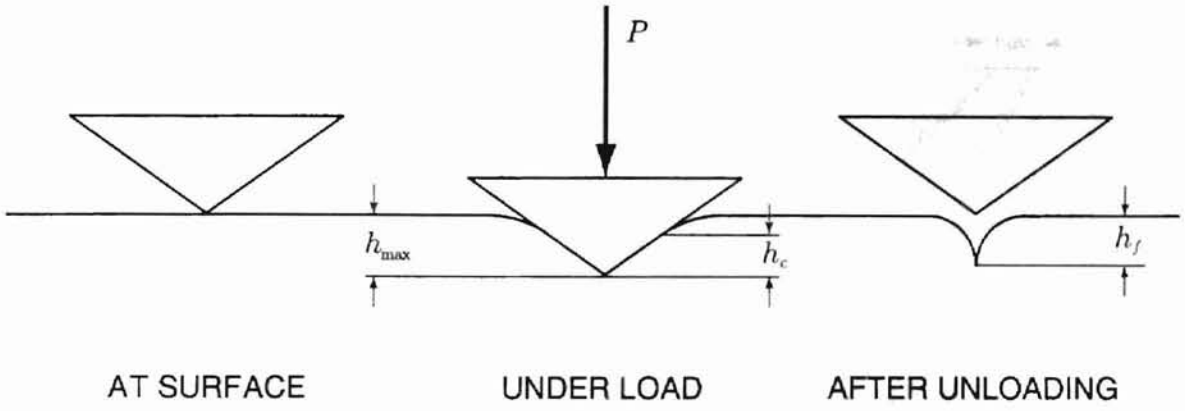

Figure 2-2: Schematic representation of the indenting process showing h_c, $h_{\max}$, and h_f

of the surface resulting from the elastic response). The maximum and final depths can be easily determined from a typical load-displacement curve obtained by indentation as shown in Fig. 2-3, and then the maximum depth can be used to determine the projected area [59]. An improvement of this method was made by considering the contact depth to evaluate the projected area (from now on referred to as the contact area) which is inbetween the maximum and final depth (Fig. 2-3). An empirical method was proposed to evaluate the contact depth by Doerner and Nix [48] based on extrapolating the initial linear portion of the unloading curve to zero load. This empirical method was successively modified [50] by considering the initial stage of unloading to be not linear, but to follow a power law of Sneddon type, Eqn. (2.1). This results in a translation of the contact depth towards the maximum depth and the magnitude is a function of ε, the geometry of the indenter (for example $\varepsilon = 1$ for a flat punch and 0.72 for a conical indenter). Once the contact depth is known the contact area could be determined by the indenter area function. Then, the elastic modulus and the hardness can be evaluated separately, the elastic modulus with Eqn.

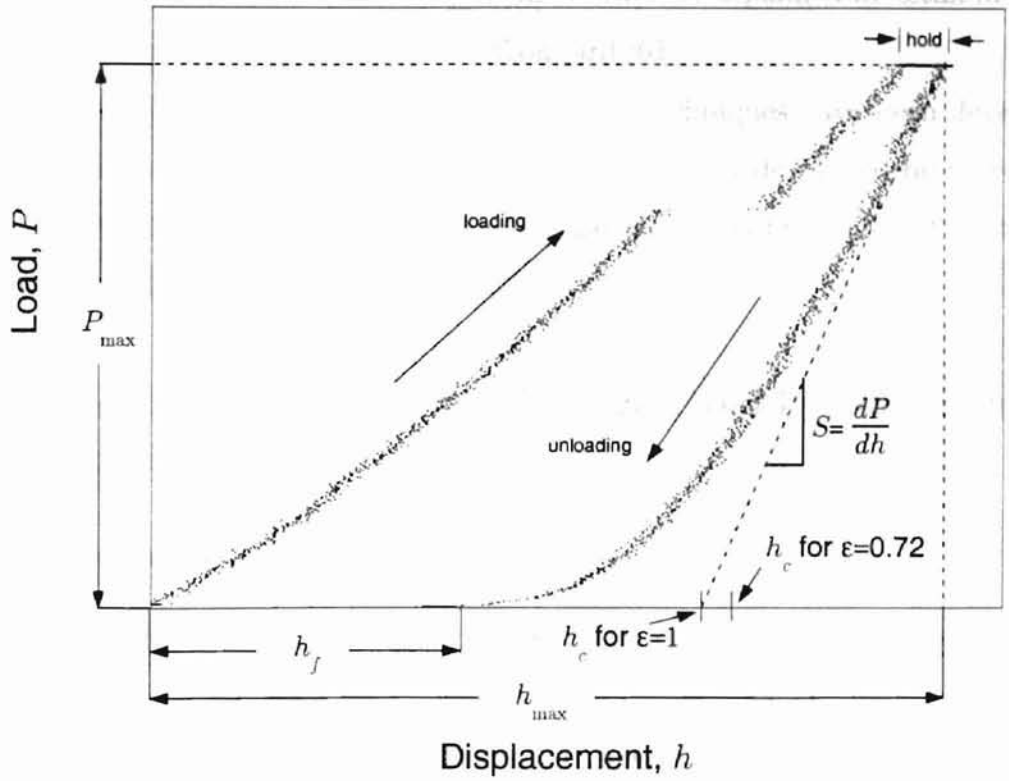

Figure 2-3: Typical load-displacement curve showing: $P_{\max}$ the maximum load; $h_{\max}$ the maximum depth; h_f the final depth; h_c the contact depth which is a function of the indenter geometric constant ε: and S the measured stiffness.

(2.2), and the hardness from the definition:

$$H = \frac{P_{\max}}{A} \tag{2.4}$$

The uncertainties resulting from the use of the method described above have been reported [60].

2.2.3 Instrument

Different types of nanoindentation instruments have been described in detail by Bhushan [45]. In particular, an instrument capable of measuring depth and load

simultaneously, similar to the one used in this work, and explained in detail in Chapter 3 was described by Doerner [48] and Woirgard [61].

To calibrate the indentation instrument several techniques have been developed. The most widely used is the one described in Appendix A developed by Oliver and Pharr [50]. Among the other techniques are those developed by Loubet [47], Doerner [48], and Sun [62].

2.2.4 Mechanical Properties Characterized by Nanoindentation

Elastic Modulus and Hardness

As previous discussed for the measurement of elastic modulus and hardness, continuous load versus indenter displacement-measuring instruments, combined with methods to determine the contact area between the indenter and the sample surface are employed.

The differences in values for elastic modulus and hardness obtained using the projected contact areas calculated from the Oliver and Pharr method [50] and those from direct measurement of the contact area with an atomic force microscope, have been reported [63][64][65].

There have been a variety of studies reported on the measurement of the elastic modulus and hardness of single crystal materials. For example, Au [66][67], SiC [68], Fe-3%Si [69][70][71], ZnS sphalerite [72], GaP [73] and GaN [15][74] single crystal surfaces have been studied. In addition the characterization of GaN has been reported for both bulk material [75], and thin films [76][77]. GaN is a compound semiconductor very similar to ZnO considered in this work, having the same wurtzite structure and similar "optoelectronic" characteristics. Whereas it should be note that ZnO has never been studied by nanoindentation, results of conventional hardness (Vickers) for bulk ZnO have been reported to be 2 GPa [15][78].

Nanoindentation has been successfully used to characterize the mechanical properties of the material surface as a function of surface roughness, of different polishing methods used to finish the surfaces, of different polar faces, and of material anisotropy. The influence of surface roughness on the measurement of hardness has been reported by Bobji [79], where the contact area was evaluated by AFM.

Recently the difference in surface mechanical properties resulting from electrolytically and mechanically polished (001) tungsten have been characterized using nanoindentation [80]. From this study it was found that for the mechanically polished surface plastic deformation occurred from the onset of loading, contrary to the electrolytically polished surface in which the deformation was found to be purely elastic until the force reached a critical value. Beyond this critical force, a sudden increase in depth was observed. A similar finding has been reported for Fe-3wt%Si [70].

Indentation has also been used to measure the differences in hardness of the two polar faces of several materials over a broad range of temperatures [73][81][82][83]. In a study of indium antimonide (InSb), where a Vickers indenter was used on the {111} faces, it was found that the In face was harder than the Sb face at all temperatures. However, the hardness difference was small at high temperatures, and within the experimental error at low temperature. The differences in hardness varied between 7% and 17% in the temperature range studied (20-400°C). It is believed that this behavior is related to the different mobilities of the In(g) and Sb(g) dislocations [81]. Here, the "g" represents glide dislocations so as to distinguish them from "s" shuffle dislocations. In Fig. 2-4 shuffle and glide dislocations for ZnO are shown. In a study of GaP a difference in microhardness between the P $\{\overline{111}\}$ surface and the Ga {111} surface was observed where the Ga surface was found to be harder [73]. As in InSb, this difference was attributed to different dislocation mobility. Moreover it has been stated that the observed difference in chemical polishing behavior of two faces of a polar material may be a result of the observed surface microhardness differences [73]. The nature of the differences in hardness of the two polar faces of GaAs has

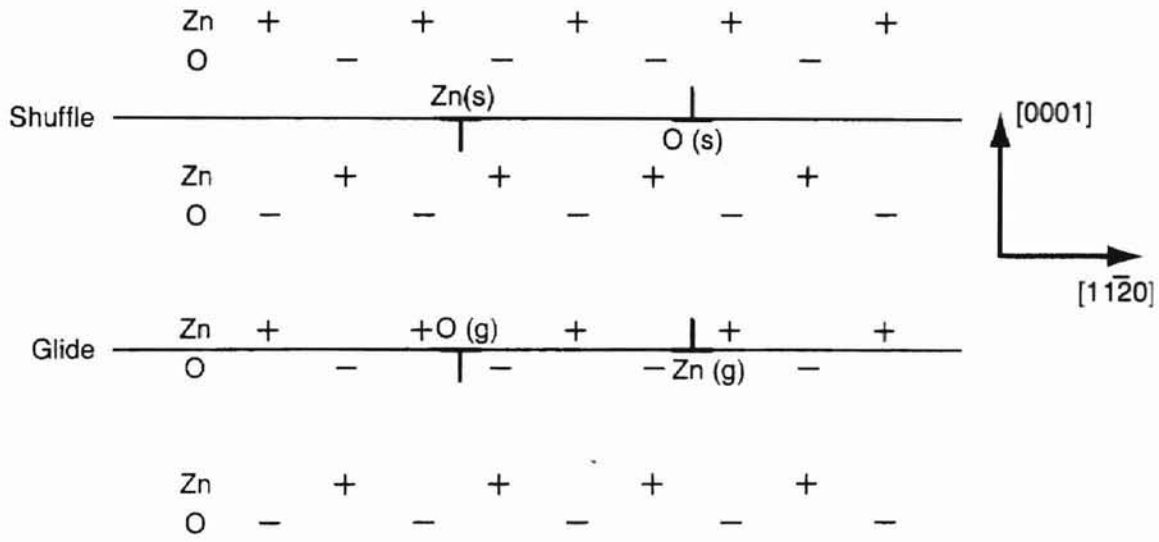

Figure 2-4: Simplified diagram of ZnO structure showing the "glide" and "shuffle" planes, and the possible types of dislocations.

been explained in detail in terms of slip geometry, sense and type of slip expected, dislocation interactions and the known differences in velocities of As(g) and Ga(g) dislocations [82]. Hardness polarity has been shown in 4H-SiC single crystals as well [83]. Significant differences between the silicon-terminated (0001) and carbon-terminated $(000\bar{1})$ faces of this polar crystal were found. Experimentally it is known that dislocations in semiconductors are dissociated [84][85] and that the velocity of the two partials in compound semiconductors can be very different [86]. Presumably this has to do with the different core structure of the two partials. In a work of Ning et al. [83] it has been stated that in a compound semiconductor, XY - where X is a group II, group III, or group IV atom, and Y is a group VI, group V, or group IV atom - the X and Y atoms occupy the lattice sites of two different, interpenetrating fcc or hcp (with an ideal c/a ratio) sublattices which are translated by a vector $(a/4,a/4,a/4)$ or $(a/3,2a/3,c/8)$ with respect to each other. In this way, these materials have a zincblende or a wurtzite structure, respectively. As a result, all the atoms at the core of one of the partials are X, while the core of the other partial consists of all

Y atoms. Consequently, it is expected that the leading partial is always the faster partial and the trailing partial is the slower one. Following this model ZnO, a II-VI compound with a wurtzite structure, will result in the generation of Zn(g) leading partial dislocations. The effect of anisotropy on indentation has also been presented in a study on Au by Kiely et al. [87], and on KCl, NaCl, LiF and MgO [88][89].

Nanoindentation has also been successfully used to characterize the elastic modulus and hardness of monolayer films as a function of film thickness, growth condition, chemical composition and residual stress state, and of multilayer films as a function of the modulated period. The mechanical properties of sol-gel zirconia deposited on polished disks of 316 stainless steel were measured as a function of film thickness from 0 nm (as polished) to 900 nm, for different values of load [90]. Similar work has been done on sol-gel-deposited titania (TiO_2) on glass and copper with thicknesses from 50 nm to over 200 nm [91], on aluminum deposited on glass with thicknesses between 240-1700 nm [65], and on sol-gel-derived hard coatings on polyester [92]. In this last study, the influence of UV irradiation and low temperature heating on the thickness and the hardness of the film was reported. The hardness of the films was evaluated not only as a function of film thickness but also as a function of the deposition temperature of the film, since deposition temperature was shown to be related to the thickness of the TiN and TiCN coatings [93]. A correlation between the resulting hardness of silicon oxinitride (SiO_xN_y) films and processing temperature has also been reported [94]. The effects on measured elastic modulus and hardness of the substrate bias voltage and nitrogen partial pressure in the deposition of titanium nitride (TiN_x) thin films [95], and vacuum annealing time in the deposition of Mo-Si-N/SiC [96] have also been studied. The influence of the carbon-to-nitrogen composition ratio, x, in TiC_xN_{1-x} thin films deposited on cemented carbide substrates on the mechanical properties including hardness and elastic modulus has also been reported [97]. In this study, TiC_xN_{1-x} thin films were grown with x=0 (TiN) to x=1 (TiC) by varying the flow ratio between the reaction gases CH_4 and N_2. In another

study by the same research group, the mechanical properties of TiC_xN_{1-x} thin films deposited on cemented carbide substrates were measured as a function of the intrinsic stress of the film as measured by X-ray diffraction [98]. Investigation into the effects of multilayer structures of compositionally modulated Ti/TiN films on their hardness where the modulation periods examined were 10, 15, 20, and 40 nm has also been reported [99].

Film Thickness

In the measurement of the mechanical properties of thin films the relation between the ratio of the maximum indentation depth to the film thickness has been analyzed [65]. Studies on the evaluation of the critical ratio, which is that of the maximum indentation depth to the film thickness in film/substrate systems such that the indentation hardness is representative of the mechanical properties of the film alone have been reported. Several years ago Bückle suggested the one-tenth rule (critical ratio = 0.1) [100]. However this empirical suggestion may not be applicable when film thicknesses are very small since the elastic displacement varies as 1/r, where r is the distance from the initial contact between the indenter and the specimen, and the influence of the substrate on the composite compliance would be apparent even at very small indentation depths. To address this problem, analytical solutions to determine the critical ratio have been proposed by Kim [101] and more recently by Yoffe [102]. In the work of Cai and Bangert [103] the finite-element method was used to simulate microhardness testing procedures of coating-substrate composites (with hard and soft substrates) and to determine the critical ratio of penetration depth to film thickness. These are based on the extension of the plastic deformation zone under the indenter, on the load at each incremental step and on the mean pressure curve, in order to obtain the actual value of microhardness of the coating so as to avoid the influence of the substrate. Experimental studies of the effect of the substrate on the measured mechanical properties of thin film systems have also been reported. In the

work of Li et al. [104] the variation of measured hardness of the bulk material of the film to that of the bulk material of the substrate as a function of the depth of indentation in different thin-film coating/substrate systems was studied. These included DLC coatings on silicon (hard substrate) and DLC coatings on polycarbonate (soft substrate). This study enabled identification of the indentation depth at which the measured hardness was that of the bulk material of the film, and hence identification of the critical ratio. Olofinjana et al. [91] proposed another method for determining the critical ratio when the bulk hardness of the film material is not known. In this method, sol-gel-deposited titania films were deposited on two different substrates, one hard (glass) and one soft (copper). The hardness of the two film/substrate systems was then measured as a function of the indentation depth which enabled identification of the critical ratio.

Thin Film Adhesion

Nanoindentation and nanoscratching have recently been employed to quantitatively assess film adhesion in thin film/substrate systems. The true work of adhesion is the thermodynamic work required to create two new surfaces at the expense of the interface, and is merely a summation of surface energies. However in most practical cases of de-adhesion, there is additional inelastic damage, such as plasticity and microcracking which occurs in regions of the substrate and film near the interface that is directly associated with the interfacial delamination. In either case, the property of interest is the energy associated with the interfacial fracture. Analytical models have been developed utilizing linear elastic fracture mechanics concepts, in which delaminations are modeled as bi-material cracks and film adhesion is characterized by the strain energy released per unit increase in delamination area [105][106][107]. These concepts have been successfully applied to many practical test methods. Some of the simplest to conduct are those utilizing a nanomechanical probe such as indentation, scratch, and line scratch techniques (a comparison of these three techniques has been

reported [108]), in which a sub-micron diamond indenter is used to initiate and propagate interfacial cracks. Analysis of the load-displacement curves and fractographic measurement by optical microscopy yield the parameters for use in the theoretical models. A key feature of these techniques is that each involves a different ratio of shear to normal stresses, or mode mixity, at the adhered film/substrate boundary. The adhesion value corresponds to the toughness of the interface at some particular mixity value.

The test methods mentioned above have some limitations, and in fact they are often impractical for ductile or strongly adhering films because of the difficulty of initiating delamination. The mechanics for calculating the quantitative driving force of indentation-induced delamination of thin-film multilayers has been reported [109]. Ductile and strongly adhering films tend to simply deform plastically before the development of sufficient elastic strain energy for delamination. To address this limitation, researchers have used superlayers deposited over the film of interest [109]. The superlayer, typically a refractory compound that does not significantly alter the underlying film, is vapor deposited at a low temperature which results in a high residual stress that provides the additional driving force for delamination. The effects of compressive residual stresses on the fracture of thin sputtered-deposited tantalum nitride films have been studied by indentation fracture and continuous nanoscratch testing [110]. In another study, nanoscratch testing has been combined with a multilayer sapphire and aluminum nitride single-substrate system to determine the effects of interface composition and structure, measured by high resolution transmission electron microscopy, on the susceptibility to fracture of hard, thin tantalum nitride films [111]. The same was also measured by nanoindentation [112]. A comparison between three different adhesion tests, viz., flexure, micro-indentation, and scratch has also been reported [113].

Residual Stress State

The influence of applied stress on the measurement of hardness and elastic modulus using nanoindentation has been investigated by Tsui et al. [114] and Jarausch et al. [115]. These studies paved the way for new techniques for estimating near surface residual stress using nanoindentation. In a recent study, the increase of residual stress resultant from UV laser-induced cracks in fused silica has been measured using nanoindentation [116]. This relative residual stress measurement (relative to the existing residual stress of the bulk) was made with the aid of a simple theoretical model based on the change of penetration depth and the change in elastic modulus and hardness. In a study of the indentation of intergranular phases of silicate glasses in polycrystalline alumina, the change in the load-displacement curve from the strained silicate-glass films, which had a known value of residual stress, was used to make an estimate for the absolute residual stress [117]. In another study the residual stress in a thin stressed layer at a glass surface was determined by a method based on the measurement of the half-penny radial crack lengths produced at the corners of Vickers indentations [118]. This method enables the evaluation of residual stress by the determination of the fracture toughness and geometric evaluation of the crack obtained after indentation with the Vickers tip. Fracture toughness has been measured as a function of the peak load applied during indentation and to the radial crack length [119]. Recently a new method for estimating residual stresses by instrumented sharp indentation, assuming the residual stresses and the residual plastic strains to be equi-bi-axial and uniform over a depth which is at least several times larger than the indentation contact diameter, has been proposed [120].

Viscoelastic-plastic Properties

Recently nanoindentation has been employed to evaluate viscoelastic-plastic properties of glasses and polymers. It is known that a viscoelastic material exhibits complex time-dependent behavior. One method to deal with analytical viscoelastic problems

is to remove the time variable in the governing equations and in the boundary conditions by employing the Laplace transformation with respect to time. The viscoelastic problem becomes, in effect, an elastic problem. The desired viscoelastic solution can then be obtained by performing the inverse Laplace transform on the elastic solution. However, the Laplace transform method can only be used when the interface between stress and deformation boundaries does not change with time. Another approach in solving viscoelastic problems is to use the method of functional equations put forth by Radok [121]. The functional equations can be obtained by replacing the elastic constants in the elastic solution by equivalent viscoelastic operators appearing in the viscoelastic constitutive equations. This method admits the existence of a moving boundary, e.g., a contact surface. This latter approach has been adopted in combination with nanoindentation testing for the characterization of viscoelastic properties. Using this method, Cheng [122] has developed an analytical method for flat and spherical tip indentation which can be applied to compressible as well as incompressible coatings. For viscoelastic analysis, nanoindentation has been used in relaxation and creep tests. In a relaxation test, the indenter is rapidly driven against a half space of viscoelastic material to a certain depth and is then held at that depth for a sufficiently long time. In a creep test, the indenter is abruptly loaded to a certain value that is maintained thereafter. The use of this method and its improvement by taking the hydrostatic pressure dependence of the elastic modulus and substrate effects into consideration has been studied [123]. The approach described above relies on a one-dimensional model. Further study on a more realistic three-dimensional model of the response of viscoelastic materials to indentation by spherical indenters, which incorporates the stress and strain distributions beneath the indenter, has also been reported [124]. In a study of viscoelastic-plastic properties of PET, load-displacement data has been used to evaluate the elastic modulus, the hardness and the creep behavior [125]. The elastic modulus has been evaluated using two methods: 1) assuming the elastic behavior during initial unloading to be that of a cylindrical punch; 2) us-

ing a power-law relation. The hardness was calculated by depth-sensing and imaging methods and the creep behavior was evaluated by the variation of the hardness as a function of time. Furthermore, the influence of the maximum penetration depth and loading and holding times on the hardness values were also addressed.

Fracture Toughness

Fracture toughness of thin films has been calculated based on the analysis of the energy release rate from the load-displacement curve during nanoindentation. For indentation techniques, radial cracks are produced during the unloading cycle when brittle materials are indented by a sharp indenter. The length of radial cracks is known to correlate with the fracture toughness and is used to calculate fracture toughness based on various equations which have been reported [126][127]. The fracture process has been shown to progress in three stages [126]: 1) first ring-like through-thickness cracks from around the indenter result from high stresses in the contact area; 2) delamination and buckling occur around the contact area at the film/substrate interface by high lateral pressure; and 3) second ring-like through-thickness cracks and spalling are generated by high bending stresses at the edges of the buckled film. The same model has been used to study the fracture toughness of multilayer hard coatings deposited on cemented carbide [128]. In this study, the changes in slope of plots of load-penetration depth squared were shown to reveal the changes of the coating/substrate system. Two other methods based on correlating crack lengths emanating from the corners of the indentation when the indenter and load are removed, and correlating fracture toughness have been reported [129]. A new mechanical test, the cross-sectional nanoindentation test, has recently been developed for measuring fracture toughness [129]. In this test indentations are made normal to the wafer cross-section within the substrate and close to the interface of interest. From the results of this test a model based on elastic plate theory was developed to numerically calculate the interfacial critical energy release rate [130]. Inputs to the model are the

thin film elastic properties, thin film thickness, interfacial crack area and maximum thin film deflection during the test. The interfacial delamination area (crack area) was measured by optical and scanning electron microscopy. The maximum thin film deflection during the test can be obtained from the load versus displacement curves and the Berkovich diamond-tip geometry assuming that the indenter shaft does not tilt during the test. The anti-wearability of brittle materials has been shown to be principally determined by its fracture toughness, when cracks occur on the worn surface [128], where anti-wearability is determined by the fracture toughness, the elastic modulus and the hardness.

2.2.5 Pop-in

Pop-in is a sudden increase of penetration depth at constant load P_{crit}, and is shown on a load-displacement curve in Fig. 2-5. It has been attributed to a variety of mechanisms including sudden nucleation of dislocations, oxide layer breakthrough, the occurrence of a phase transformation. or twinning. Pop-in can occur due to any process which results in sudden release of strain energy [131]. Studies on a variety of materials have attributed pop-in to a sudden nucleation of dislocations. These are listed in Table 2.6 and include Au [67][132], Al [133], single crystal Fe-3%Si [69][70][71], GaAs [69][134][135], MgO [135][136][137], InP [134], Al_2O_3, single crystal SiC [68], (001)TiN [138], AlGaN thin films [139], GaN thin films deposited on sapphire [76][77] and bulk GaN [76].

The arguments that have been made for attributing the yield point of a material to the nucleation of dislocations are essentially two, i.e., 1) observation of elastic behavior before the onset of plasticity and 2) the agreement between the maximum shear stress under the indenter calculated by P_{crit} and the theoretical shear strength, which is the ideal shear stress if slip is assumed to occur by the translation of one plane of atoms over another in a perfect lattice. An additional argument made in several studies is the absence of cracks as observed by atomic force microscopy (AFM)

Material	P_{crit} (mN)	Range %	h_{crit} (nm)	Indenter	Reference
Au	$90 - 700\frac{Kg}{mm^2}$	±77.2	NR	1	[67]
Al[a]	$15 - 27 \times 10^{-2}$	±28.6	~ 7	2	[133]
Al (110)	$\sim 3 \times 10^{-1}$		~ 15	2	[133]
Al (111)	$\sim 8 \times 10^{-3}$		~ 6	2	[133]
Al (133)	$\sim 15 \times 10^{-2}$		~ 8	2	[133]
Fe-3%Si[b]	$7 - 30 \times 10^{-2}$	±62.2	~ 17.6	3	[69]
GaAs	$\sim 6 \times 10^{-2}$		~ 18	3	[69]
GaAs	$23 - 45$	±32.3	~ 200	4	[134]
InP	$10 - 17$	±25.9	~ 150	4	[134]
SiC[b]	6.2 ± 0.5	±8.1	~ 85	2	[68]
Al_2O_3[c]	1.5 ± 0.4	±26.7	~ 100	2	[68]
Al_2O_3[d]	7.3 ± 1.8	±24.6	~ 40	2	[68]
TiN (001)	0.34 ± 0.04	±11.8	~ 15	2	[138]
GaN[e]	21.0 ± 2	±9.5	~ 35	2	[77]
GaN[f]	$24 - 40$	±25.0	~ 150	4	[76]

Table 2.6: Reported pop-in values for several materials with the range of the value of critical load. (a) polycrystal material, (b) single crystal material, (c) indentation on (1012) plane, (d) indentation on (0001) plane, (e) thin film 1.3-2.4 μm thick, (f) thin film 3 μm thick. The indenters used and listed above are (1) Four-side pyramidal, (2) Berkovich, (3) Sharp three-sided, (4) Spherical with radius of 4.2 μm. NR=not reported

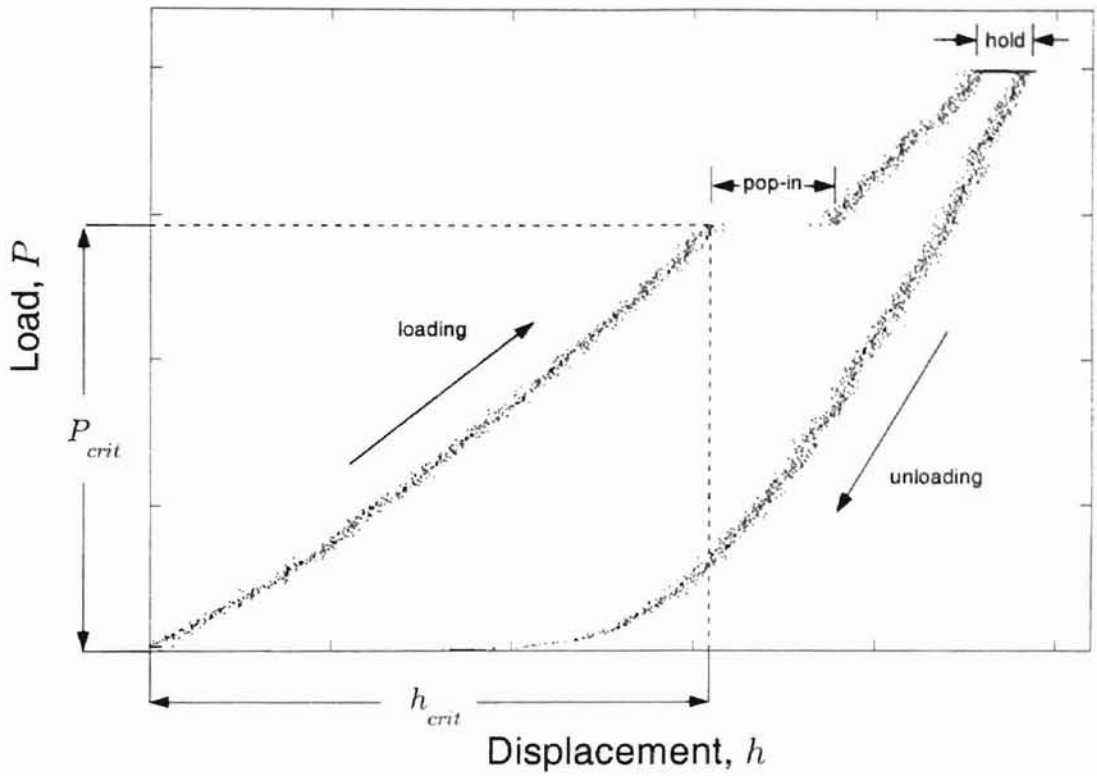

Figure 2-5: Pop-in

imaging [133][136]. Shown in Fig. 2-6 is a typical load-displacement curve obtained during loading and unloading before P_{crit} has been reached. The elastic behavior of the material at a load lower than P_{crit} is used to explain the fact that pop-in can be viewed as the onset of plasticity, or in other words the first movement of dislocations. A question arises as to whether the dislocations are created and then moved (where by the shear stress should be equal to the theoretical shear stress) or whether they were already present in the material and were then moved (where by the shear stress should be equal to the Peierls-Nabarro stress). To address this issue Gane [67], during indentation of Au, observed that the maximum shear stress under the indenter, which was considered to be approximately equal to 1/6 of the pressure under the indenter, was in agreement with the reported theoretical shear strength of Au. This suggested that the dislocations were generated and then moved.

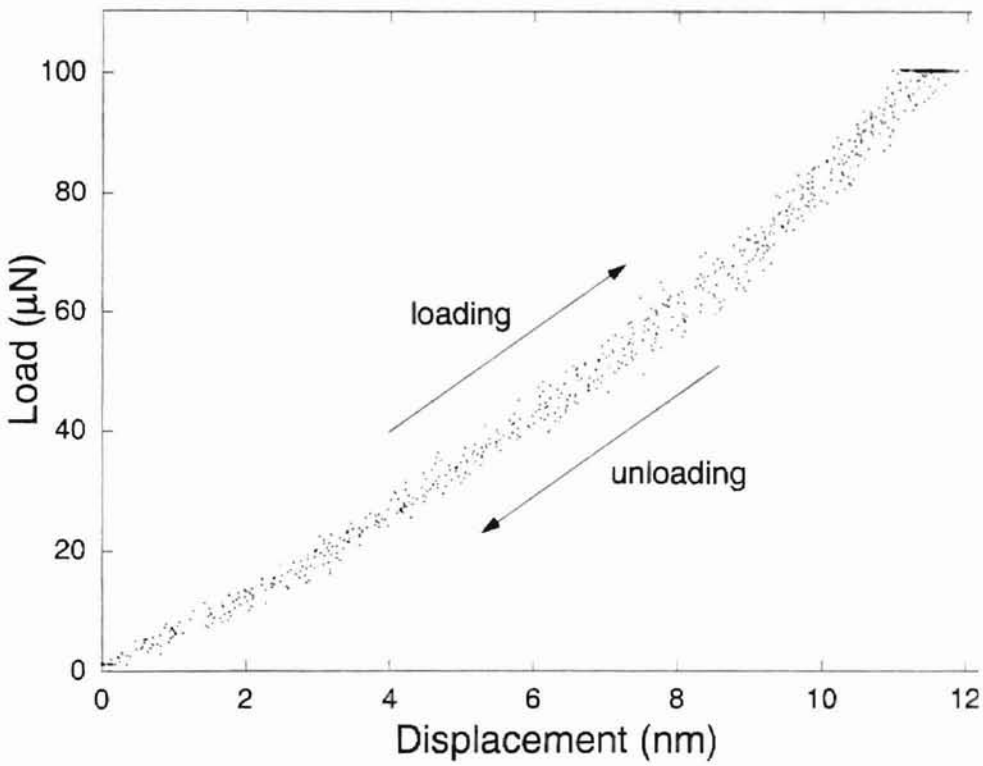

Figure 2-6: Typical elastic behavior observed before onset of plasticity o

To evaluate the pressure under the indenter and then the maximum she the Hertzian theory of elastic contact between two non-rigid spheres was us solution has been summarized by Johnson [53], where the maximum pressu the spherical indenter (p_0) is

$$p_0 = \left(\frac{6E_r}{\pi^3 R^2}\right)^{1/3} P^{1/3}$$

where E_r is the reduced elastic modulus, given in Eqn. (2.3), which account non-rigidness of the sphere, R is the radius of the spherical tip, P is the load to the indenter, in this case P_{crit}. Then the maximum shear stress under the

is given as

$$\tau_{\max} = 0.31 p_0 = 0.18 \left(\frac{P_{crit} E_r^2}{R^2} \right)^{1/3} \tag{2.6}$$

Equation (2.6) has been used in a variety of studies [69][70][71][132][133]. A particular solution of the Hertzian problem has been presented by Timoshenko [140] where he assumed that both bodies in contact had the same elastic properties and took Poisson's ratio as $\nu = 0.3$. Then, Eqn. (2.6) becomes

$$\tau_{\max} = 0.12 \left(\frac{P_{crit} E^2}{R^2} \right)^{1/3} \tag{2.7}$$

where E is the elastic modulus of the sample as well as the indenter. Although this solution is a very rough approximation, not considering the differences between the diamond tip and the different kind of samples, it has been used in several studies [68][77][138][139]. Once the maximum shear stress under the indenter has been calculated it can be compared to the theoretical value. The theoretical shear strength [141] can be approximated by

$$\tau_{theo} = \frac{G}{2\pi} \tag{2.8}$$

where G is the shear modulus of the sample. This equation has been extensively used [69][70][132][133]. The value τ_{theo} should not be confused with the shear stress needed to move an existing dislocation which is the Peierls-Nabarro stress τ_p [142] and is given by

$$\tau_p \approx \frac{2G}{1-\nu} e^{-[2\pi a/(1-\nu)b]} \tag{2.9}$$

where ν is Poisson's ratio, a is the distance between slip planes and b is the distance between atoms in a slip plane along the slip direction [46][143]. Other expressions for the critical shear stress τ_{crit} for the creation of a dislocation loop have also been presented. Page et al. [68] have used

$$\tau_{crit} \approx \frac{Gb}{4\pi r} \ln \left(\frac{R^*}{r_0} \right) \approx \frac{Gb}{4\pi r} \ln \left(\frac{r}{r_0} \right) \tag{2.10}$$

where r is the radius of the loop, r_0 the dislocation core radius, and R^* the upper limit of the stress field integration. Bahr et al. [71] report

$$\tau_{crit} = \frac{2-\nu}{1-\nu}\frac{Gb}{8\pi}\left[\frac{4}{4r-\frac{2}{r_0}} + \frac{1}{r}\ln\left(\frac{4r}{r_0}-2\right)\right] \tag{2.11}$$

where b is the Burgers vector, and Oden et al. [138] have employed the simplified expression

$$\tau_c = \frac{Gb}{2\pi r_c} \approx \frac{G}{10} \tag{2.12}$$

where r_c is the critical radius.

Much work has been conducted to determine whether the yield point behavior is associated with dislocation nucleation or oxide breakthrough [70]. For example, in the work conduced by Gerberich in 1996 [69], two different occurrences of pop-in have been observed. The first occurrence at a load between 70 and 300 μN was associated with the onset of dislocation nucleation and the second at a load of about 2 mN was associated with the breakthrough of the surface oxide layer. In an earlier study by the same research group [144] similar behavior was seen where it was argued that the second pop-in observed was not due to dislocation nucleation but rather oxide breakthrough. The authors pointed out that the measured force to initiate the yielding process was more than an order of magnitude greater for Fe-3wt%Si than for Ni although these two materials had similar elastic moduli and thicknesses of the oxide overlayers. If the pop-in was caused by nucleation dislocation a similar force to initiate yielding should have been observed. In a study by Asif [131] on Si pop-in was attributed to breakthrough of material which had undergone a phase transformation during indentation.

The onset of plasticity in Si, where sometimes in the loading curve and more often in the unloading curve [145] pop-in was observed, has been attributed to a phase transformation. A large amount of depth recovery during unloading, referred to as "pop-out", resulting in a characteristic reverse force on the indenter has been observed

[68][146]. TEM (transmission electron microscopy) studies of indentations in silicon revealed less evidence of obvious dislocation activity but did show residual highly imperfect, and often amorphous, structures within the indentations, consistent with a densification transformation occurring at the very high hydrostatic stresses produced under the indenter. The reverse force is caused by the relaxation of densified material during unloading. Thus it has been argued that the low-load hardness response of silicon is controlled by a pressure-sensitive phase transformation [68].

Although microcracking has been observed during indentation in Al_2O_3 [68][147], InP and GaAs [134], it has not been considered the cause of pop-in. In a study on Al_2O_3 [68], TEM images showed the presence of a few dislocation loops and microcracks, but the fact that the shear stress value was near the theoretical strength indicated that dislocation nucleation was most likely the cause of pop-in. In the study on InP and GaAs, the microcracks were found at the apex of the impression as observed by XTEM (cross-sectional transmission electron microscopy), however only for high-load indentation. That the discontinuity in the load-displacement curve was not caused by microcracks was suggested by the fact that at low-load there were no observed microcracks but the data collected were similar to the higher load region where microcracks were observed.

The onset of plasticity in sapphire at a critical load of 200 mN which is much higher than that observed by Page et al. (maximum load $\leqslant 8mN$) [68] was attributed to the twinning process [148].

The experimental variability of P_{crit} can be very high as shown in Table 2.6 [67][68][69][76][77][133][134][138]. In the case of GaN not only is there a large variability but question as to whether the material exhibits pop-in [76][77] or not [75]. To attempt to explain this large variability numerous studies on the conditions that effect pop-in has been performed. Among these are the topography of the surface of the sample, environmental conditions, indentation time, velocity of engagement and indenter geometry. The relationships of crystal orientation, dislocation density

and oxide film thickness to the occurrence of pop-in have been reported [70][138]. In addition, the influence of variations in surface chemistry [71], of roughness [132] and for films, the thickness of the film [77][149], the epitaxial interlayer [149], biaxial misfit stress [149], and film quality [77] have been studied in relation to pop-in. The temperature [71] and relative humidity [131] during indentation have been recorded and the influence on pop-in analyzed. The indentation time, measured from when the indentation test starts to the occurrence of pop-in has been recorded where it was found that at lower loads this time increases [71]. The velocity of engagement [150][151] and the radius of the indenter [131][133] has also been found to effect pop-in.

2.2.6 Dislocation Generation

The dislocations generated by indentation have been studied extensively by several researchers. The major research issues that have been explored are the generation mechanisms, the plane and direction the dislocations travel once created, and the anisotropy that the rosette dislocations show.

In a study by Hirsch et al. on GaAs [82], the dislocations due to Vickers indentations were first observed by etching the surface and then a model developed to predict the pattern of the dislocations. It should be noted parenthetically that Vickers indentations are large by comparison to those produced by nanoindentation. The model calculates the resolved shear stress for each point in a region under the indenter for a given applied load and for all possible slip systems. Locations on a given slip system where the resolved shear stress is a maximum are identified. The resolved shear stresses were calculated from the three principal stresses obtained by the solution of the problem of a uniform pressure acting along a parallel strip developed by Nadai [152]. Using this model, the GaAs plastic zone under the indentation was modeled in three regions: 1) an inner region where slip systems cross each other forming locks - this region is strongly work-hardening; 2) an outer region where slip occurs in the material along diverging planes - here slip is limited only by the lattice

friction stress; 3) a rosette slip region where the slip plane is parallel to the surface - here the magnitude of work-hardening depends on the geometry and orientation of the indenter. This plastic zone modeling approach has been used not only in materials with cubic structures but in hexagonal structures as well. For example, in a study of sapphire conducted by Nowak et al. [147] the Hirsch model was modified slightly by multiplying the shear stress by the so-called constraint factor which accounts for the tendency of the indented material to move toward the free surface. This model was successfully used to explain hardness anisotropy and in the study of rosette dislocations. Using plastic zone modeling the hardness anisotropy of InSb [153] and GaAs [154] was attributed to different work-hardening characteristics of the slip system activated in different indenter orientations, and as previously discussed, to the different velocities of the dislocations In(g) and Sb(g). Several studies on rosette dislocations using this model have also been presented. In a study by Doerschel [155] the formation and motion of the rosettes was attributed to microtwinning, and anisotropy in terms of the length of the arms of the rosettes was considered to be caused by the differences in the shear stress acting on the different slip planes. In another study the model of Hirsch was used to show that the dimension of the rosettes was influenced by the oxygen present in the silicon which helped the formation of locks [156]. In addition the dislocation rosettes created in InSb by indentation have been studied as a function of the amount of doping and the annealing temperature used [153]. The plastic zone modeling method has been used not only for Vickers indenters but for spherical [157] and Knoop [154] indenters as well.

The dislocations discussed above are due to applied indenter loads much greater then P_{crit}. This loading results in multiple dislocation activation which can be explained by plastic zone modeling. In the case of pop-in. ideally only one slip system is activated. A model has also been presented to predict this slip system [69][87]. In this method. if the possible slip systems are along different planes it is necessary that indentation be performed on different surface planes. e.g., (0001), $(10\bar{1}0)$ and $(11\bar{2}0)$.

This is because different slip systems may have different values of critical resolved shear stress, thus the slip system where the maximum resolved shear stress acts may not be activated because the critical shear stress for that slip system may be higher than for another. The first step of this method is to calculate the resolved shear stress on all the possible slip systems at the P_{crit} for each surface plane indented. Once the resolved shear stresses are obtained the maximum for each slip system for a particular surface plane is compared with the maximum for the same slip system of another plane. This is repeated for all slip systems and for all planes. Finally the activated slip system will be the one for which the maximum is independent of the surface plane, i.e., its value is constant for each surface plane. This method has been used in a study conducted by Gerberich [69] on Fe-3wt%Si and by Kiely [87] on Au. Gerberich evaluated the state of stress under the indenter in cylindrical coordinates using the Johnson solution of the Hertzian problem [53]. He then determined the resolved shear stress τ_r on any slip plane with normal n and slip direction s by summing the contribution from all components of stress σ_{ij}, viz.,

$$\tau_r = c_{rr}\sigma_{rr} + 2c_{r\theta}\sigma_{r\theta} + c_{\theta\theta}\sigma_{\theta\theta} + c_{zz}\sigma_{zz} \tag{2.13}$$

where c_{ij} are the Schmid factors

$$c_{ij} = \frac{1}{2}\left(n_i s_j + n_j s_i\right) \tag{2.14}$$

The same approach was followed by Kiely [87]. In the Gerberich work only one plane was indented because only two possible slip systems were identified and both had about the same critical shear stress as a result of the cubic structure of Fe-3wt%Si therefore the system with the maximum resolved shear stress was determined to be the active one.

Simulation by numerical analysis of the initial stages of plastic deformation due to an indentation (for a rectangular prism and cylinder indenter) using a quasi-

continuum method has been developed [158]. With this method it was possible to predict the load-displacement curve as well as the Peierls stress and the density of geometrically necessary dislocations beneath the indenter.

2.2.7 Influence of Light

The influence of light on crack propagation and on dislocation generation during indentation has been reported [72][73]. Koubaiti, who used TEM deformation experiments in conjunction with indentation correlated the indentation results to the ratio of the wavelength of the light used to the absorption edge. At a ratio of less than one, dislocation mobility is increased and crack propagation suppressed, as observed in a study conducted by Maeda at al. on GaP [73]. This is referred to as a negative photo-plastic effect (PPE). In the study of Koubaiti on ZnS [72] for ratios greater than one (positive PPE) dislocation mobility decreases and crack propagation increases. These studies enabled the explanation of the softening effect in GaP [73] and the hardening effect in ZnS [72] due to illumination.

Chapter 3

Experiments

3.1 Preparation of ZnO Surfaces

Hexagonal (wurtzite) structure ZnO grown by the seeded chemical vapor transport (SCVT) method was used in the study. A ZnO crystal possesses two distinct polar faces normal to the <0001> axis, a Zn-terminated (0001) face (Zn face) and an O-terminated ($000\bar{1}$) face (O face). Both faces were studied in the present work. The (0001) oriented ZnO wafers were sawn from a boule and then etched in 5 vol % trifluoroacetic acid (F_3CCOOH) and de-ionized H_2O (15 MΩ-cm) to remove about 25 μm from the saw-damaged surface. The oriented crystals were of nominal dimensions 8 x 10 x 0.7 mm. The wafers were processed on both sides by first lapping and then chemomechanical polishing. This provided flat, minimally damaged surfaces which could be then further processed. Lapping was performed using a commercial lapping machine with a cast iron wheel and a 9 μm Al_2O_3/de-ionized H_2O slurry resulting in an additional 50 μm of material removal from each side. This was followed by chemomechanical polishing using a commercial polishing machine and a slurry of a 1:8 ratio of sodium hypochlorite:colloidal silica (9.1 pH). Approximately 25 μm of material from each side was removed under conditions of 1.7 x 10^{-2} MPa. Sets of Zn face and O face wafers were prepared with the following polishing preparations:

1) mechanical polishing with 1 μm diamond abrasive/de-ionized H_2O slurry and 2) chemomechanical polishing as described above. Mechanical polishing was performed using a nylon pad and a pressure of 1.4 x 10^{-2} MPa. Etched surfaces were also prepared after chemomechanical polishing by etching in trifluoroacetic acid/de-ionized H_2O.

3.2 Instrument

The nanoindentation system is composed of a commercially available nanoindenter (Hysitron, Inc.) and an atomic force microscope (AFM) manufactured by Digital Instruments. The Hysitron system includes a signal adaptor, a scanner, a controller, a three plate capacitive load-displacement transducer and an indenter. The main components of this instrument, the three plate transducer and the indenter. will be described in detail later.

In Fig. 3-1 a block diagram of the nanoindenter is shown. The software interface between the atomic force microscope and the Hysitron is made by the signal adaptor while the hardware interface is made by the scanner. Attached to the scanner is the transducer, where the indenter is fixed. Below. brief comments on the individual components of the nanoindenter are made. The indenter is the only component in contact with the material, i.e., it is an interface between the surface of the material sampled and the transducer. The transducer is used to apply a desired load to the indenter and measure its displacement in the z direction. The transducer controller manages the input and output of the transducer (load and displacement as a function of time) which are then sent to the transducer computer which displays the plotted load-displacement data and the signal adaptor that converts the data into a compatible format for the AFM controller. The scanner moves the tip in the x and y directions labeled in Fig. 3-1. The AFM controller receives the coordinates of the indenter position in three dimensions, the z coordinate from the transducer controller

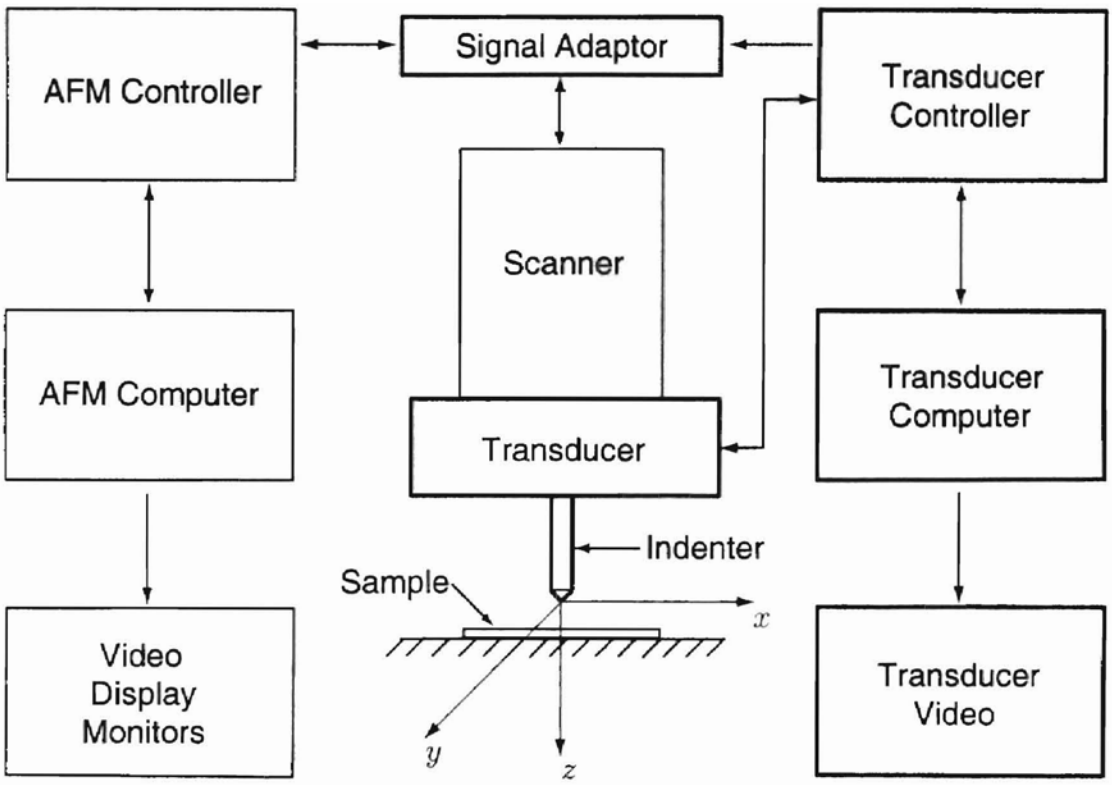

Figure 3-1: Block diagram of the nanoindentation system. The components of the Hysitron system are in bold.

and the x and y coordinates from the scanner, allowing for an image of the topography to be displayed on the AFM monitor. An example of a topography image obtained in situ is shown in Fig. 3-2. There are essentially two computers, the Hysitron computer which controls the load, z direction and time, and the AFM computer which controls the other two directions x and y and the engagement of the tip to the surface (the macroscopic z direction motion).

The maximum load which can be applied by the transducer is approximately 10.7 mN. The range of data points that can be chosen is from 500 to 8000. The resolution stated by Hysitron in the user's manual is less than 1 nN for the load and approximately 0.0002 nm for the displacement. The noise floor is reported to be 100 nN for the load and < 0.2 nm for the displacement (without averaging). This allows

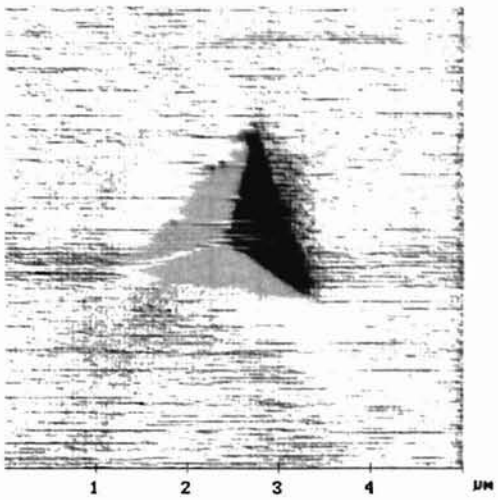

Figure 3-2: AFM topography image of an indentation in ZnO at 3000 μN peak load.

indentation to be performed with maximum loads < 25 μN, and totals depths < 5 nm.

3.2.1 Transducer Operation

The essence of the nanoindenter is a three plate capacitive force/displacement transducer. This transducer designed by Hysitron has the advantage of providing high sensitivity. large dynamic range, and a linear displacement output signal. The low sprung mass (200 mg) of the transducer's center plate minimizes the sensitivity of external vibrations. and allows for light indentations < 25 μN to be made.

The transducer is shown in Fig. 3-3 and consists of one mobile electrode attached to a thin plate acting as a flexible spring (referred to as the *pickup electrode* or *center plate*), and two fixed outer electrodes (referred to as *drive plates*). The indenter is attached to the center plate by a screw so that the load and displacement applied to the center plate correspond to the load and displacement of the indenter. The two outer electrodes are driven by AC signals 180° out of phase. Since the fixed plates are

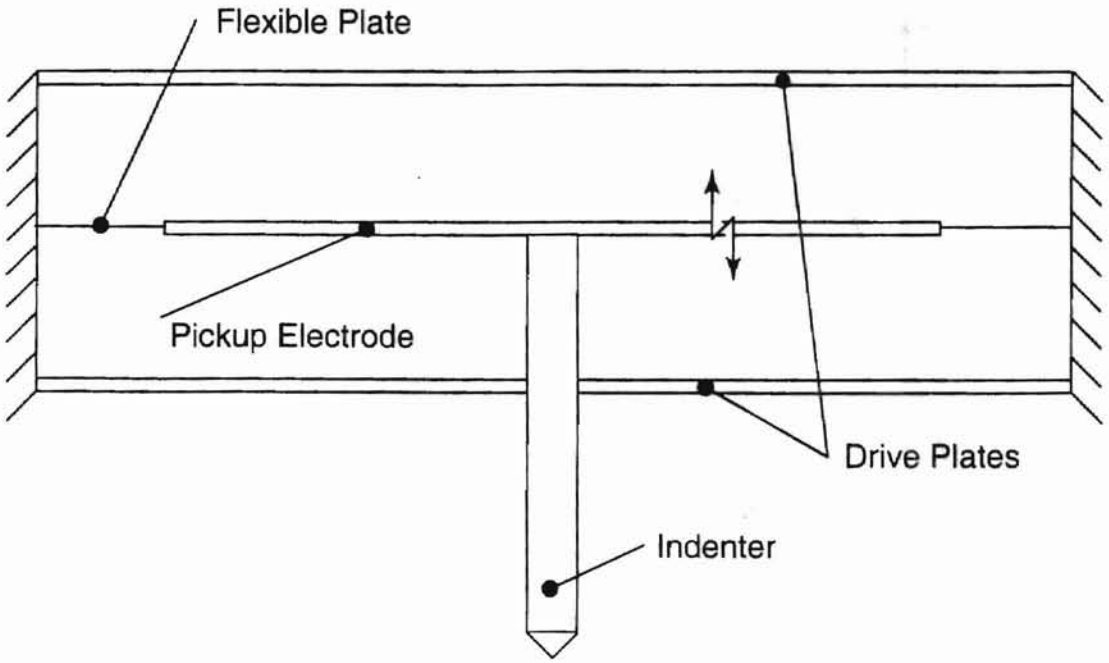

Figure 3-3: Three plate capacitive force/displacement transducer

parallel and the distance between them is much smaller than the area of the plates, it is possible to model them with the theory of infinite parallel planes carrying an equal but opposite uniform charge density. This enables one to consider the electric field constant and the potential to vary linearly from the maximum (equal to the applied signal) at the drive plate to zero at the position centered directly between the drive plates. The distribution of the potential is shown in Fig. 3-4. An important design consideration allows one to consider the potential of the center plate (V_{CP}) equal to the potential present at its position between the drive plates. This allows the central plate displacement to be obtained by measuring its potential. The load applied to the center plate is regulated by the potential applied to the driver plates once the position of the center plate is known.

The user inputs to the control software are the load pattern and the number of load-time data points to be taken. An example of a load pattern is shown in Fig. 3-5. When the command to perform the indentation is given the software determines the

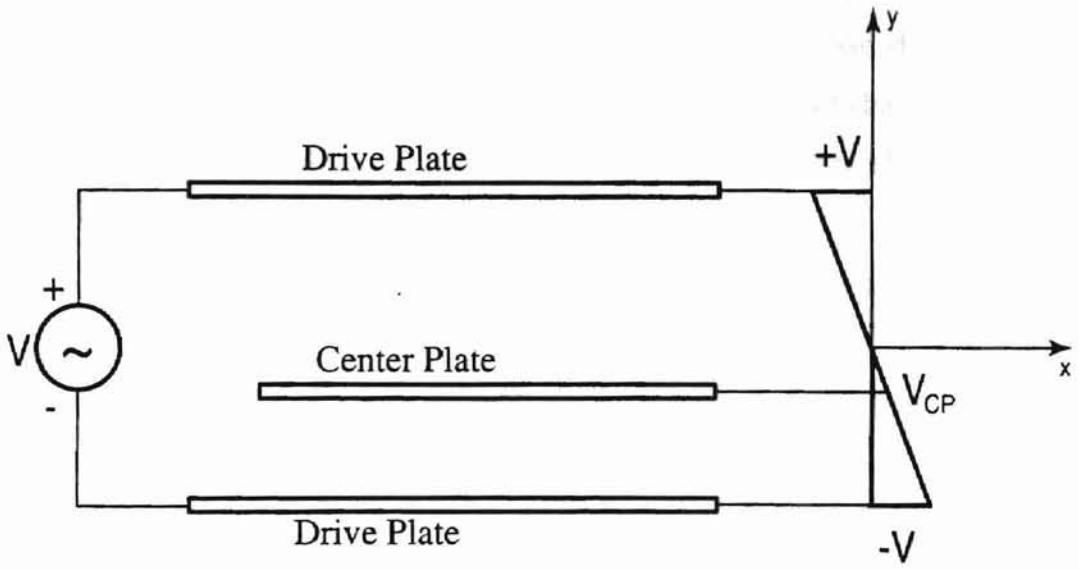

Figure 3-4: Distribution of the electric potential between the drive plates. V is the AC signal applied to the drive plates which are 180° out of phase and V_{CP} is the potential of the center plate.

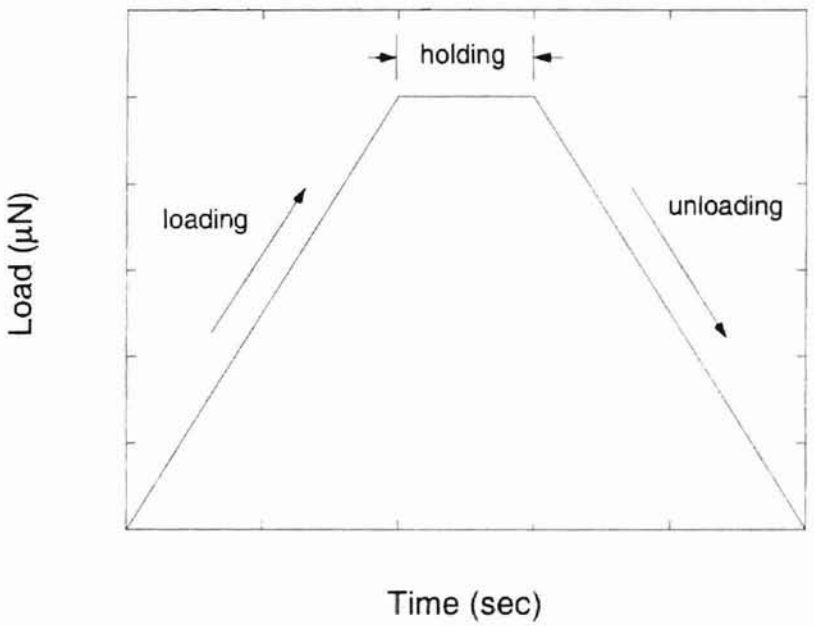

Figure 3-5: Example of a load pattern

position of the center plate and sets it to zero displacement. From the position of the center plate the signal needed at the drive plate to apply the load described in the first point of the discrete load pattern is calculated. The effect of changing the signal at the driven plate will result in a displacement of the center plate after which a new calculation of the signal is made to follow the load pattern. The load-displacement data for each time step is recorded resulting in the load-displacement curve as shown in Fig. 3-6.

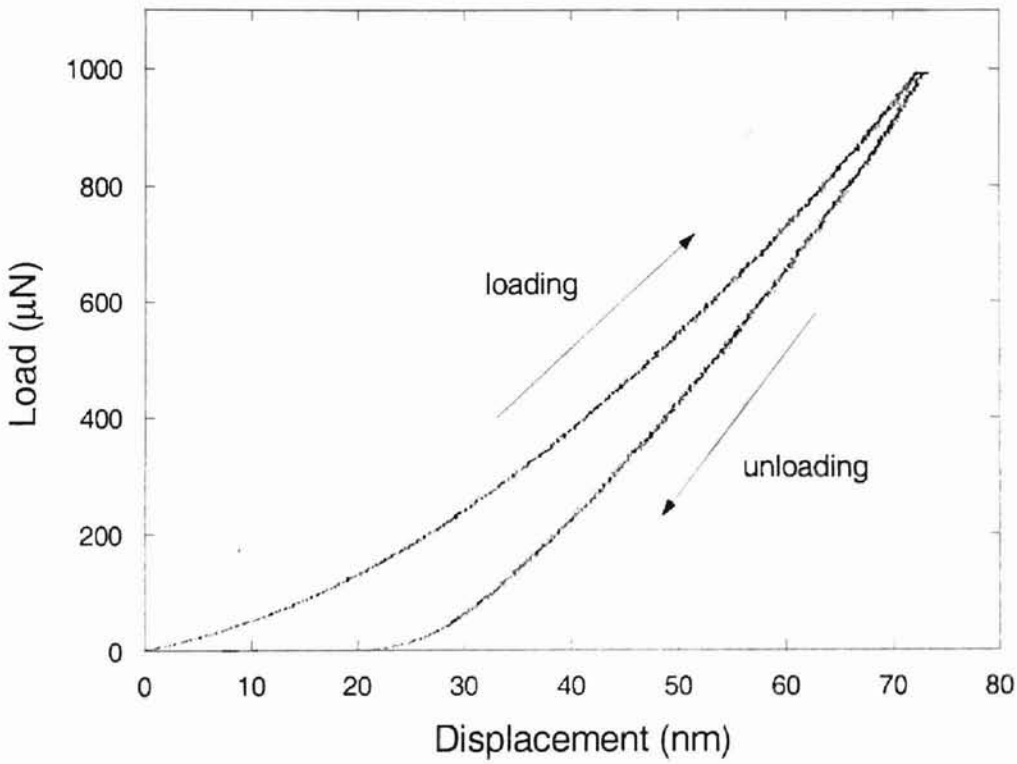

Figure 3-6: Load-displacement curve for a peak load of 1000 μN in Fused Silica

3.2.2 Indenter

In this study a Berkovïch indenter was used. The indenter material is diamond which has a high elastic modulus (E=1141 GPa [50]), high hardness, low friction and low

surface roughness, all the characteristics needed by an indenter. Another important characteristic is a well-defined geometry so that the impression left on the material is well defined. The Berkovich geometry (shown in Fig. 3-7) is a three-sided pyramid with a 65.3° angle between the altitude of the lateral face (segment $\overline{AH}$) and the vertical axis (segment $\overline{AO}$) and a 76.9° angle between any side and the vertical axis. An advantage of the three-sided pyramid is a sharply pointed tip compared with the

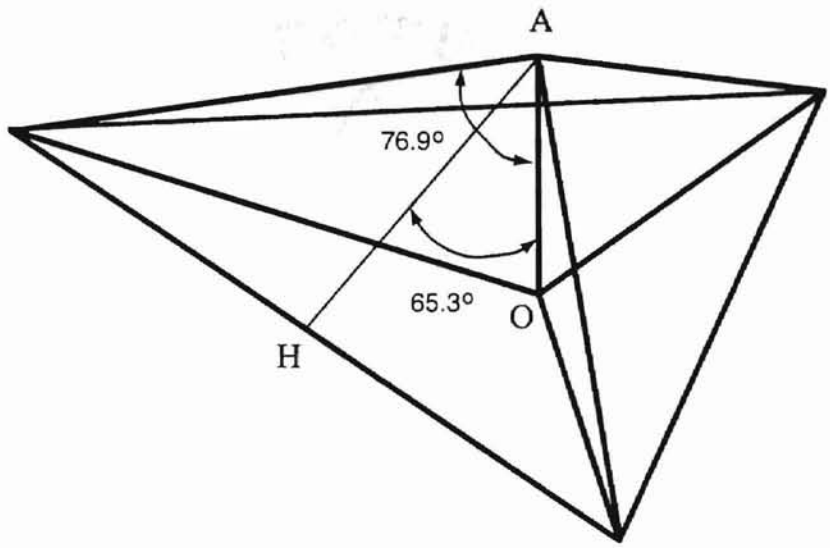

Figure 3-7: Geometry of the Berkovich indenter

four-sided pyramid geometry of Vickers and Knoop, as a result of the fact that three non-parallel planes intersect at a single point. This fact makes the Berkovich easy to manufacture. Another advantage of this geometry is that the area function which is the cross-sectional area of the indenter as a function of the distance from its tip, is similar to the Vickers area function. An AFM image of the indenter used in this study is shown in Fig. 3-8.

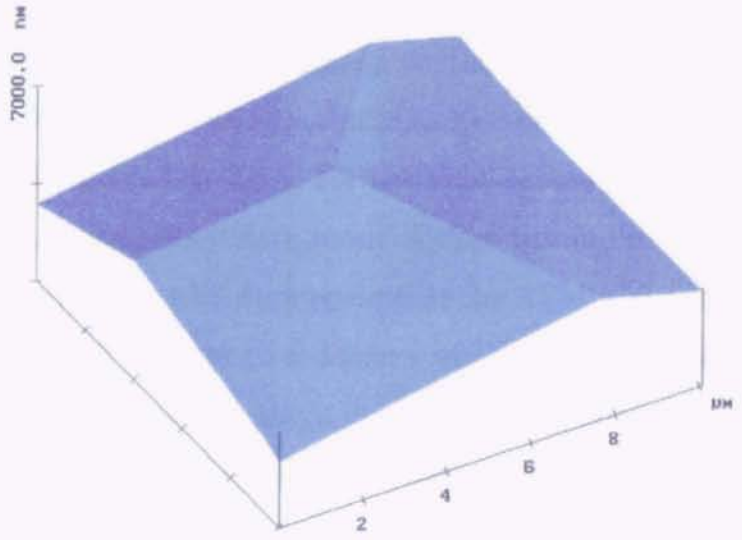

Figure 3-8: AFM image of the Berkovich indenter used

3.3 Detailed Procedure for the Nanoindentation Experiments

This section describes in detail the steps performed during a set of experiments, from the set-up of the machine and software, to the indentation of the material and storage of the results.

Before fixing the indenter on the transducer, the tip of the indenter is wiped with a tissue wetted with a cleaning solution of 70% methanol and 30% ethyl alcohol and then dried by blowing it with ultra purified nitrogen. Then the transducer with the indenter mounted on it is fixed to the scanner, which is secured to the AFM. Once the scanner is attached to the AFM the controller of the transducer is connected and turned on. The force gain, displayed on the transducer controller shows the load applied to the transducer, and initially should correspond approximately to the weight of the indenter (251.6 mg). This provides a good check to confirm that all the connections are working properly. Once the value of the force gain has been checked,

it is reset to zero. Then the tip is focused with the AFM optical camera for viewing when approaching the sample surface.

In the next step, the sample is placed on the vacuum chuck with the room in darkness. Indications from the minor studies discussed in Chapter 4 are that the ZnO surface can be altered by light. For the same reason all the samples are stored in a desiccator in a completely dark room. Before turning the room lights on after the sample is mounted the enclosure protecting the AFM is closed.

The tip is manually brought to a distance of about 70 μm from the surface with the AFM motor, which controls the z direction during the engagement procedure. This is made possible by the AFM optical camera which allows one to see the mirror image of the tip reflected from the sample surface at a distance of approximately 70 μm. During the manual approach two images of the tips (the actual one and its reflection appear) on the AFM monitor when the tip is close to the surface of the sample. Then the approach is stopped and before using the automatic engaging procedure, the system is allowed settle, warming up for about one hour.

The system is allowed to warm up so that the thermal drift due to the different temperatures of the tip, sample, transducer, scanner, and the machine frame (all objects under the enclosure) is minimized. The effect of the thermal drift can be seen by the continuous variation of the force gain which decreases with time. When the value of the force gain is constant (after about one hour) the machine is ready to indent and therefore the value of the force gain is again set to zero.

At the beginning of each set of indentation experiments, before engaging the surface of the sample, an "air indentation" is made. The load pattern consists of loading and unloading, without any holding, at a peak load of 20 μN and with a load rate of 10 μN/sec. The load-displacement data for such an indentation should result in an increasing displacement with constant load equal to zero. If the load-displacement data shows an increasing or decreasing load during the air indentation the electrostatic force constant (EFC) must be adjusted to result in a constant zero

load. A typical value of the EFC is 0.02976 $\mu N/V^2$.

To engage the surface, two inputs are entered, 1) the velocity of engagement of the tip, entered into the AFM software and 2) the set point inputted in nA equivalent to mg force, entered into the Hysitron software. The set point is the load measured by the transducer at which the vertical motor should stop. These two values must be chosen carefully to avoid false engagement, and more importantly, to not damage the sample surface by introducing plastic deformation. It was noticed that with a high velocity of engagement, e.g., 7 μm/sec, the set point must also be high, e.g., 200 μN (20 nA) to avoid false engagement. These conditions however caused plastic deformation to occur on the surface of the material, as was evidenced by a residual imprint which could be seen. Useful conditions were found to be a velocity of 1 μm/sec and the load of engagement of 20 μN. Once these two parameters are entered, and the scan size confirmed to be zero so that the tip would not scan the surface with a load of 20 μN, the engagement could be made. As soon as the tip comes in contact with the surface and the z motor stops, the current set point is changed to 0.8 - 1 nA, corresponding to about 8 - 10 μN load applied to the tip, and the scan size is changed to 5 μm.

After engaging the surface, it is scanned to measure the topography. This takes about ten minutes. While the surface is being scanned, the load pattern (load-time sequence), the number of data points and the drift correction are set on the Hysitron computer. At the beginning of the indentation experiments the load pattern shown in Fig. 3-9 was used. This sequence was the same as that used in the experiments of Oliver and Pharr [50]. The indenter is loaded and unloaded three times with the unloadings terminating at 10% of the peak load. This is to assure that the unloading data used to calculate the elastic modulus is mostly elastic. After the third unloading, the load is held at 10% of the peak load, while the variation of displacement is monitored so as to evaluate the presence of thermal drift during the indentation. Following the hold period, the indenter is loaded for a fourth and final

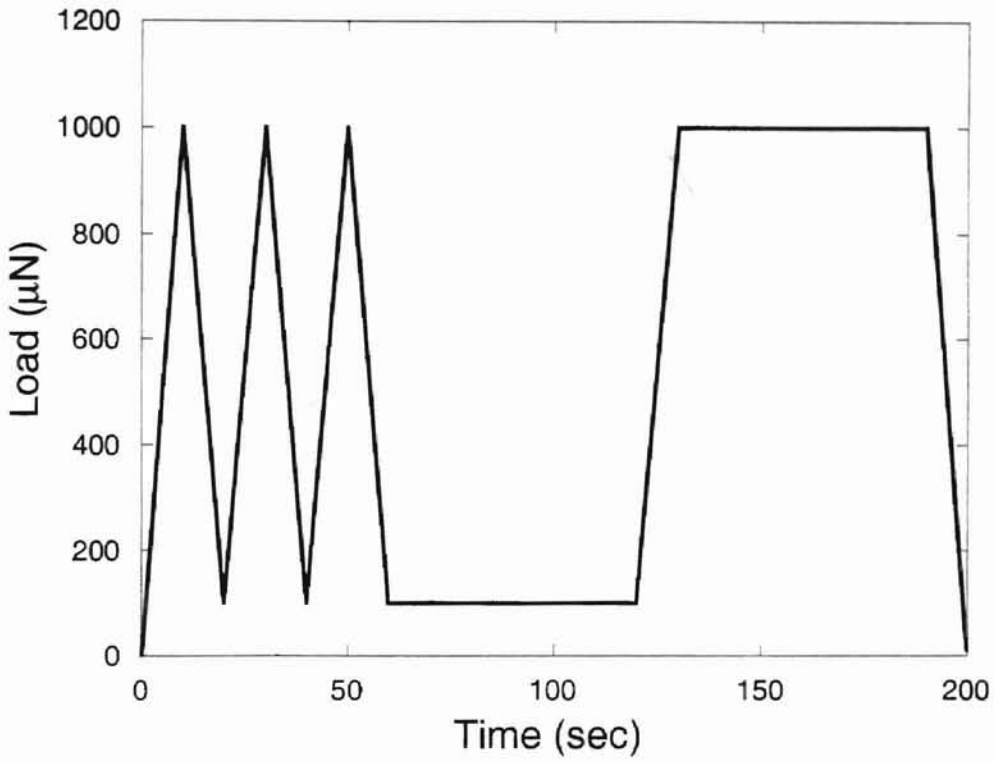

Figure 3-9: Load pattern used by Oliver and Pharr

time, and then held at the peak load to allow any final time-dependent plastic effects to diminish. The indenter is then completely unloaded. This load pattern was soon dismissed in favor of a simpler one shown in Fig. 3-10. As a result of the shorter time, the simpler load pattern minimized problems with drift, and reproduced the results obtained with the load pattern of Oliver and Pharr. The load pattern which was used consisted of a loading portion, a holding time equal to half the time of loading and an unloading portion. The loading rate was chosen to be 100 μN/sec, which was found to be ideal for the range of indentations performed (200 to 3000 μN). For the shallow depths the indentation was performed in 5 sec and at the largest depth the indentation took 75 sec. The number of data points selected was 3000 and the drift correction was set to a maximum drift rate of 0.1 nm/sec and a maximum time of 20 sec for all the indentations. When the drift correction is selected and the command to

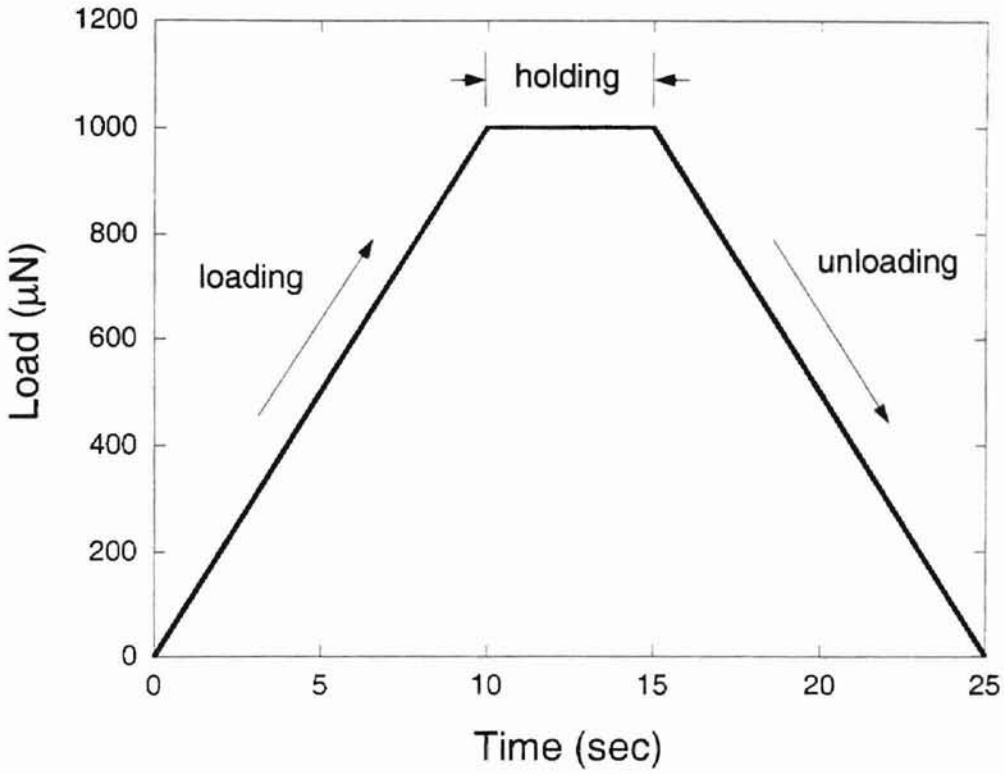

Figure 3-10: Load pattern used for a peak load of 1000 μN

make an indentation given, the transducer maintains the load at zero before indenting for a period of 5 sec after which the drift rate of the displacement is evaluated. If the drift rate is greater than 0.1 nm/sec the load is maintained for another 5 sec, otherwise the indentation is performed. For the case when the load is held at zero for 20 sec (4 cycles) and the drift rate is still greater than the prescribed one, the instrument will perform the indentation and correct the data using the last value of drift rate obtained. The set of experiments reported in this study do not involve any where the drift rate was higher than the prescribed value. When the drift rate is below that prescribed, the instrument corrects the data using the measured value, which is assumed to be constant throughout the test.

When the surface is completely scanned over the 5 μm x 5 μm region, the topography is evaluated and the scanner located to a flat region. Then the scan size and

the internal and proportional gains of the scanner are set to zero just before the indentation is performed. This is to stop the scanner and assure that no compliance is added to the indenter. Then the indentation is performed. Once the indentation is completed the scan size, internal and proportional gains are changed back to their original values, so that an in situ image of the indentation can be taken.

After the indentation is completed, the load-displacement curve is plotted on the Hysitron monitor, and the value of the reduced elastic modulus (E_r), hardness (H), contact depth (h_c) and measured stiffness (S), evaluated as described in Chapter 2 are given. These values are then stored in a database.

Chapter 4

Discussion of Results

4.1 Load - Displacement Analysis

A typical load-displacement curve for a peak load of 200 μN on ZnO is shown in Fig. 4-1. In this plot, as well as in all the indentations performed on ZnO, a sudden increase in penetration depth at a given load P_{crit} (pop-in) was observed. Pop-in divides the loading portion into two regions, a purely elastic region before the onset of plasticity and an elasto-plastic region after it. The increase in penetration at constant peak load is due to material creep during the hold of the peak load (Fig. 3-10).

4.1.1 Elastic Loading

To verify the elasticity before pop-in several indentations were made at loads less then 150 μN. An example of the load-displacement curve is given in Fig. 4-2. As can be seen the loading and unloading portions of the load-displacement curve overlap, and after indentation no permanent deformation of the surface was observed. This result enabled consideration of the indentation process before the onset of plasticity as an elastic contact problem for which the Hertzian solution could then describe the load-displacement curve [53]. The Hertzian solution for a non-rigid, spherical indenter in

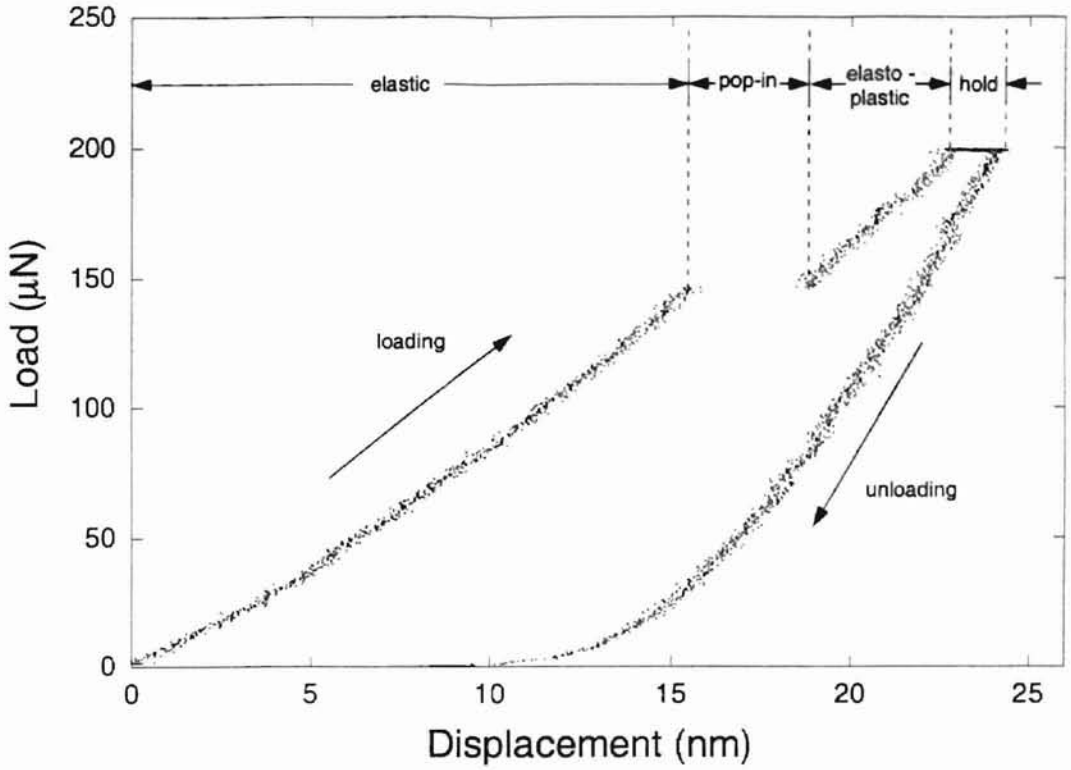

Figure 4-1: Typical load-displacement curve for ZnO

contact with an elastic half-space is

$$P = \frac{4}{3} E_r \sqrt{R h^3} = \left(\frac{4}{3} E_r \sqrt{R} \right) h^{\frac{3}{2}} \tag{4.1}$$

where E_r is the reduced modulus as defined by Eqn. (2.3), and R is the radius of the spherical indenter. At shallow indentations the Berkovich indenter can be considered a sphere with a radius equal to the radius tip.

The radius of the Berkovich indenter was estimated by fitting the area function of the indenter, calculated in Appendix A, with the area function of an ideal sphere, evaluated geometrically as shown in Fig. 4-3. The area function was fit for h_c between 4.7 nm, the minimum considered in the calibration process, and 18 nm (note the onset of plasticity occurred at a depth of about 16 nm). As can be seen in Fig. 4-3 the area

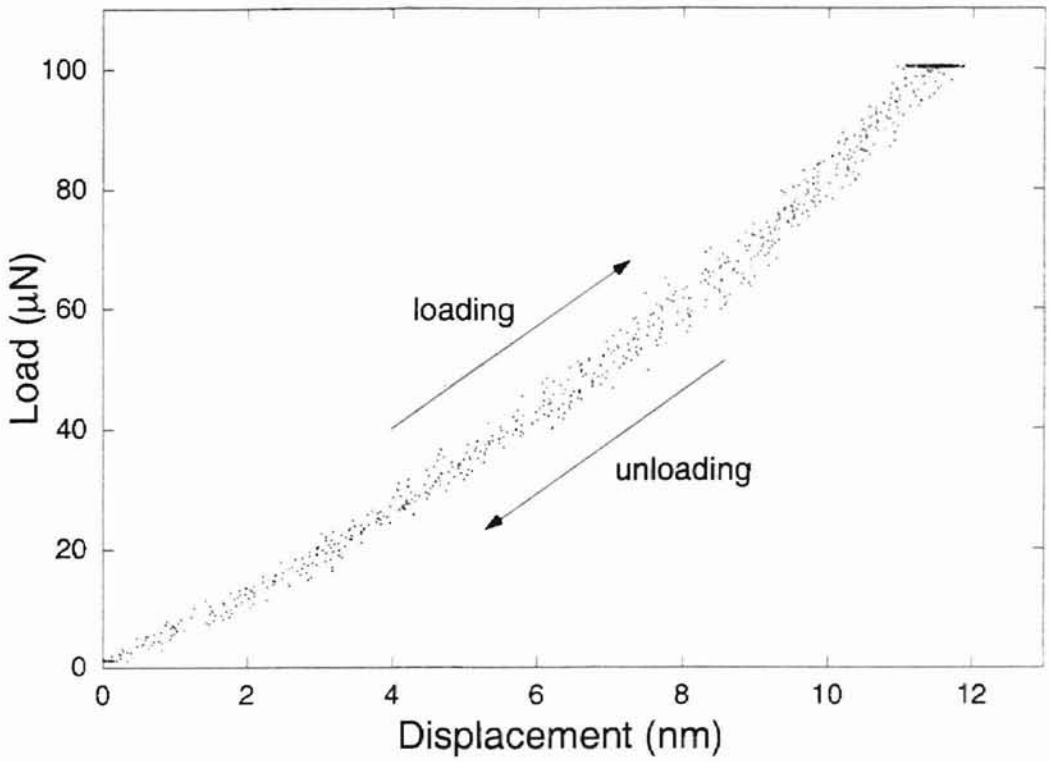

Figure 4-2: Indentation in ZnO at 100 μN peak load

function for an ideal sphere is

$$A = -\pi h_c^2 + 2\pi R h_c \tag{4.2}$$

where the resultant radius of the sphere, R, was found to be about 270 nm. The plot of the area function for the Berkovich indenter and for the ideal sphere of radius 270 nm is shown in Fig. 4-4.

In Fig. 4-5 the Hertzian solution given by Eqn. (4.1) has been compared to the measured load-displacement data. Here, $R = 270$ nm, and $E_r = 125.5$ GPa (calculated from reported values [18]). The two curves are seen to follow the same path with an off set of about 0.5 nm which could be explained by an offset in the force transducer. This result confirms the purely elastic behavior of ZnO before pop-in.

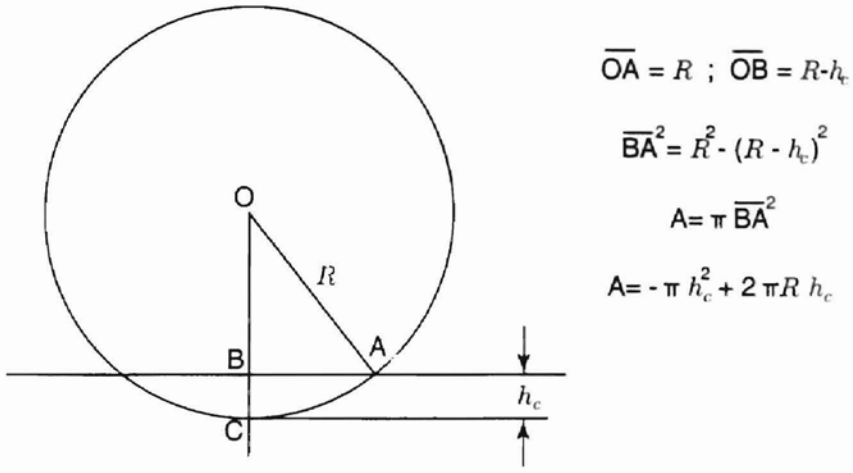

Figure 4-3: Area function of an ideal sphere calculated geometrically

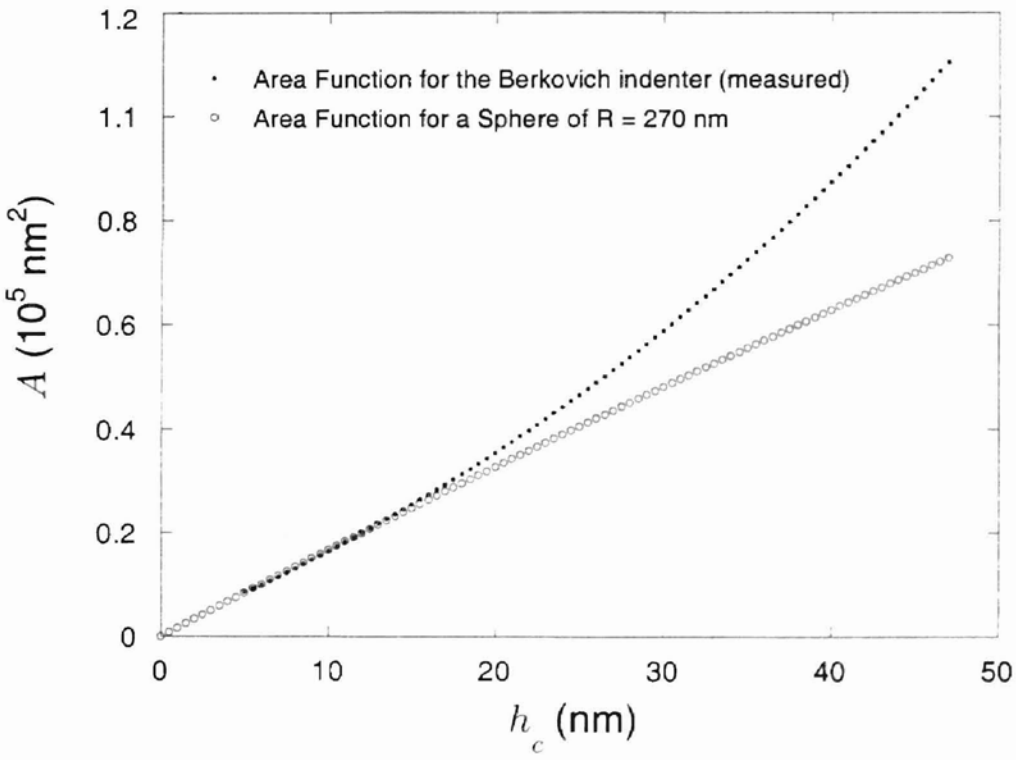

Figure 4-4: Comparision between the measured area function of the Berkovich indenter and the calculated area function of an ideal sphere of radius 270 nm

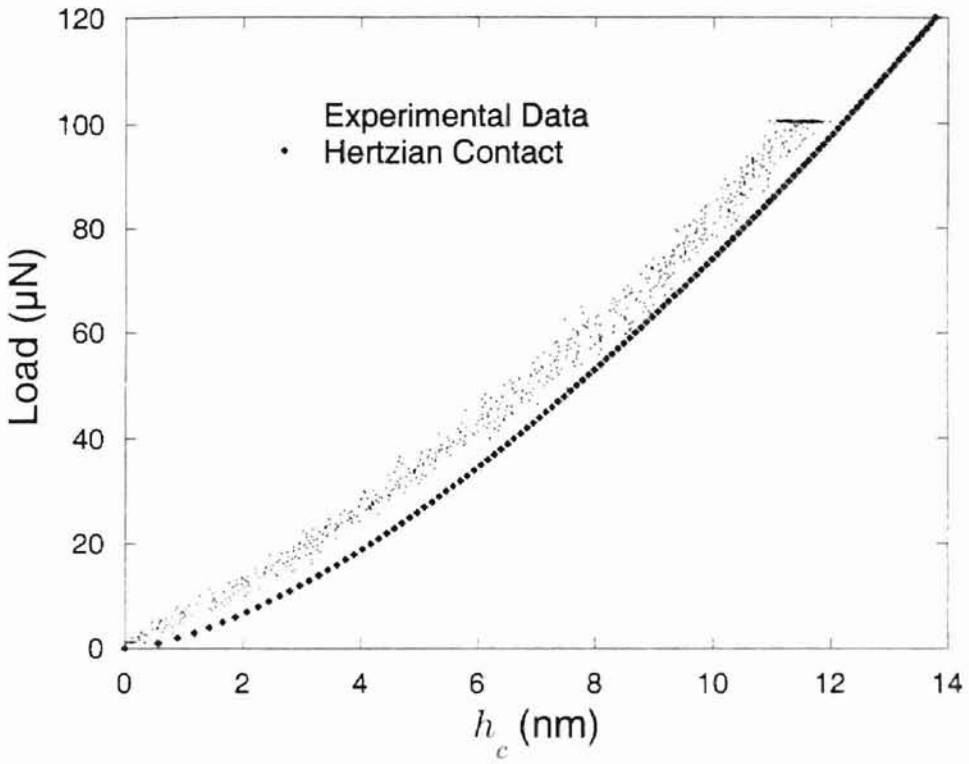

Figure 4-5: Comparison between the experimental data and the Hertzian solution

4.1.2 Pop-in

In Fig. 4-6 an indentation stopped just after pop-in is presented. In this case, the

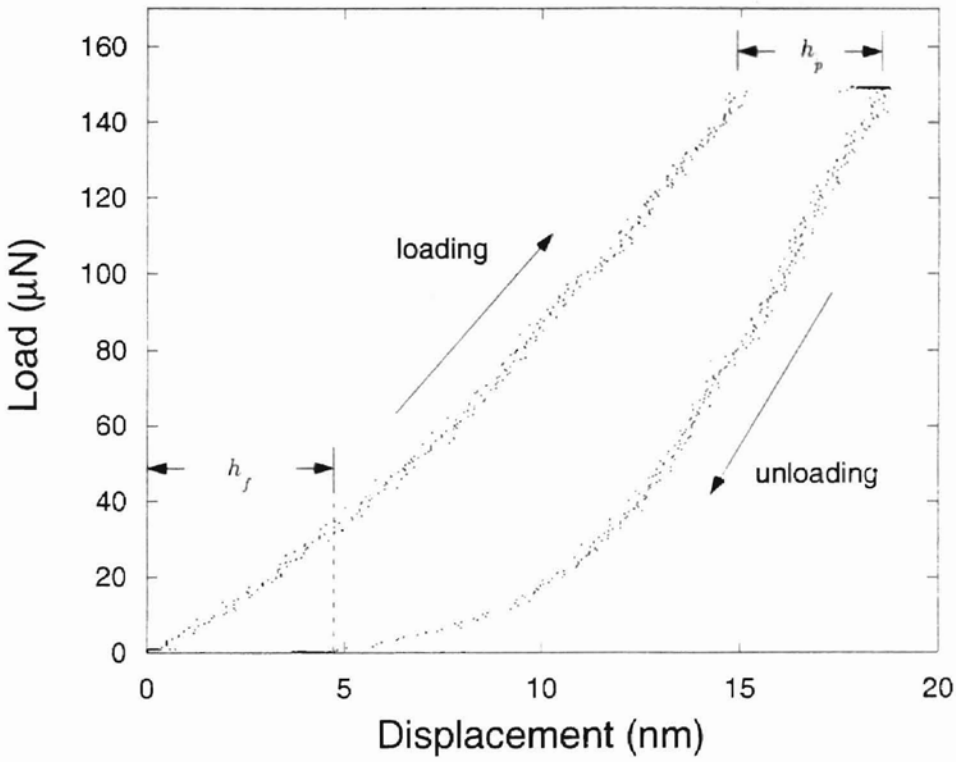

Figure 4-6: Indentation stopped just after Pop-in

unloading portion of the load-displacement curve does not overlap the loading part. Moreover the in situ measurement of the surface topography showed a permanent imprint with a depth equal to the final depth h_f. Note that the depth of the pop-in h_p is approximately equal to the final depth h_f.

4.2 Investigation of the Two Polar Faces of ZnO

The first study conducted on ZnO was to determine if any difference in the mechanical response, i.e., elastic modulus (E), hardness (H), and onset of plasticity (pop-in), of

the two polar faces could be measured by nanoindentation. This study was motivated by the fact that several differences between the polar faces of ZnO were observed as can be seen in Table 2.5, and by the fact that differences in hardness between the polar faces of GaP [73], GaAs [82], and InSb [81] have been reported.

In this study, both the Zn-terminated (0001) and O-terminated ($000\bar{1}$) faces of ZnO prepared by chemomechanical polishing were investigated. The range of indentations performed on both faces was from 200 - 3000 μN, corresponding to a contact depth of 15 - 130 nm. The smallest indentation was chosen with a peak load higher than the P_{crit}, so that plastic deformation would occur and hardness could be measured.

4.2.1 Measured Hardness

Results of hardness as a function of contact depth are shown in Fig. 4-7, where the error bars are based on one standard deviation of about fifteen experiments per point. The two faces did not present discernible differences in hardness, but a slight decrease for both faces at greater depths can be inferred. The difference in the mean value of hardness between the indentations at approximately 18 nm and 125 nm was 18.6% for the Zn face and 16.3% for the O face. The hardness was found to be 5.3 $\pm$ 0.3 GPa at about 125 nm, and 6.2 $\pm$ 0.4 GPa for depths between approximately 18 and 60 nm. These values of hardness were comparable to the only reference value found on ZnO of 2 GPa [15], obtained by Vickers indentation and therefore for much larger and deeper indentations. The hardness results are summarized in Table 4.1.

A plausible explanation of why no difference between the two faces was observed is that at the depth scale investigated the dislocations generated during the onset of plasticity do not interact with each other. This may be due to only a few dislocations being generated or may be because the dislocations move on only one slip system and therefore are parallel to each other. For GaP [73], GaAs [82], and InSb [81] the difference in hardness between the two faces was attributed to differences in velocities

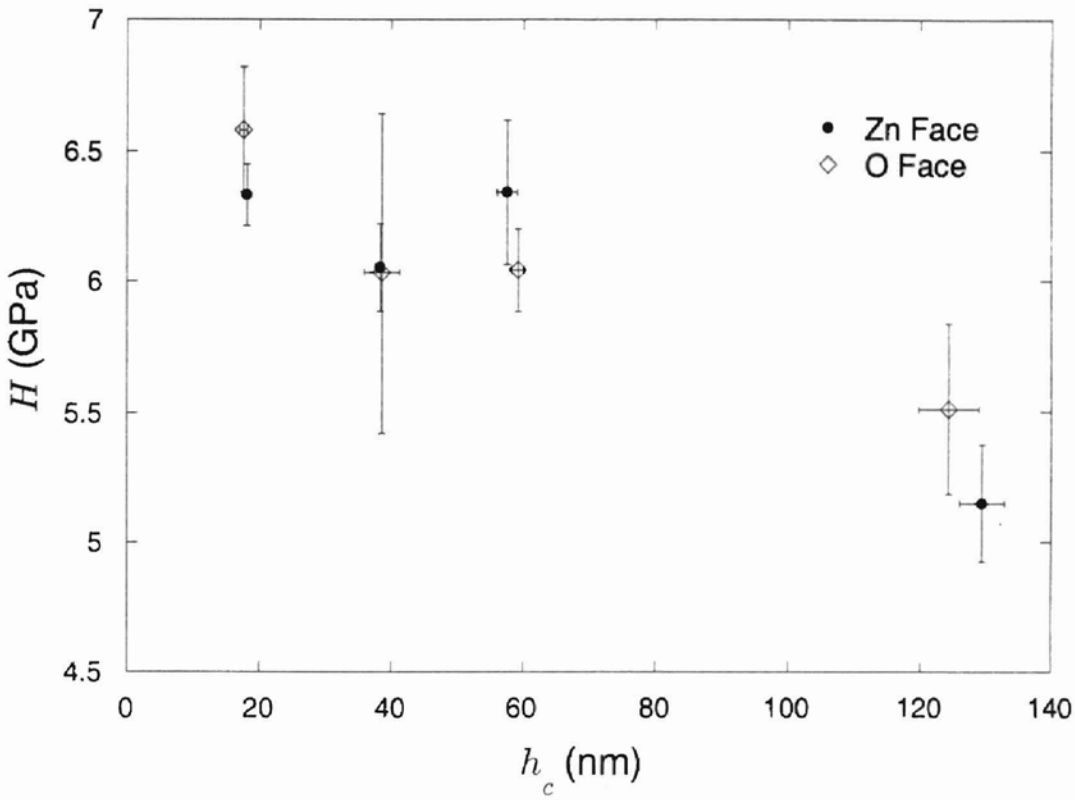

Figure 4-7: Hardness versus contact depth of the polar faces of ZnO

between the X dislocation and the Y dislocation (for the XY material), which causes the dislocations on one face to interact with each other earlier than on the other face, with the result being a difference in hardness between the two faces.

	H (GPa)		
Depth	18-60 nm	125 nm	Bulk [15]
ZnO	6.2 ± 0.4	5.3 ± 0.3	2

Table 4.1: Hardness results of the two polar faces of ZnO

4.2.2 Measured Elastic Modulus

The elastic modulus for bulk ZnO has been reported to be 123.0 GPa [18] (Reuss scale) as listed in Table 2.2. Fig. 4-8 shows the elastic modulus as a function of

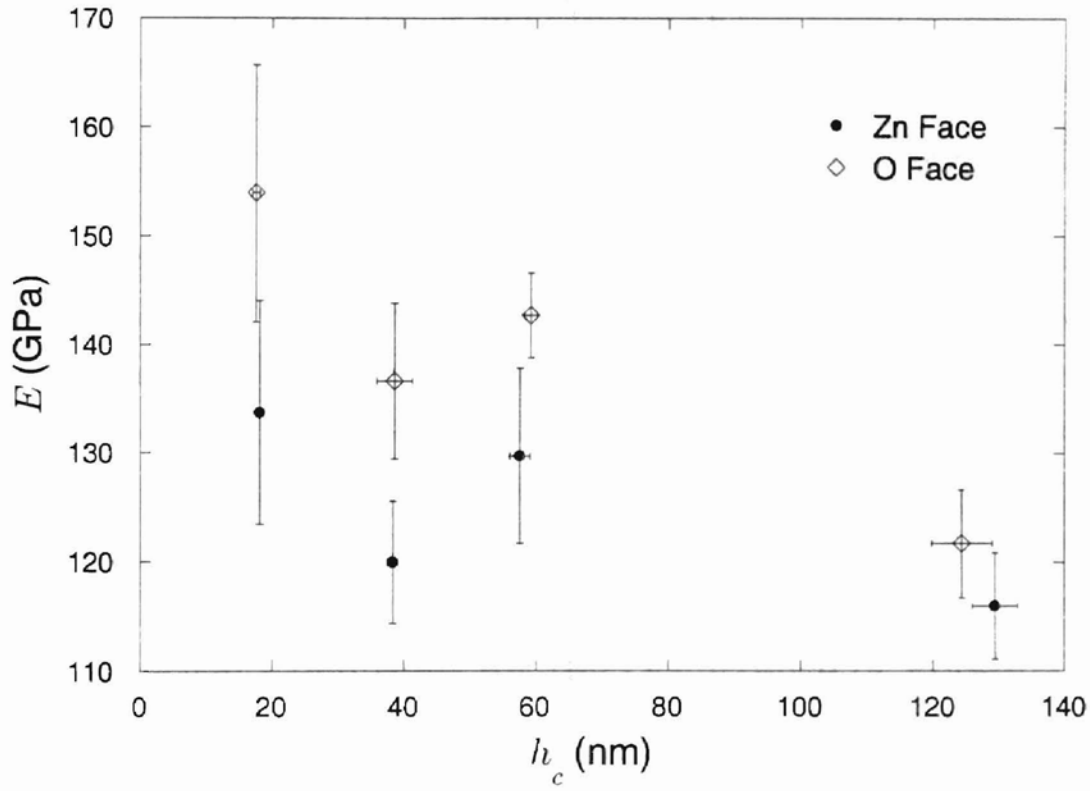

Figure 4-8: Elastic modulus versus contact depth of the polar faces of ZnO

contact depth obtained for both faces. The error bars are again based on one standard deviation of about fifteen experiments per point. At a contact depth of 125 nm the moduli found for both faces are in agreement with the reported value, E=116.0 $\pm$ 4.9 GPa for Zn face and E=121.7 $\pm$ 5.0 GPa for O face. The O face was found to have a higher elastic modulus over the entire range of investigation, and at shallow depths the difference of the mean values between the two surfaces increases to 13.1% at a contact depth of about 18 nm (E=133.7 $\pm$ 10.3 GPa for Zn face, and E=153.9 $\pm$ 11.8 GPa for O face). The elastic modulus results are summarized in Table 4.2.

A plausible explanation regarding the observed difference in elastic modulus between the polar faces could be differences in stoichiometry, bonding or simply the

	E (GPa)		
Depth	18 nm	125 nm	Bulk [18]
Zn face	133.7 ± 10.3	116.0 ± 4.9	
O face	153.9 ± 11.8	121.7 ± 5.0	
ZnO			123.0

Table 4.2: Elastic modulus results for the two polar faces of ZnO

difference in atomic arrangement of the two surfaces as a result of reconstruction and relaxation. For polar materials the surface atoms undergo a process of reconstruction and relaxation needed to eliminate the dipole generated through the crystal from having a cation or anion termination and to produce a stable surface [159]. No definitive explanation however can be given with the available understanding of the surface compositions.

4.2.3 Critical Conditions for the Occurrence of Pop-in

In all the experiments performed, the presence of pop-in was observed. The critical load for pop-in was found to differ for each of the faces, where P_{crit} was 150 ± 17 μN at a depth of 16 ± 1 nm for Zn face, and 166 ± 30 μN at a depth of 17 ± 3 nm for O face. Table 4.3 summarizes the values of the critical load (P_{crit}) and depth (h_{crit}) for the two faces of ZnO. These results are discussed in the next section.

	$\mathbf{P_{crit}}$ **(μN)**	$\mathbf{h_{crit}}$ **(nm)**
Zn face	150 ± 17	16 ± 1
O face	166 ± 30	17 ± 3

Table 4.3: Pop-in results for the two polar faces of ZnO

4.3 Pop-in and the Onset of Plasticity

4.3.1 Dislocation Nucleation

As was discussed in Chapter 2, one of the causes of the sudden increase in displacement at a critical load is dislocation nucleation. For this to be the case for ZnO, two observations should be made, 1) elastic behavior before the onset of plasticity and 2) agreement between the measured maximum shear stress under the indenter and the theoretical shear strength (ideal shear stress, if slip is assumed to occur by the translation of one plane of atoms over another in a perfect lattice).

The observation that the load-displacement data indicates purely elastic behavior before pop-in has been made and is shown in Fig. 4-2. Next, a simple comparison of the maximum shear stress under the indenter at the onset of pop-in and the theoretical shear stress required to cause interatomic slip must be made. An estimate of the maximum shear stress, assuming the material is isotropic and considering elastic contact between a spherical tip and a flat surface can be made using Eqn. (2.6) from Hertzian contact theory

$$\tau_{\max} = 0.31 p_m = 0.18 \left(\frac{P_{crit} E_r^2}{R^2} \right)^{1/3} \tag{4.3}$$

where the reduced elastic modulus (E_r) was considered equal to 125.5 GPa [18] for both faces, and the radius of the spherical tip (R) is 270 nm, as estimated earlier. Using the values in Table 4.3 for P_{crit} one obtains τ_{max} = 5.7 GPa for the Zn face and τ_{max} = 5.9 GPa for the O face. A simple estimate of the theoretical shear stress can be made using Eqn. (2.8)

$$\tau_{theo} = \frac{G}{2\pi} \tag{4.4}$$

where the shear modulus (G) was considered equal to 45.3 GPa [18]. Therefore τ_{theo} = 7.2 GPa and indicates agreement with the magnitude of the estimated maximum shear stress under the indenter. It should be noted however that these calculations

are a coarse approximation that indicate that it is reasonable to assume that dislocation nucleation is the cause of the onset of plasticity in this case. Later, a better approximation based on the prediction of the active slip systems, and a calculation of the critical resolved shear stress on these systems will be presented.

4.3.2 Repeatability

In Table 2.6 the critical load and depth of the occurrence of pop-in and the range of the critical load for several materials were presented. As can be seen the measured range of the critic load was from a minimum of 8% for SiC [68] to a maximum of 77% for Au [67]. The cause of this variability was attributed to numerous factors including the topography of the sample surface, environmental conditions, indentation time and velocity of engagement.

Care was taken to minimize the measured variability caused by the above-mentioned factors. Each indentation was repeated approximately fifteen times, using the identical procedure. To minimize the effects of variations in surface topography the region to be indented was first scanned to confirm the presence of a flat area. If debris or unusual surface roughness was observed the indenter was withdrawn and moved to another region until a flat area was found. The environmental conditions were not controlled, but the temperature and the relative humidity under the enclosure of the instrument were measured. The temperature was constant at 82°F after the warm up of the instrument for about one hour, and the relative humidity varied from day to day from 6% to 29%. The loading rate was maintained constant at 100 μN/sec for all indentations so that for the same elapsed time (measured from when the indentation test started) the same load was applied. In addition, the time from when the surface was engaged to the start of the indentation was controlled and kept constant as well. The velocity of engagement was kept as low as possible, 1 μm/sec, and was the same for all indentations.

All the indentations of the polar faces were made using the above precautions.

	$\mathbf{P}_{crit}$		$\mathbf{h}_{crit}$	
	μN	Range %	nm	Range %
Zn face	150 ± 17	± 11.3	16 ± 1	± 6.2
O face	166 ± 30	± 18.1	17 ± 3	± 17.6

Table 4.4: Critical load and depth results for the two polar faces of ZnO

The range of critical values observed for pop-in are shown in Table 4.4. Comparing the range of these results to the ones in Table 2.6, a better level of repeatability was reached.

4.3.3 Maximum Pressure ($\mathbf{p}_0$)

Perhaps a more appropriate measure of the onset of plasticity or pop-in is to use some form of pressure, dividing the critical load by an area so as to obtain the state of stress under the indenter. To determine this state of stress, and then the resolved shear stress on the various slip systems, the distribution of the applied load by the indenter on the surface must be known. Consider again the contact between a non-rigid sphere and an elastic half-space as shown in Fig. 4-9. The Hertzian contact theory can be used to obtain the pressure distribution under the indenter. The pressure distribution proposed by Hertz, which satisfies the boundary condition for displacements within the contact is elliptical and given as

$$p\left(r\right) = p_0 \left\{1 - \left(\frac{r}{a}\right)^2\right\}^{1/2} \tag{4.5}$$

where p_0 is the maximum pressure under the indenter, r is the radial coordinate and a is the radius of contact as shown in Fig. 4-9 and Fig. 4-10. The P_{crit} can be expressed as the integral of the pressure distribution over the contact area, viz.,

$$P_{crit} = \int_0^a p(r) 2\pi r dr = \frac{2}{3} p_0 \pi a^2 \tag{4.6}$$

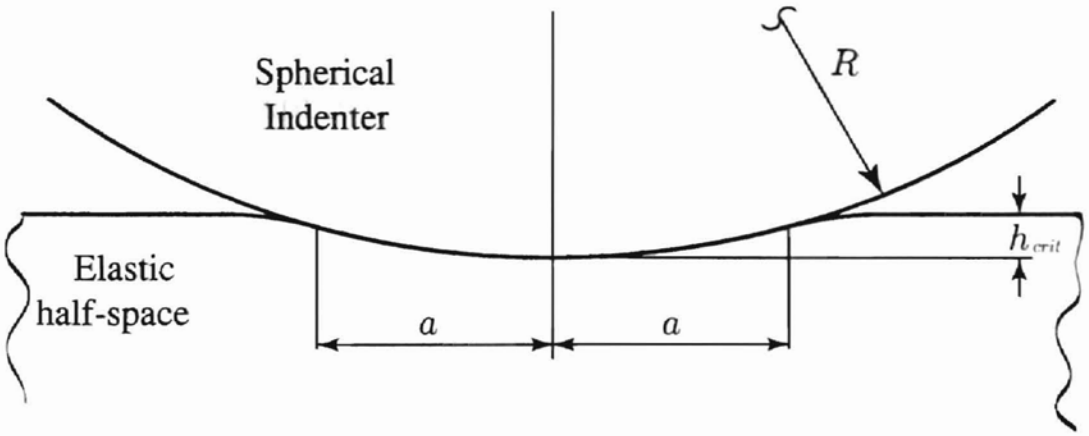

Figure 4-9: Contact between a spherical indenter and an elastic half-space

	$\mathbf{p_0}$	
	GPa	Range %
Zn face	16.9 ± 1.2	± 7.1
O face	17.1 ± 2.0	± 11.7

Table 4.5: Maximum pressure under the indenter at the onset of plasticity for the two polar faces of ZnO

and the radius of contact a can be expressed as [53]

$$a^2 = Rh_{crit} \tag{4.7}$$

We can therefore characterize the onset of plasticity with the maximum pressure under the indenter p_0 which depends on both the critical load and depth, viz.,

$$p_0 = \frac{3}{2}\frac{P_{crit}}{\pi R h_{crit}} \tag{4.8}$$

Table 4.5 lists the onset of pop-in in terms of the maximum pressure. No discernible differences can be seen between the two faces and the variability drops to less than 12%. By considering the critical load and depth separately to characterize the onset of plasticity the difference in the elastic moduli between the two faces was not considered.

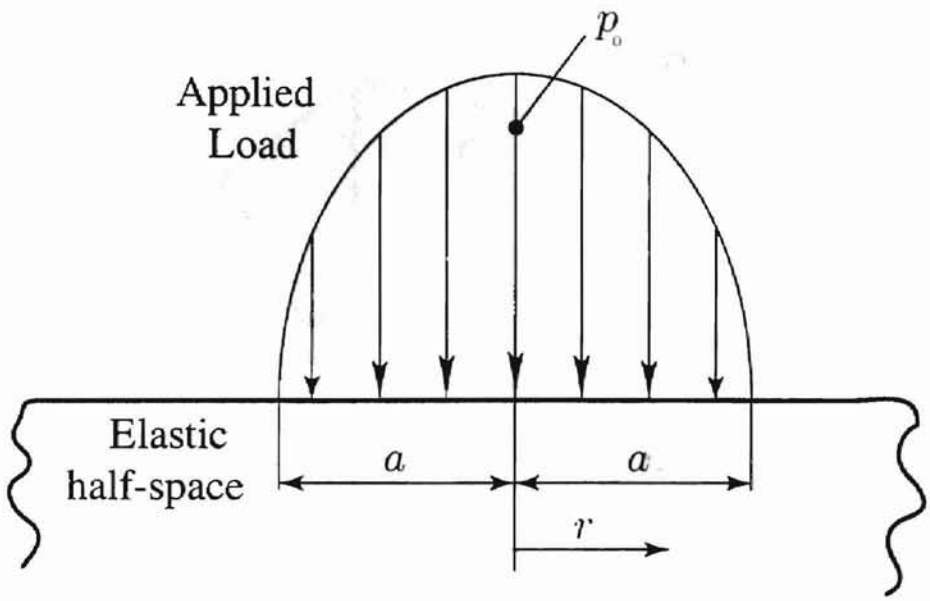

Figure 4-10: Elliptical pressure distribution due to the contact between a spherical indenter and an elastic half-space evaluated by Hertz

This could account for the observed difference in the occurrence of pop-in listed in Table 4.4.

4.4 Investigation of the $(10\bar{1}0)$ and $(11\bar{2}0)$ Prismatic Planes of ZnO

In addition to the study performed on the (0001) and $(000\bar{1})$ polar faces the prismatic planes $(10\bar{1}0)$ and $(11\bar{2}0)$ which are 90° apart were also studied. Shown in Fig. 4-11 is the hexagonal geometry of ZnO and the three principal planes which have been studied. Note that planes 60° apart are members of the same family of planes due to the six-fold symmetry [13]. Study on the $(10\bar{1}0)$ and $(11\bar{2}0)$ planes was necessary to enable an estimate of the theoretical shear strength (and to estimate the active slip systems). This also allowed for the measurement of the hardness and elastic modulus for these planes.

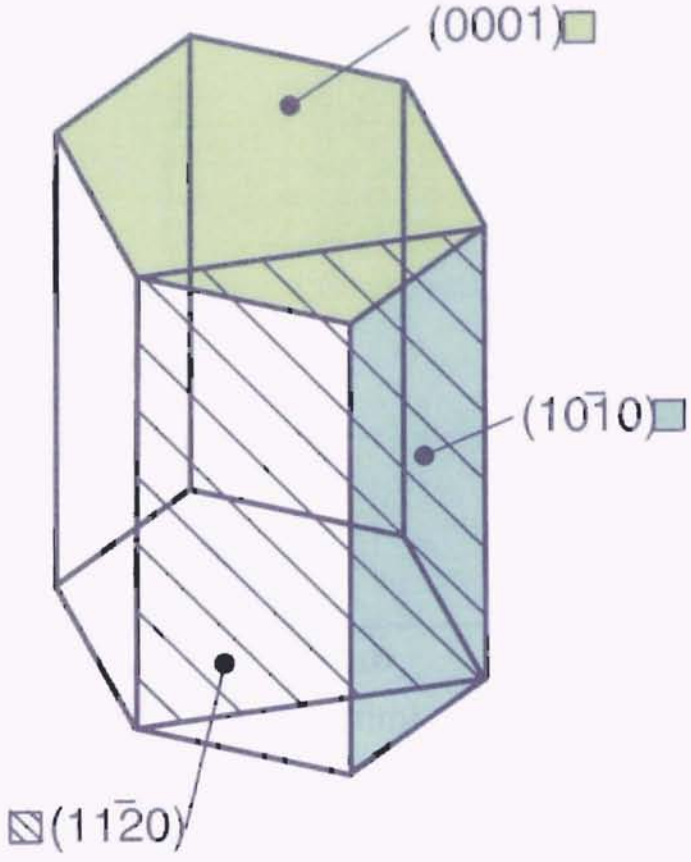

Figure 4-11: Hexagonal geometry showing the planes which have been studied

Both the (10$\bar{1}$0) and (11$\bar{2}$0) faces of ZnO prepared by chemomechanical polishing were investigated. The range of indentations performed on both faces was 500 - 3000 μN, corresponding to a contact depth of 65 - 190 nm. The lower bound of the load range was increased because at 200 μN some indentations did not exhibit the pop-in.

4.4.1 Measured Hardness

Results of hardness as a function of contact depth for the two prismatic planes are shown in 4-12. The results for the O-terminated face (recall that there were no observed differences between the O and Zn faces) are shown for comparison. The error bars again represent one standard deviation of about fifteen experiments per

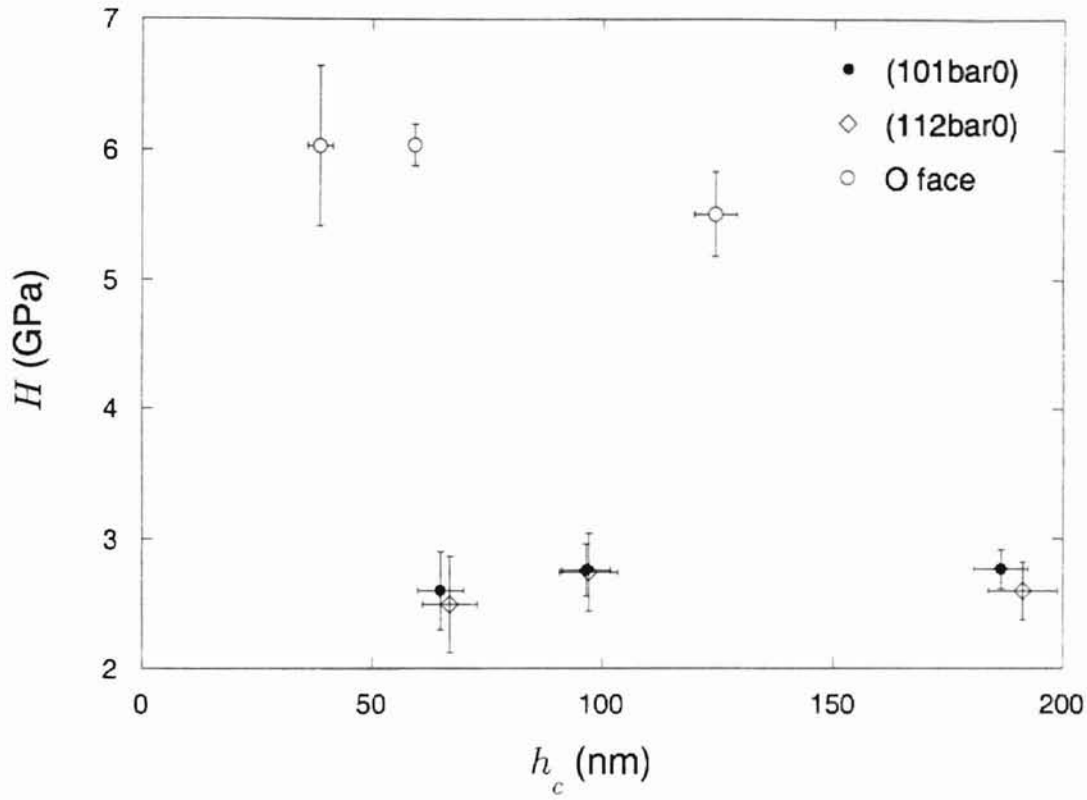

Figure 4-12: Hardness versus contact depth for indentations on the two prismatic planes $(10\bar{1}0)$ and $(11\bar{2}0)$. As a comparison, indentations on the O-terminated face $(000\bar{1})$ are also shown.

point.

The two prismatic faces did not exhibit discernible differences of hardness, but a significant difference between the hardness measured on the prismatic faces and the polar faces was noticed. The hardness for the prismatic faces was found to be 2.7 $\pm$ 0.3 GPa, when averaged over all the indentations performed on both faces. The hardness results for both prismatic faces are summarized in Table 4.6. This value of hardness is seen to be significantly smaller than the 5.3 $\pm$ 0.3 GPa at approximately 125 nm, and 6.2 $\pm$ 0.4 GPa for depths of 18 - 60 nm found for the Zn and O faces.

Typical load-displacement curves obtained for indentation on the $(10\bar{1}0)$, $(11\bar{2}0)$ and $(000\bar{1})$ faces are shown in Fig. 4-13. The lower hardness which results for the

	H (GPa)
Depth	65-190 nm
$(10\bar{1}0)$	2.7 ± 0.2
$(11\bar{2}0)$	2.6 ± 0.3

Table 4.6: Hardness results of the two prismatic faces of ZnO

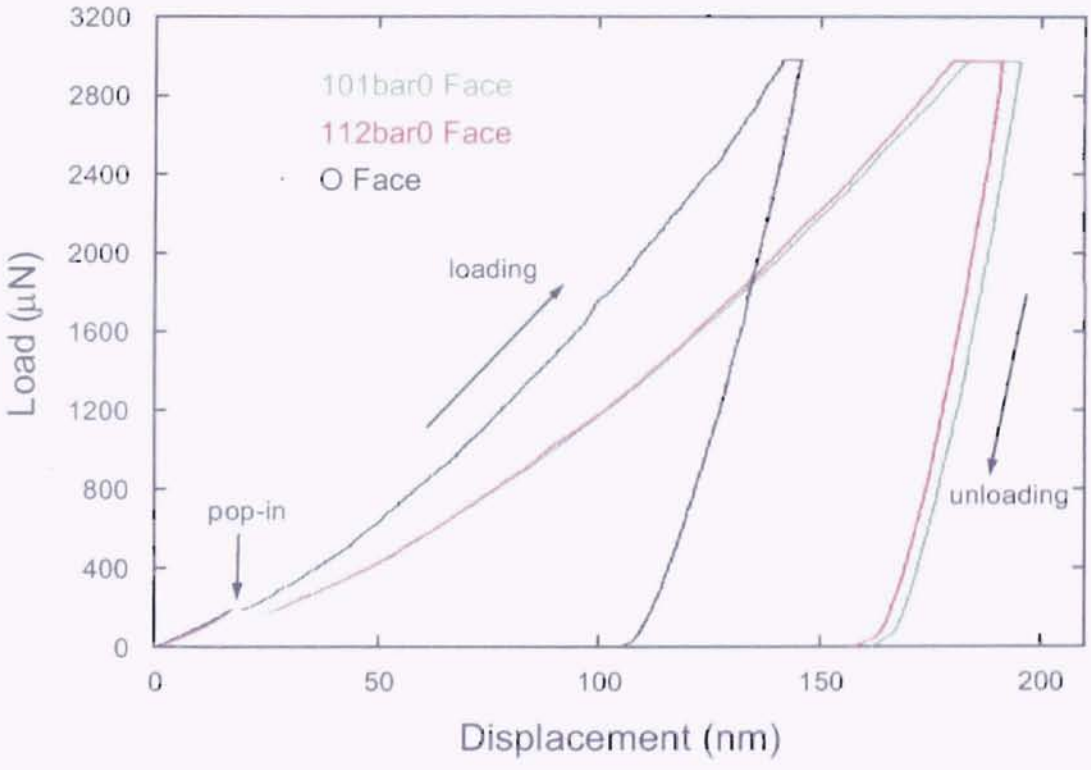

Figure 4-13: Comparison between the O face and the prismatic $(10\bar{1}0)$, $(11\bar{2}0)$ faces

$(10\bar{1}0)$ and $(11\bar{2}0)$ planes can be seen.

4.4.2 Measured Elastic Modulus

Fig. 4-14 shows a comparison of the elastic modulus obtained for both polar faces and

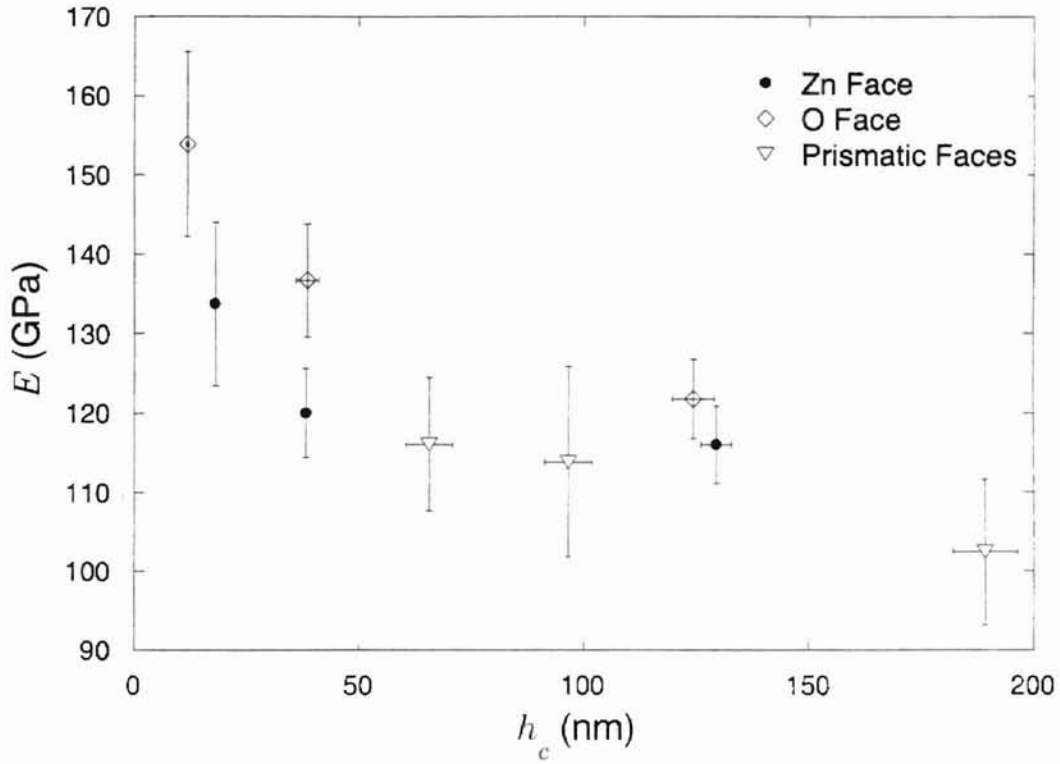

Figure 4-14: Comparison between the elastic modulus obtain for the Zn and O face and the prismatic faces

the prismatic faces. The data for the $(10\bar{1}0)$ and $(11\bar{2}0)$ faces are considered together because they did not present any significant difference in elastic modulus. The error bars are again based on one standard deviation of about fifteen experiments per point. For the prismatic faces at a contact depth between 65 and 100 nm, E=114.4 $\pm$ 11.2 GPa. This value is in agreement with the reported elastic modulus for bulk ZnO, and is the same order of magnitude for that of the polar faces. At a depth of approximately 190 nm the elastic modulus is seen to decrease to E=102.4 $\pm$ 9.3 GPa. The decrease

	E (GPa)				
Depth	18 nm	65-100 nm	125 nm	190 nm	Bulk [18]
Zn face	133.7 ± 10.3		116.0 ± 4.9		
O face	153.9 ± 11.8		121.7 ± 5.0		
Prismatic Faces		114.4 ± 11.2		102.4 ± 9.3	
ZnO					123.0

Table 4.7: Summary of the elastic modulus results for the (0001), (000$\bar{1}$), (10$\bar{1}$0) and (11$\bar{2}$0) faces and for bulk ZnO

of elastic modulus with increased contact depth was also observed for the polar faces. The elastic modulus results are summarized in Table 4.7. At contact depths greater than 65 nm, no significant differences in the elastic moduli measured for all the faces were observed.

4.4.3 Observation of Pop-in

In all the experiments performed, pop-in was observed. For some indentations two pop-in events at different loads were observed as shown in the load-displacement curve of Fig. 4-15. This behavior was only observed on the prismatic faces. The pop-in depth for all the principal planes indented has been reported in Table 4.8, where for the multiple pop-in events (prismatic planes) the pop-in depths had been added together. As can be seen the pop-in depth during indentations on the prismatic planes is more than double and with greater variability when compared to indentations on the basal planes. The critical load for the first pop-in was found to differ for each of the faces, where $P_{crit} = 146 \pm 23$ μN at a depth of 22 ± 6 nm for the (10$\bar{1}$0) face, and $P_{crit} = 181 \pm 37$ μN at a depth of 27 ± 5 nm for (11$\bar{2}$0) face. The maximum load under the indenter p_0 was found to be 13.3 ± 2.8 GPa for (10$\bar{1}$0) face and 12.0 ± 3.2 GPa for (11$\bar{2}$0) face. The variability in measurements on the prismatic faces was found to be higher than on the polar faces, despite the fact that the same procedure was used during the experiments. A slightly higher roughness of the prismatic faces may

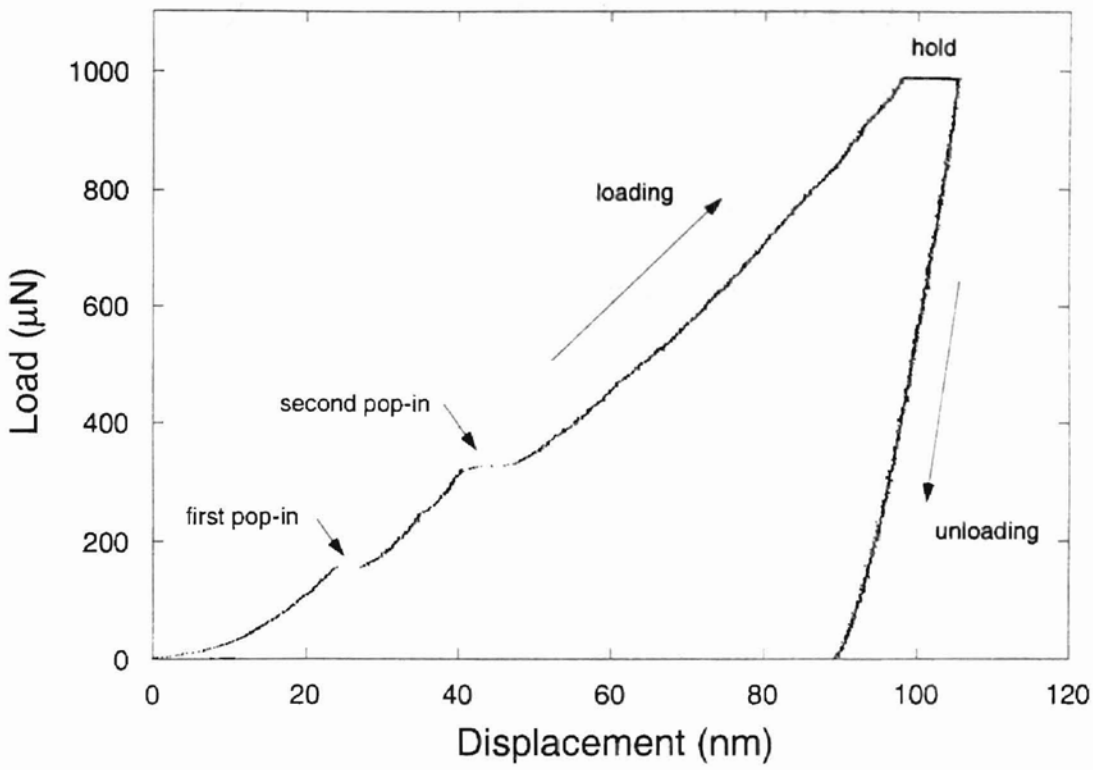

Figure 4-15: Load-displacement curve showing the occurence of 2 pop-in events at different loads. This indentation was made on $(10\bar{1}0)$ face.

account for this (R_{rms} = 0.2 - 0.3 nm for the polar faces vs. R_{rms} = approximately 1.0 nm for the prismatic faces). Table 4.9 summarizes the values obtained for critical load (P_{crit}), depth (h_{crit}) and maximum pressure under the indenter (p_0) for all faces investigated.

	Pop-in Depth (nm)
Zn face	3.31 ± 0.50
O face	2.29 ± 0.60
$(10\bar{1}0)$ face	7.60 ± 2.13
$(11\bar{2}0)$ face	7.56 ± 2.01

Table 4.8: Pop-in depth for all the principal planes indented

	P_{crit} (μN)	h_{crit} (nm)	p_0 (GPa)
Zn face	150 ± 17	16 ± 1	16.9 ± 1.2
O face	166 ± 30	17 ± 3	17.1 ± 2.0
$(10\bar{1}0)$ face	146 ± 23	22 ± 6	13.3 ± 2.8
$(11\bar{2}0)$ face	181 ± 37	27 ± 5	12.0 ± 3.2

Table 4.9: Pop-in results for the principal planes of ZnO

4.5 Critical Resolved Shear Stresses at the Onset of Plasticity

In this section, the results obtained for the conditions at the onset of plasticity will be used to estimate the active slip systems and their critical resolved shear stress at pop-in. ZnO has a wurtzite structure, and as reported by Das [37] in a study on CdS (also with a wurtzite structure) five possible slip systems can be identified: $(0001)[11\bar{2}0]$, $(0001)[10\bar{1}0]$, $(10\bar{1}0)[1\bar{2}10]$, $(1\bar{2}10)[10\bar{1}0]$, and $(10\bar{1}0)[0001]$. For each of these slip systems the maximum resolved shear stress must be evaluated.

The assumptions made during the following calculations are: 1) the indenter is spherical with radius 270 nm, 2) an elliptical load resulting from Hertzian theory is applied on the undeformed surface, 3) the material is perfectly elastic and 4) the material is isotropic. A model which considers the material transversely isotropic, following the work of Dahan [160] is currently under development in our research group and was used to calculate the resolved shear stresses at pop-in due to indentation on the polar faces. A comparison between isotropic and transversely isotropic model results showed a difference of 2% on the basal slip systems and 25% on the prismatic slip systems.

To determine the resolved shear stress on a slip system, the state of stress under the indenter must be calculated. The state of stress on an elastic half-space due to a load perpendicular to the surface can be obtained using the approach of Boussinesq [52][53]. The geometry for this problem is shown in Fig. 4-16. The solution in Cartesian coordinates for a load p is given by the following

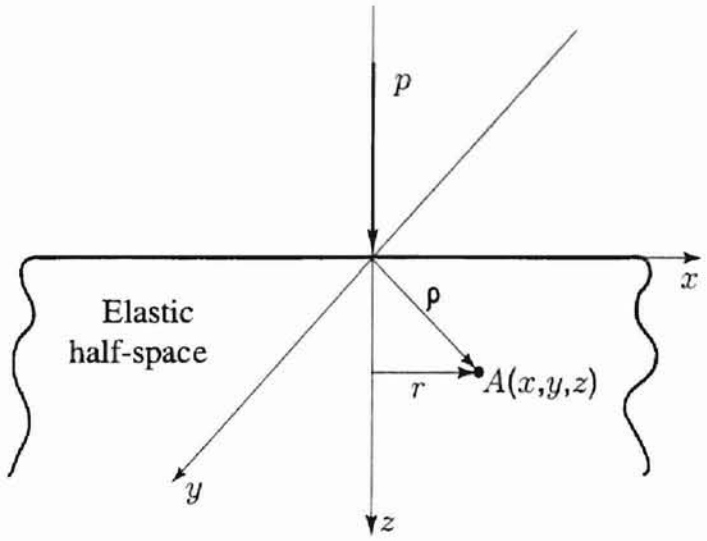

Figure 4-16: Geometry considered in the Boussinesq problem. A(x,y,z) is a ar
point in the elastic half-space.

$$
\begin{aligned}
\sigma^*_{xx} &= \sigma^*_x = \frac{p}{2\pi}\left[\frac{(1-2\nu)}{r^2}\left\{\left(1-\frac{z}{\rho}\right)\frac{x^2-y^2}{r^2}+\frac{zy^2}{\rho^3}\right\}-\frac{3zx^2}{\rho^5}\right] \\
\sigma^*_{yy} &= \sigma^*_y = \frac{p}{2\pi}\left[\frac{(1-2\nu)}{r^2}\left\{\left(1-\frac{z}{\rho}\right)\frac{y^2-x^2}{r^2}+\frac{zx^2}{\rho^3}\right\}-\frac{3zy^2}{\rho^5}\right] \\
\sigma^*_{zz} &= \sigma^*_z = -\frac{3z^3}{2\pi\rho^5}p \\
\sigma^*_{xy} &= \tau^*_{xy} = \frac{p}{2\pi}\left[\frac{(1-2\nu)}{r^2}\left\{\left(1-\frac{z}{\rho}\right)\frac{xy}{r^2}+\frac{xyz}{\rho^3}\right\}-\frac{3xyz}{\rho^5}\right] \\
\sigma^*_{xz} &= \tau^*_{xz} = -\frac{3xz^2}{2\pi\rho^5}p \\
\sigma^*_{yz} &= \tau^*_{yz} = -\frac{3yz^2}{2\pi\rho^5}p
\end{aligned}
$$

where

$$r^2 = x^2 + y^2$$

and

$$\rho^2 = r^2 + z^2 = x^2 + y^2 + z^2$$

In the Hertzian problem the distribution of load on the elastic half-space w

to be elliptical (Fig 4.5). The load applied in Cartesian coordinates is then

$$p(x', y') = p_0 \sqrt{1 - \left[\left(\frac{x'}{a} \right)^2 + \left(\frac{y'}{a} \right)^2 \right]} \tag{4.12}$$

for $-a \leq x' \leq a$ and $-a \leq y' \leq a$, where p_0 is the maximum pressure under the indenter. Thus the components of stress under the indenter can be found by integrating Eqn. (4.9) over the area of contact, a circle of radius a, viz.,

$$\sigma_{ij}(x, y, z) = \int_{-a}^{a} \int_{-\sqrt{a^2-x^2}}^{\sqrt{a^2-x^2}} p(x', y') \, \sigma^*_{ij}(x, y, z) \, dy' dx' \tag{4.13}$$

where the x' and y' indicate the coordinates of the load, and x, y and z indicate the coordinates of an arbitrary point within the elastic half-space. In the present work the integral in Eqn. (4.13) has been evaluated numerically.

Once the state of stress is known the resolved shear stress, τ_r, on any slip plane with normal n and slip direction s can be determined by summing the contribution from all components of stress, σ_{ij}, i.e.,

$$\tau_r = c_{xx}\sigma_{xx} + c_{yy}\sigma_{yy} + c_{zz}\sigma_{zz} + 2c_{xy}\sigma_{xy} + 2c_{xz}\sigma_{xz} + 2c_{yz}\sigma_{yz} \tag{4.14}$$

where c_{ij} are the Schmid factors

$$c_{ij} = \frac{1}{2}(n_i s_j + n_j s_i) \tag{4.15}$$

Consider the following example for determining the Schmid factors for indentation on the $(11\bar{2}0)$ face and for the slip system of $(1\bar{2}10)[10\bar{1}0]$ as shown in Fig 4-17. For this case s is 30° clockwise from the z axis and perpendicular to x, and n is 30° clockwise from the y axis and perpendicular to x. Then.

$$n_x = 0 \; ; \; n_y = \cos 30^\circ = \frac{\sqrt{3}}{2} \; ; \; n_z = -\sin 30^\circ = -\frac{1}{2} \tag{4.16}$$

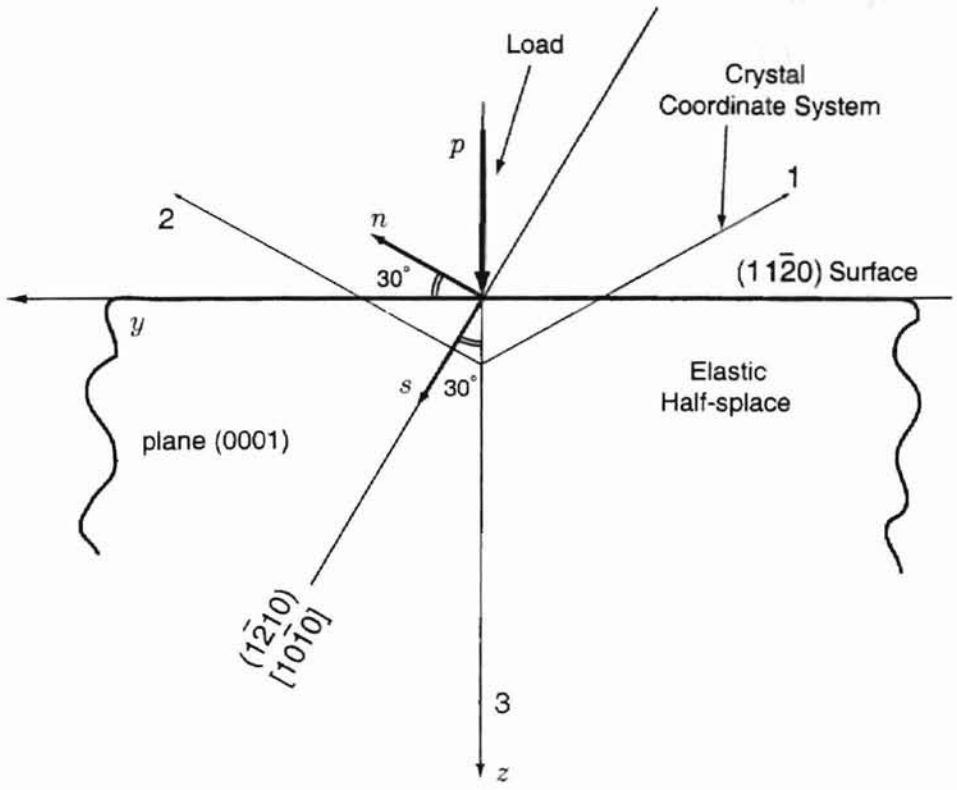

Figure 4-17: Slip plane normal n, and slip direction s for an indentation on the $(11\bar{2}0)$ face and a $(1\bar{2}10)[10\bar{1}0]$ slip system

$$s_x = 0 \; ; \; s_y = \sin 30^\circ = \frac{1}{2} \; ; \; s_z = \cos 30^\circ = \frac{\sqrt{3}}{2}$$

$$\begin{aligned} c_{xx} &= n_x s_x = 0 \\ c_{yy} &= n_y s_y = \frac{\sqrt{3}}{4} \\ c_{zz} &= n_z s_z = -\frac{\sqrt{3}}{4} \\ c_{xy} &= \frac{1}{2}\left(n_x s_y + n_y s_x\right) = 0 \\ c_{xz} &= \frac{1}{2}\left(n_x s_z + n_z s_x\right) = 0 \\ c_{yx} &= \frac{1}{2}\left(n_y s_z + n_z s_y\right) = \frac{1}{4} \end{aligned} \tag{4.17}$$

The resolved shear stresses were obtained using the mean values of p_0 in Table 4.9 as input. In Fig. 4-18, the maximum resolved shear stresses for each face indented

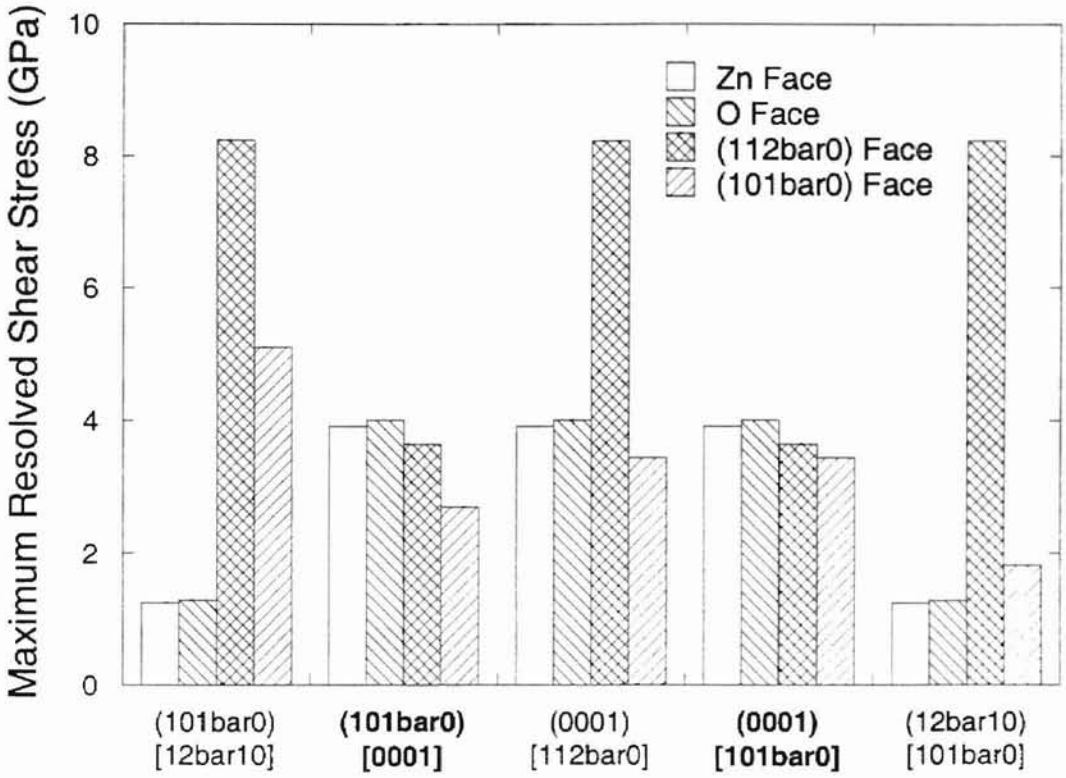

Figure 4-18: Maximum resolved shear stress on the five possible slip systems for indentation on all the faces indented: Zn, O, $(10\bar{1}0)$, and $(11\bar{2}0)$

versus the five most likely slip systems have been shown. How this figure should be analyzed will be explained by considering the $(10\bar{1}0)[1\bar{2}10]$ slip system as an example. For indentations on the Zn face the maximum pressure under the indenter was 16.9 GPa (mean value) which resulted in a maximum resolved shear stress of about 1 GPa on the slip system considered. This value could be, at a maximum, equal to the critical resolved shear stress if this slip system was activated during indentation on the Zn face. What can be observed however is that for indentations on the $(11\bar{2}0)$ face the maximum resolved shear stress was calculated to be approximately 8 GPa. This implies that during indentation on the Zn, O and (1010) faces, where the maximum

resolved shear stress was found to be less the 8 GPa, the $(10\bar{1}0)[1\bar{2}10]$ slip system was not active (since we assume that a given slip system should have only one critical resolved shear stress). In addition the critical resolved shear stress for the $(10\bar{1}0)[1\bar{2}10]$ slip system must be equal to or greater than 8 GPa.

Analyzing the entire Fig. 4-18, it can be seen that for the $(0001)[10\bar{1}0]$ and $(10\bar{1}0)[0001]$ slip systems, for the indentations on all the faces, a constant maximum of about 4 GPa is reached. The indentations on the $(11\bar{2}0)$ face showed that on the $(10\bar{1}0)[1\bar{2}10]$, $(0001)[11\bar{2}0]$, and $(1\bar{2}10)[10\bar{1}0]$ slip systems, a lower bound for the critical resolved shear stress is about 8 GPa. It was then concluded that for indentation on the Zn, O and (1010) faces the active slip system could be either the basal $(0001)[10\bar{1}0]$ or the prismatic $(10\bar{1}0)[0001]$ slip system if not both, with a critical resolved shear stress of approximately 4 GPa.

4.6 Minor Studies

Several minor studies were performed using nanoindentation on ZnO. These studies included: 1) mechanically polished ZnO, 2) etched ZnO and 3) ZnO exposed to UV light. The purpose of these minor studies was to identify fertile areas for future work, and to allow for some basic comparisons to the main study undertaken.

4.6.1 Indentation of Mechanically Polished ZnO

A set of ZnO wafers were prepared by mechanical polishing to enable a comparison with the chemomechanically polished surfaces of the main study. The surfaces were polished with a 1 μm diamond abrasive/de-ionized H_2O slurry. Indentations were performed only on the Zn face. Figure 4-19 shows a comparison of the load-displacement curves obtained for chemomechanically polished and mechanically polished Zn face surfaces. The main differences between the two surfaces are the pop-in and the penetration of the indenter.

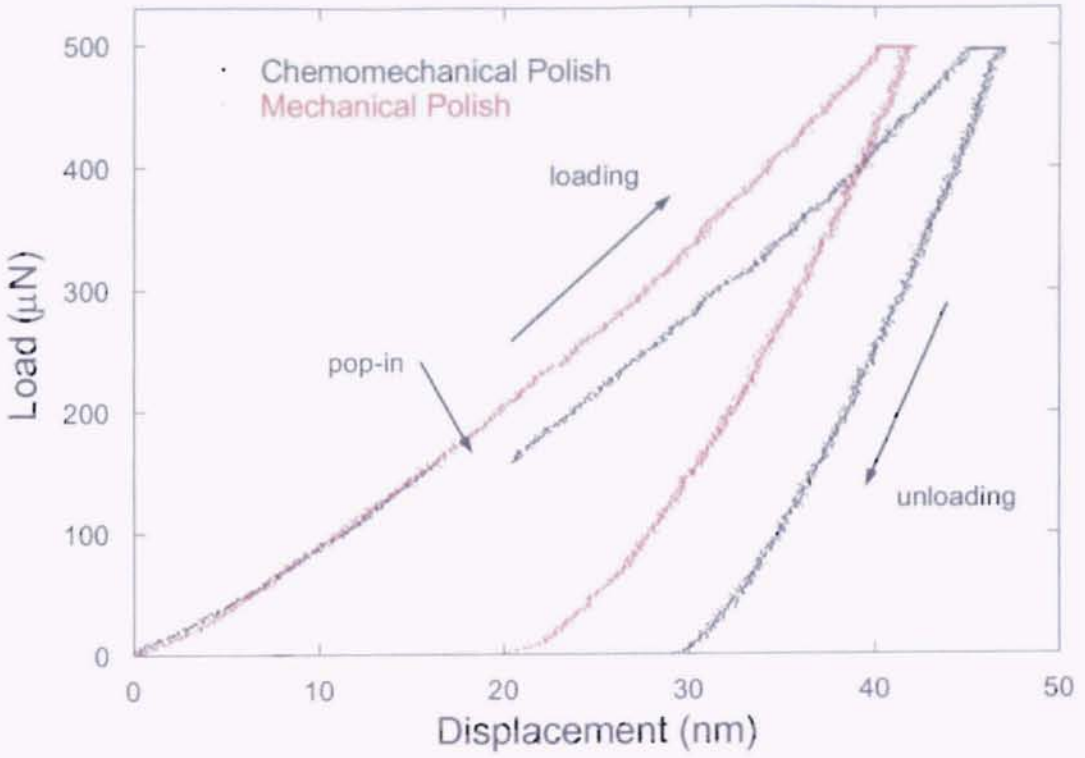

Figure 4-19: Load-displacement curve for a peak load of 500 μN showing the presence of pop-in for a chemomechanically polished surface and the absence of it for a mechanically polished surface.

The fact that pop-in is present for the indentation on the chemomechanically polished surface but not for the mechanically polished surface is in agreement with a recent study conducted by Miyahara on electrolytically and mechanically polished (001) tungsten single crystals [80]. In this study it was found that for the mechanically polished specimen during indentation plastic deformation occurred from the beginning, contrary to the electrolytically polished specimen where deformation was purely elastic until the force reached a critical value, beyond which a sudden increase in depth was observed. In the present study a similar result was found, where the mechanically polished surface exhibited some permanent deformation on unloading while the chemomechanically polished surface behaved purely elastically. This is shown in

Fig. 4-20. Inexplicable is the fact that the two surfaces follow the same loading curve.

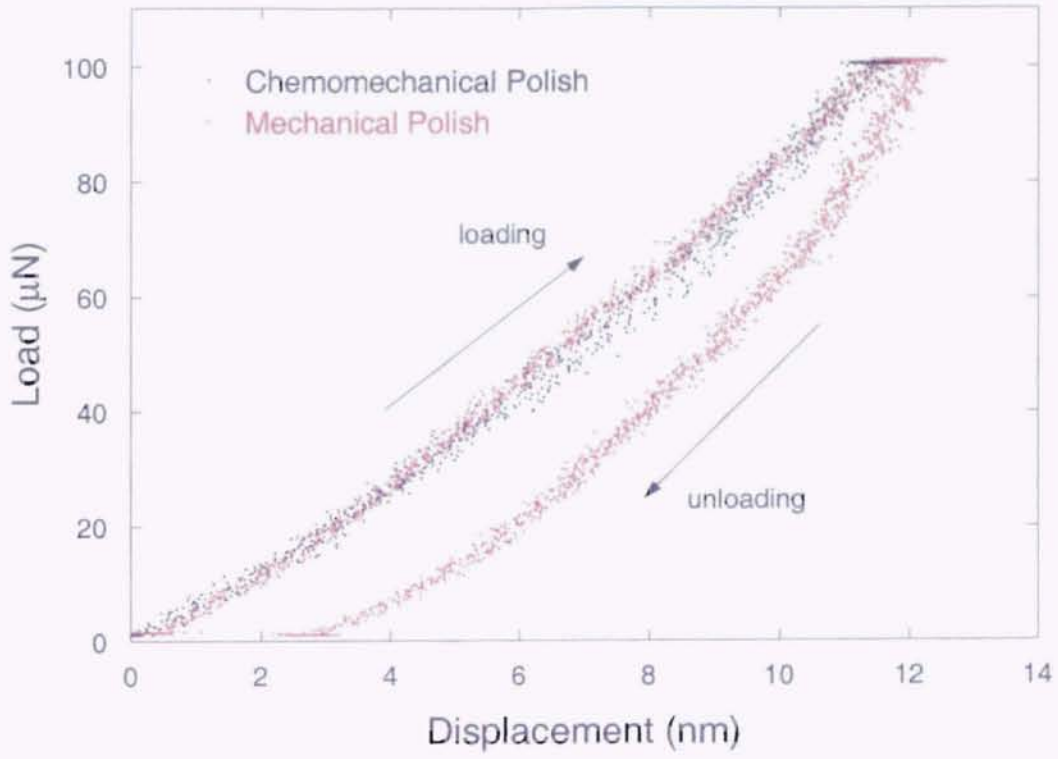

Figure 4-20: Load-displacement curve for a peak load of 100 μN, showing the purely elastic behavior of the chemomechanically polished surface and the elasto-plastic behavior of the mechanically polished surface.

This was not the case for the study conducted by Miyahara. This point needs further study.

As can be seen in Fig. 4-19 the indenter penetrated less into the mechanically polished surface indicating a higher hardness. The hardness for the mechanically polished surface was approximately 7.8 GPa.

4.6.2 Indentation of Etched ZnO

The Zn face was etched using the procedure previously described in Chapter 3, and nanoindentation was performed to obtain a comparison with the chemomechanically

	H (GPa)	E (GPa)
Etched Zn Face	5.6 ± 0.4	120.1 ± 6.2
Chemomechanically polished Zn Face	6.2 ± 0.4	133.7 ± 10.3

	P_{crit} (μN)	h_{crit} (nm)	p_0 (GPa)
Etched Zn Face	126 ± 18	15 ± 1	15.2 ± 1.1
Chemomechanically polished Zn Face	150 ± 17	16 ± 1	16.9 ± 1.2

Table 4.10: Indentation results for etched and chemomechanically polished Zn surfaces

polished surface results. The results obtained from this study are summarized in Table 4.10. These results are for a peak load of 200 μN, corresponding to a depth of 25 nm. Minimal differences in H and E were observed between the etched and polished surfaces.

4.6.3 Indentation of the Zn Face while Exposed to UV Light

In this study a lamp producing UV light at 254 nm was used. The lamp operates on 115 Volts, 60 Hz and 0.16 Amps. The study was divided into two different experiments. In the first experiment indentations were performed under UV light. In the second experiment, the sample was exposed to UV light for 18 hours in a chamber purged with nitrogen before an indentation was performed in darkness. Both studies were limited to the Zn face only.

The first experiment was motivated by the results reported by Carlsson [38] on the influence of light on dislocation mobility in ZnO. Carlsson argued that above band-gap light was able to prohibit dislocation motion on the basal plane by increasing the shear stress needed to move dislocations but that it did not have any influence on dislocation motion on prismatic planes. Recall from an earlier section that the two slip planes predicted are: 1) basal slip system $(0001)[10\bar{1}0]$ and 2) prismatic slip system $(10\bar{1}0)[0001]$. The results obtained for the experiment performed under

	P_{crit} (μN)	h_{crit} (nm)	p_0 (GPa)
Zn face under UV light	178	16	19.7
Zn face in darkness	150 $\pm$ 17	16 $\pm$ 1	16.9 $\pm$ 1.2

Table 4.11: Indentation results performed under UV light and in darkness for a Zn surface

UV light did not exclude either one of the two slip systems as being active. In fact some indentations with loads as high as 500 μN did not exhibit pop-in, but this this was not repeatable in that some did exhibit pop-in. The results in terms of pop-in for those indentations where it occurred are shown in Table 4.11. The standard deviations for these results were not evaluated due to the few indentations performed. During this experiment two main problems were faced. First, the set-up of the lamp under the instrument enclosure did not guarantee that light was properly illuminating the surface. Secondly, there was significant noise introduced on the load-displacement curve as shown in Fig. 4-21, which had a frequency of about 60 Hz which is consistent with that used by the lamp.

The second experiment was characterized by an interesting phenomenon, the growth of "bumps" on the surface as can be seen in Fig. 4-22. With the presence of these bumps it was harder to find a flat region, and this was worst with the increase of time of exposure of the sample to UV light. As a result no further nanoindentation studies on these surfaces were performed. The appearance of these "bumps" requires further study.

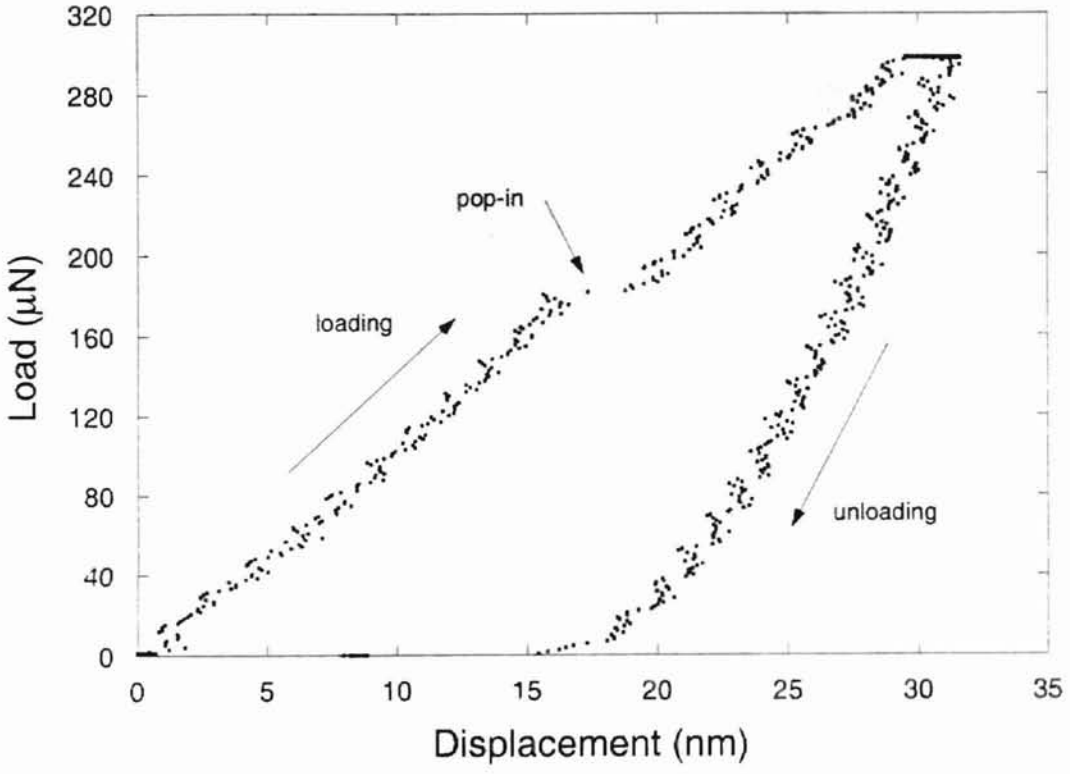

Figure 4-21: Load-displacement curve for an indentation performed under UV light. Note the noise at 60 Hz introduced by the light.

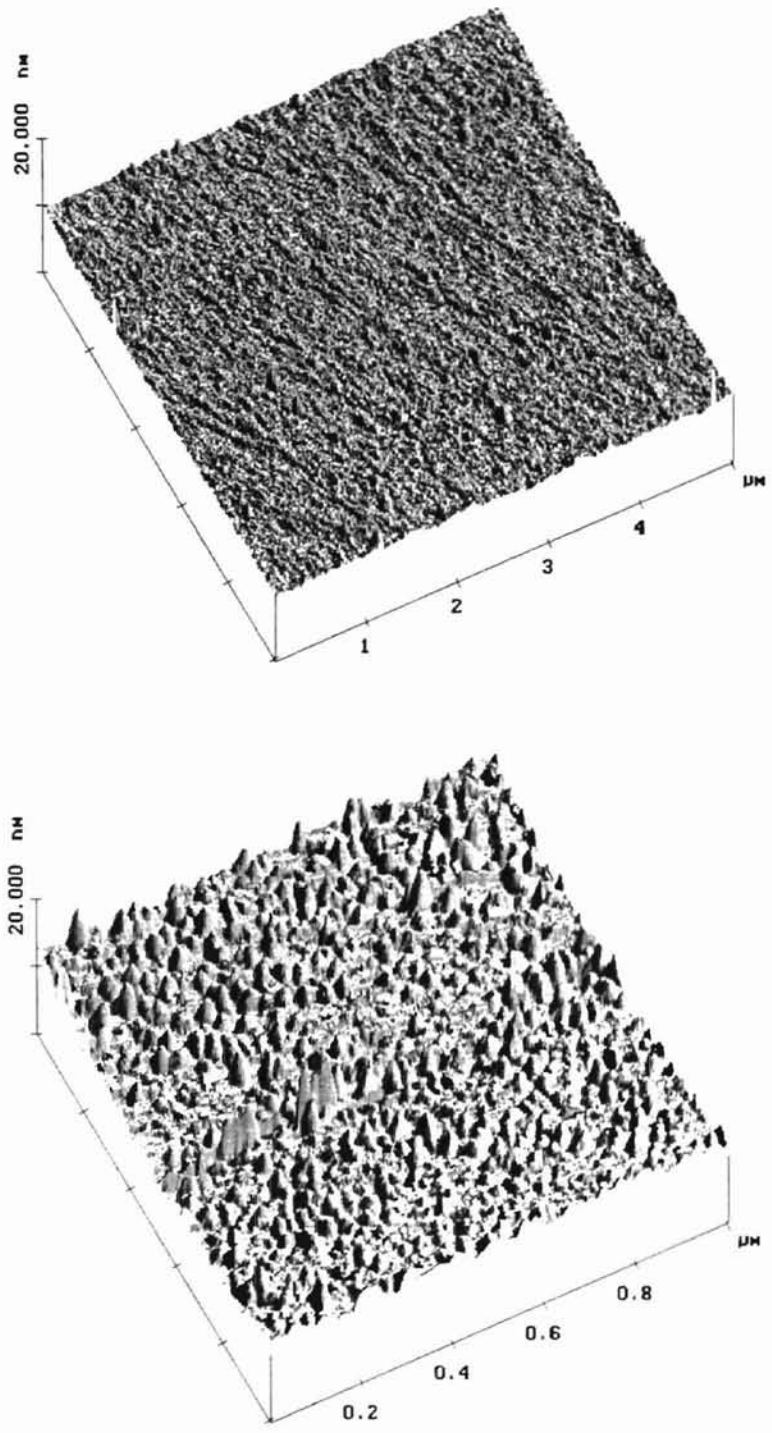

Figure 4-22: Topography of the Zn surface of ZnO before (above) and after (under) the exposure of UV light for 18 hours

Chapter 5

Conclusions

The principal planes of single crystal ZnO prepared by chemomechanical polishing have been investigated by nanoindentation. These included the (0001), (000$\bar{1}$), (10$\bar{1}$0) and (11$\bar{2}$0) planes.

Findings indicate no measurable difference in hardness between the Zn and O face. The measured hardness was found to be 5.3 $\pm$ 0.3 GPa at approximately 125 nm, and 6.2 $\pm$ 0.4 GPa for depths of approximately 18 - 60 nm. A plausible explanation of why no difference between the two faces was observed is that at the depth scale investigated the dislocations generated during the onset of plasticity do not interact with each other. This may be due to only a few dislocations being generated or may be because the dislocations move on only one slip system and therefore are parallel to each other. However, a difference in hardness was found between indentation on the basal faces and indentation on prismatic faces. The measured hardness of the prismatic faces was found to be 2.7 $\pm$ 0.3 GPa, thus the hardness of the prismatic faces is lower than the basal faces.

The elastic modulus for the deepest indentations (h_c=125 nm) performed on both the polar faces did not present discernible differences, 116.0 $\pm$ 4.9 GPa for the Zn face and 121.7 $\pm$ 5.0 GPa for the O face, and measured values were in agreement with the reported bulk elastic modulus of 123.0 GPa. The elastic modulus for shallow

indentations (h_c=18 nm) exhibited a difference between the two faces where for the Zn face E=133.7 ± 10.3 GPa and for the O face E=153.9 ± 11.8 GPa. A plausible explanation regarding the observed difference in elastic modulus between the polar faces at shallow indentation depths could be differences in stoichiometry, bonding or simply the difference in atomic arrangement of the two surfaces as a result of reconstruction and relaxation. No definitive explanation however can be given with the available understanding of the surface compositions.

Chemomechanically polished surfaces exhibited purely elastic behavior until the onset of plasticity at pop-in. Pop-in was attributed to dislocation nucleation and was characterized by the maximum pressure under the indenter (p_0). No measurable difference in p_0 was found between the two polar faces. The onset of pop-in was found to be highly repeatable.

A calculation of the critical resolved shear stress was made based on a prediction of the possibly active slip systems. To determine the critical resolved shear stress the pop-in data for indentations on the polar (0001), (000$\bar{1}$) and prismatic (10$\bar{1}$0), (11$\bar{2}$0) planes were used. Results indicate that the (0001)[10$\bar{1}$0] and/or (10$\bar{1}$0)[0001] systems were responsible for slip at pop-in with a critical resolved shear stress of about 4 GPa. In addition, the indentations on the (11$\bar{2}$0) face showed that on the (10$\bar{1}$0)[1$\bar{2}$10], (0001)[11$\bar{2}$0] and (1$\bar{2}$10)[10$\bar{1}$0] slip systems, the critical resolved shear stress was estimated to have a lower bound of 8 GPa.

Minor studies investigating mechanically polished and etched Zn surfaces, and the influence of UV light on the surface mechanical properties of ZnO have also been performed. Surfaces which had been mechanically polished did not exhibit pop-in and had a higher hardness than those which had been chemomechanically polished. No discernible differences in elastic modulus was found between the mechanically polished and chemomechanically polished surfaces. Due to several experimental difficulties the studies on the influence of UV light were inconclusive.

Bibliography

[1] V. Srikant and D. R. Clarke. On the optical band gap of zinc oxide. *Journal of Applied Physics*, 83(10):5447–5451, 1998.

[2] R. Ahuja, L. Fast, O. Eriksson, J. M. Wills, and B. Johansson. Elastic and high pressure properties of ZnO. *Journal of Applied Physics*, 83:8065–8067, 1998.

[3] X. W. Sun and H. S. Kwok. Optical properties of epitaxially grown zinc oxide films on sapphire by pulsed laser deposition. *Journal of Applied Physics*, 86(1):408–411, 1999.

[4] D. C. Look. Recent advances in ZnO materials and devices. *Materials Science and Engineering B*, 80:383–387, 2001.

[5] S. Choopun, R. D. Vispute, W. Noch, A. Balsamo, R. P. Sharma, T. Venkatesan, A. Iliadis, and D. C. Look. Oxygen pressure-tuned epitaxy and optoelectronic properties of laser-deposited ZnO films on sapphire. *Applied Physics Letters*, 75:3947–3949, 1999.

[6] D. M. Bagnall, Y. F. Chen, Z. Zhu, T. Yao, M. Y. Shen, and T. Goto. High temperature excitonic stimulated emission from ZnO epitaxial layers. *Applied Physics Letters*, 73(8):1038–1040, 1998.

[7] D. M. Bagnall, Y. F. Chen, Z. Zhu, T. Yao, S. Koyama, M. Y. Shen, and T. Goto. Optically pumped lasing of ZnO at room temperature. *Applied Physics Letters*, 70:2230–2232, 1997.

[8] Z. K. Tang, G. K. L. Wong, P. Yu, M. Kawasaki, A. Ohtomo, H. Koinuma, and Y. Segawa. Room-temperature ultraviolet laser emission from self-assembled ZnO microcrystallite thin films. *Applied Physics Letters*, 72:3270–3272, 1998.

[9] S. Chang, N. B. Rex, R. K. Chang, G. Chong, and L. J. Guido. Stimulated emission and lasing in whispering-gallery modes of GaN microdisk cavities. *Applied Physics Letters*, 75:166–168, 1999.

[10] Y. Chen, D. M. Bagnall, H. Koh, K. Park, K. Hiraga, Z. Zhu, and T. Yao. Plasma assisted molecular beam epitaxy of ZnO on c-plane sapphire: Growth and characterization. *Journal of Applied Physics*, 84(7):3912–3918, 1998.

[11] A. Yamamoto, T. Kido, T. Goto, Y. Chen, T. Yao, and A. Kasuya. Dynamics of photoexcited carriers in ZnO epitaxial thin films. *Applied Physics Letters*, 75(4):469–471, 1999.

[12] M. Neuberger. II-VI semiconducting compounds data tables. Technical Report AD 698 341, Electronic Properties Information Center, Hughes Aircraft Company, Culver City, California, October 1969.

[13] V. E. Henrich, H. J. Zeiger, E. I. Solomon, and R. R. Gay. Explanation of the 6-fold LEED patterns from polar (0001) and (0001bar) ZnO surfaces. *Surface Science*, 74:682–683, 1978.

[14] H. Karzel, W. Potzel, M. Kofferlein, W. Schiessl, M. Steiner, U. Hiller, G. M. Kalvius, D. W. Mitchell, T. P. Das, P. Blaha, K. Schwarz, and M. P. Pasternak. Lattice dynamics and hyperfine interactions in ZnO and ZnSe at high external pressures. *Physical Review B*. 53:11425–11438, 1996.

[15] M. D. Drory, J. W. Ager III, T. Suski, I. Grzegory, and S. Porowski. Hardness and fracture toughness of bulk single crystal gallium nitride. *Applied Physics Letters*, 69(26):4044–4046, 1996.

[16] Y. S. Park, C. W. Litton, T. C. Collins, and D. C. Reynolds. Exciton spectrum of ZnO. *Physical Review*, 143:512–519, 1966.

[17] V. F. Petrenko and R. W. Whitworth. Charged dislocations and the plastic deformation of II-VI compounds. *Philosophical Magazine A*, 41(5):681–699, 1980.

[18] G. Simmons and H. Wang. *Single Crystal Elastic Constant and Calculated Aggregate Properties: a Handbook*. The M.I.T. Press, London, 1971.

[19] T. B. Bateman. Elastic moduli of single-crystal zinc oxide. *Journal of Applied Physics*, 33:3309–3312, 1962.

[20] L. B. Kobiakov. Elastic, piezoelectric and dielectric properties of ZnO and CdS single crystals in a wide range of temperatures. *Solid State Communications*, 35:305–310, 1980.

[21] J. E. Jaffe and A. C. Hess. Hartree-fock study of phase changes in ZnO at high pressure. *Physical Review B*, 48:7903–7909, 1993.

[22] A. N. Mariano and R. E. Hanneman. Crystallographic polarity of ZnO crystals. *Journal of Applied Physics*, 34:384–388, 1963.

[23] S. C. Chang and P. Mark. The crystallography of the polar (0001) Zn and (0001bar) O surfaces of zinc oxide. *Surface Science*, 46:293–300, 1974.

[24] M. Galeotti, A. Atrei, U. Bardi, G. Rovida, M. Torrini, E. Zanazzi, A. Santucci, and A. Klimov. Structure of the ZnO(0001) surface studied by x-ray photoelectron diffraction. *Chemical Physics Letters*, 222:349–352, 1994.

[25] T. Ohnishi, A. Ohtomo, M. Kawasaki, K. Takahashi, M. Yoshimoto, and H. Koinuma. Determination of surface polarity of c-axis oriented ZnO films by coaxial impact-collision ion scattering spectroscopy. *Applied Physics Letters*, 72:824–826, 1998.

[26] H. C. Gatos and M. C. Lavine. Etching and inhibition of the (111) surfaces of the III-V intermetallic compounds: InSb. *Journal of Physical and Chemical Solids*, 14:169–174, 1960.

[27] T. Matsuoka, N. Yoshimoto, T. Sasaki, and A. Katsui. Wide-gap semiconductor InGaN and InGaAlN grown by MOVPE. *Journal of Electronic Materials*, 21:157–163, 1992.

[28] D. C. Reynolds and S. J. Czyzak. Dislocations in two types of CdS crystals. *Journal of Applied Physics*, 31:94–98, 1960.

[29] J. L. Weyher, P. D. Brown, J. L. Rouviere, T. Wosinski, A. R. A. Zauner, and I. Grzegory. Recent advances in defect-selective etching of GaN. *Journal of Crystal Growth*, 210:151–156, 2000.

[30] M. J. Suscavage, D. F. JR. Ryder, and P. W. Yip. A study of the surface morphological features of the polar faces of ZnO by atomic force microscopy (AFM) methods and AlN thin films deposited on ZnO polar faces by PLD. *Materials Research Society Symposium Proceedings*, 449:283–288, 1997.

[31] R. E. Sherriff, D. C. Reynolds, D. C. Look, B. Jogai, J. E. Hoelscher, T. C. Collins, G. Cantwell, and W. C. Harsch. Photoluminescence measurements from the two polar faces of ZnO. *Journal of Applied Physics*, 88:3454–3457, 2000.

[32] D. A. Lucca, D. W. Hamby, M. J. Klopfstein, G. Cantwell, C. J. Wetteland, J. R. Tesmer, and M. Nastasi. Effects of polishing on the photoluminescence of single crystal ZnO. *Annals of the CIRP*, 57:397–400, 2001.

[33] D. Kohl, M. Henzler, and G. Heiland. Low temperature sublimation processes from clean cleaved polar surfaces of zinc oxide crystals during first heating. *Surface Science*, 41:403–411, 1974.

[34] G. Heiland and P. Kunstmann. Polar surfaces of zinc oxide crystals. *Surface Science*, 13:72–84, 1969.

[35] Y. A. Osip'yan and I. S. Smirnova. Perfect dislocations in the wurtzite lattice. *Physica Status Solidi*, 30:19–29, 1968.

[36] Y. A. Osipyan and I. S. Smirnova. Partial dislocations in the wurtzite lattice. *Journal of Physics and Chemistry of Solids*, 32:1521–1530, 1971.

[37] N. Das and M. Weinstein. Crystal imperfections in vapor-grown CdS. In D. G. Thomas, editor, *II-VI Semiconducting Compounds International Conference*, pages 147–166. W. A. Benjamin, Inc., 1967.

[38] L. Carlsson. Orientation and temperature dependence of the photoplastic effect in ZnO. *Journal of Applied Physics*, 42:676–680, 1971.

[39] N. Y. Gorid'ko, P. P. Kuz'menko, and N. N. Novikov. The change of mechanical properties of germanium with changing concentration of current carriers. *Soviet Physics - Solid State*, 3(12):2652–2656, 1962.

[40] W. Shockley. Dislocations and edge states in diamond crystal structure. *Physical Review*, 91:228, 1953.

[41] Yu. A. Osip'yan and I. B. Savchenko. Experimental observation of the influence of light on plastic deformation of cadmium sulfide. *ZhETF Pis'ma*, 7:130–134, 1968.

[42] V. F. Petrenko, N. N. Khusnatdinov, and I. Baker. Effect of x radiation on the plastic deformation of II-VI compounds. *Physical Review B*, 53(23):15401–15403. 1996.

[43] V. M. Beilin and Y. K. Vekilov. Influence of the internal photoeffect on the microhardness of Ge and Si. *Soviet Physics - Solid State*, 5(8):2372–2374, 1963.

[44] D. A. Lucca, E. Brinksmeier, and G. Goch. Progress in assessing surface and subsurface integrity. *Annals of the CIRP*, 47:669–693, 1998.

[45] B. Bhushan. Nanomechanical properties of solid surfaces and thin films. In *Handbook of Micro/Nanotribology*, pages 321–396. CRC Press, Inc., 1995.

[46] G.E. Dieter. *Mechanical Metallurgy*. McGraw-Hill, Boston, 1986.

[47] J. L. Loubet, J. M. Georges, O. Marchesini, and G. Meille. Vickers indentation curves of magnesium oxide (MgO). *Journal of Tribology*, 106:43–48, 1984.

[48] M. F. Doerner and W. D. Nix. A method for interpreting the data from depth-sensing indentation instruments. *Journal of Materials Research*, 1:601–609, 1986.

[49] S. V. Hainsworth, H. W. Chandler, and T. F. Page. Analysis of nanoindentation load-displacement loading curves. *Journal of Materials Research*, 11, 1996.

[50] W. C. Oliver and G. M. Pharr. An improved technique for determining hardness and elastic modulus using load and displacement sensing indentation experiments. *Journal of Materials Research*, 7:1564–1583, 1992.

[51] J. Woirgard and J-C. Dargenton. An alternative method for penetration depth determination in nanoindentation measurements. *Materials Research Society*, 12:2455–2458, 1997.

[52] F. F. Ling, W. M. Lai, and D. A. Lucca. *Fundamentals of Surface Mechanics with Applications*. Springer-Verlag, New York, to appear.

[53] K. L. Johnson. *Contact Mechanics*. Cambridge University Press, Cambridge, 1985.

[54] A. E. H. Love. Boussinesq's problem for a rigid cone. *Quarterly Journal of Mathematics (Oxford)*. 10:161–175. 1939.

[55] I. N. Sneddon. The relation between load and penetration in the axisymmetric boussinesq problem for a punch of arbitrary profile. *International Journal of Engineering Science*, 3:47–57, 1965.

[56] D. Tabor. A simple theory of static and dynamic hardness. *Proceedings of the Royal Society A*, page 247, 1948.

[57] N. A. Stillwell and D. Tabor. Elastic recovery of conical indentations. *Proceedings of the Royal Society*, 78:169–179, 1961.

[58] R. B. King. Elastic analysis of some punch problems for a layered medium. *International Journal of Solids Structures*, 23(12):1657–1664, 1987.

[59] J. B. Pethica, R. Hutchings, and W. C. Oliver. Hardness measurement at penetration depths as small as 20 nm. *Philosophical Magazine A*, 48:593–606, 1983.

[60] L. E. Seitzman. Mechanical properties from instrumented indentation: Uncertainties due to tip-shape correction. *Journal of Materials Research*, 13:2936–2944, 1998.

[61] J. Woirgard and J. C. Dargenton. A new proposal for design of high-accuracy nano-indenters. *Measurement Science and Technology*, 6:16–21, 1995.

[62] Y. Sun, S. Zheng, T. Bell, and J. Smith. Indenter tip radius and load frame compliance calibration using nanoindentation loading curves. *Philosophical Magazine Letters*, 79:649–658, 1999.

[63] T. Bao, Jr. P. W. Morrison, and W. Woyczynski. AFM nanoindentation as a method to determine microhardness of hard thin films. *Materials Research Society Symposium Proceedings*, 517:395–400, 1998.

[64] Y. Y. Lim, M. M. Chaudhri, and Y. Enomoto. Accurate determination of the mechanical properties of thin aluminum films deposited on sapphire flats using nanoindentations. *Journal of Materials Research*, 14:2314–2327, 1999.

[65] T. Y. Tsui and G. M. Pharr. Substrate effects on nanoindentation mechanical property measurment of soft films on hard substrates. *Journal of Materials Research*, 14:292–301, 1999.

[66] J. D. Kiely, K. F. Jarausch, J. E. Houston, and P. E. Russell. Initial stages of yield in nanoindentation. *Journal of Materials Research*, 14(6):2219–2227, 1999.

[67] N. Gane and P. Bowden. Microdeformation of solids. *Journal of Applied Physics*, 39:1432–1435, 1968.

[68] T. F. Page, W. C. Oliver, and C. J. McHargue. The deformation behavior of ceramic crystals subjected to very low load (nano)indentations. *Journal of Materials Research*, 7:450–473, 1992.

[69] W. W. Gerberich, J. C. Nelson, E. T. Lilleodden, P. Anderson, and J. T. Wyrobek. Indentation induced dislocation nucleation: The initial yield point. *Acta Materiala*, 44:3585–3598, 1996.

[70] D. F. Bahr, D. E. Kramer, and W. W. Gerberich. Non-linear deformation mechanisms during nanoindentation. *Acta Materiala*, 46:3605–3617, 1998.

[71] D. F. Bahr, D. E. Wilson, and D. A. Crowson. Energy considerations regarding yield points during indentation. *Journal of Materials Research*, 14(6):2269 2275. 1999.

[72] S. Koubaiti, J. J. Couderc, C. Levade, and G. Vanderschaeve. Vickers indentation on the (001) faces of ZnS sphalerite under UV illumination and in darkness.

Crack patterns and rosette microstructure. *Acta Materialia*, 44(8):3279–3291, 1996.

[73] K. Maeda, O. Ueda, Y. Murayama, and K. Sakamoto. Mechanical properties and photomechanical effect in GaP single crystals. *Journal of Physical and Chemical Solids*, 38:1173–1179, 1977.

[74] R. Nowak, M. Pessa, M. Suganuma, M. Leszczynski, I. Grzegory, S. Porowski, and F. Yoshida. Elastic and plastic properties of GaN determined by nano-indentation of bulk crystal. *Applied Physics Letters*, 75:2070–2072, 1999.

[75] R. Nowak, F. Yoshida, J. Morgiel, and B. Major. Postdeposition relaxation of internal stress in sputter-grown thin films caused by ion bombardment. *Journal of Applied Physics*, 85:841–852, 1999.

[76] S. O. Kucheyev, J. E. Bradby, J. S. Williams, C. Jagadish, M. Toth, M. R. Phillips, and M. V. Swain. Nanoindentation of epitaxial GaN films. *Applied Physics Letters*, 77:3373–3375, 2000.

[77] G. Yu, H. Ishikawa, T. Egawa, T. Soga, J. Watanabe, T. Jimbo, and M. Umeno. Mechanical properties of the GaN thin films deposited on sapphire substrate. *Journal of Crystal Growth*, 189/190:701–705, 1998.

[78] I. J. McColm. *Ceramic Hardness*. Plenum Press, New York, 1990.

[79] M. S. Bobji and S. K. Biswas. Deconvolution of hardness from data obtained from nanoindentation of rough surfaces. *Journal of Materials Research*, 14:2259–2268, 1999.

[80] K. Miyahara, S. Matsuoka. and N. Nagashima. Nanoindentation measurement for a tungsten (001) single crystal. *JSME International Journal A*, 41(4):562–568, 1998.

[81] S. G. Roberts. Hardness anisotropy and polarity in indium antimonide. *Philosophical Magazine B*, 53:37–45, 1986.

[82] P. B. Hirsch, P. Pirouz, S. G. Roberts, and P. D. Warren. Indentation plasticity and polarity of hardness on (111) faces of GaAs. *Philosophical Magazine B*, 52(3):759–784, 1985.

[83] X.-J. Ning, N. Huvey, and P. Pirouz. Dislocation cores and hardness polarity of 4H-SiC. *Journal of American Ceramic Society*, 80(7):1645–1652, 1997.

[84] H. Gottschalk, G. Patzer, and H. Alexander. Stacking fault energy and ionicity of cubic III-V compounds. *Physica Status Solidi*, 45:207–217, 1978.

[85] S. Takeuchi, K. Suzuki, K. Maeda, and H. Iwanaga. Stacking-fault energy of II-VI compounds. *Philosophical Magazine A*, 50:171–178, 1984.

[86] A. George and J. Rabier. Dislocations and plasticity in semiconductors. I – dislocation structures and dynamics. *Review of Physics Applications*, 22:941–966, 1987.

[87] J. D. Kiely and J. E. Houston. Nanomechanical properties of Au (111), (001), and (110) surfaces. *Physical Review B*, 57:588–594, 1998.

[88] Y. S. Boyarskaya, D. Z. Grebko, and E. I. Purich. Anomalies in the Knoop microhardness anistropy of crystals. *Journal of Materials Science*, 14:737–741, 1979.

[89] C. A. Brookes, R. P. Burmand, and J. E. Morgan. Anistropy and indentation creep in crystals with the rocksalt structure. *Journal of Materials Science*, 10:2171–2177, 1975.

[90] M. J. Paterson, P. J. K. Paterson, and B. Ben-Nissan. The dependence of structural and mechanical properties on film thickness in sol-gel zirconia films. *Journal of Materials Research*, 13:388–395, 1998.

[91] A. O. Olofinjana, J. M. Bell, and A. K. Jamting. Evaluation of the mechanical properties of sol-gel-deposited titania films using ultra-micro-indentation method. *Wear*, 241:174–179, 2000.

[92] C. M. Chan, G. Z. Cao, H. Fong, M. Sarikaya, T. Robinson, and L. Nelson. Nanoindentation and adhesion of sol-gel-derived hard coatings on polyester. *Journal of Materials Research*, 15:148–154, 2000.

[93] E. Lugscheider, C. Barimani, and M. Lake. Mechanical properties of Ti(C,N) and TiN thin films on cutting tools measured by nanoindentation. *Materials Research Society Symposium Proceedings*, 522:311–316, 1998.

[94] Y. Shima, H. Hasuyama, T. Kondoh, Y. Imaoka, T. Watari, K. Baba, and R. Hatada. Mechanical properties of silicon oxynitride thin films prepared by low energy ion beam assisted deposition. *Nuclear Instruments and Methods in Physics Research B*, 148:599–603, 1999.

[95] O. R. Shojaei and A. Karimi. Comparison of mechanical properties of TiN thin films using nanoindentation and bulge test. *Thin Solid Films*, 332:202–208, 1998.

[96] P. Torri, J.-P. Hirvonen, H. Kung, Y.-C. Lu, M. Nastasi, and P. N. Gibson. Mechanical properties, stress evolution and high-temeprature thermal stability of nanolayered Mo-Si-N/SiC thin films. *Journal of Vacuum Science Technology B*, 17:1329–1335, 1999.

[97] L. Karlsson, L. Hultman, M. P. Johansson, J.-E. Sundgren, and H. Ljungcrantz. Growth, microstructure, and mechanical properties of arc evaporated TiC_xN_{1-x} (0<=x<=1) films. *Surface and Coatings Technology*, 126:1–14, 2000.

[98] L. Karlsson, L. Hultman, and J.-E. Sundgren. Influence of residual stresses on the mechanical properties of TiC_xN_{1-x} (x=0, 0.15, 0.45) thin films deposited by arc evaporation. *Thin Solid Films*, 371:167–177, 2000.

[99] E. Kusano, M. Kitagawa, H. Nanto, and A. Kinbara. Hardness enhancement by compositionally modulated structure of Ti/TiN multilayer films. *Journal of Vacuum Sicence Technology A*, 16:1272–1276, 1998.

[100] H. Buckle. *Science of Hardness Testing and Its Research Applications.* American Society for Metals, Metals Park, 1971.

[101] M. T. Kim. Influence of substrates on the elastic reaction of films for the microindentation tests. *Thin Solid Films*, 283:12–16, 1996.

[102] E. H. Yoffe. The elastic compliance of a surface film on a substrate. *Philosophical Magazine Letters*, 77:69–77, 1998.

[103] X. Cai and H. Bangert. Hardness measurements of thin films - determining the critical ratio of depth to thickness using FEM. *Thin Solid Films*, 264:59–71, 1995.

[104] J. Li, E. T. Thostenson, T. Chou, and L. Riester. An investigation of thin-film coating/substrate systems by nanoindentation. *Journal of Engineering Materials and Technology*, 120:154–162, 1998.

[105] D. B. Marshall and A. G. Evans. Measurement of adherence of residually stressed thin films by indentation. I. mechanics of interface delamination. *Journal of Applied Physics*, 56(10):2632–2638, 1984.

[106] A. G. Evans and J. W. Hutchinson. On the mechanics of delamination and spalling in compressed films. *International Journal of Solids Structures*, 20(5):455–466, 1984.

[107] J.W. Hutchinson and Z. Suo. *Mixed mode cracking in layered materials.* Advances in Applied Mechanics. Academic Press, New York, 1992.

[108] M. D. Kriese, D. A. Boismier, N. R. Moody, and W. W. Gerberich. Nanomechanical fracture-testing of thin films. *Engineering Fracture Mechanics*, 61:1–20, 1998.

[109] M. D. Kriese, W. W. Gerberich, and N. R. Moody. Quantitative adhesion measures of multilayer films: Part I. indentation mechanics. *Journal of Materials Research*, 14:3007–3018, 1999.

[110] N. R. Moody, R. Q. Hwang, S. Venka-Taraman, J. E. Angelo, D. P. Norwood, and W. W. Gerberich. Adhesion and fracture of tantalum nitride films. *Acta Materialia*, 46(2):585–597, 1998.

[111] N. R. Moody, A. Strojny, D. L. Medlin, A. Talin, and W. W. Gerberich. Substrate composition effects on the interfacial fracture of tantalum nitride films. *Journal of Materials Research*, 14:2306–2313, 1999.

[112] N. R. Moody, D. Medlin, D. Boehme, and D. P. Norwood. Film thickness effects on the fracture of tantalum nitride on aluminum nitride thin film systems. *Engineering Fracture Mechanics*, 61:107–118, 1998.

[113] A. Kuper, R. Clissold, P. J. Martin, and M. V. Swain. A comparative assessment of three approaches for ranking the adhesion of TiN coatings onto two steels. *Thin Solid Films*, 308-309:329–333, 1997.

[114] T. Y. Tsui, W. C. Oliver, and G. M. Pharr. Influences of stress on the measurement of mechanical properties using nanoindentation: Part I. experimental studies in an aluminum alloy. *Journal of Materials Research*, 11:752–759, 1996.

[115] K. F. Jarausch, J. D. Kiely, J. E. Houston, and P. E. Russell. Defect-dependent elasticity: Nanoindentation as a probe of stress state. *Journal of Materials Reserach*, 15:1693–1701, 2000.

[116] F. Dahmani, J. C. Lambropoulos, A. W. Schmid, S. J. Burns, and C. Pratt. Nanoindentation technique for measuring residual stress field around a laser-induced crack in fused silica. *Journal of Materials Science*, 33:4677–4685, 1998.

[117] A. V. Zagrebelny and C. B. Carter. Indentation of strained silicate-glass films on alumina substrates. *Scripta Materialia*, 37:1869–1875, 1997.

[118] B. R. Lawn and T. R. Wilshaw. *Fracture of brittle solids.* Cambridge Solid State Science Series. Cambridge University Press, Cambridge, 1975.

[119] G. Y. Odo, L. N. Nogueira, and C. M. Lepienski. Ionic migration effects on the mechanical properties of glass surfaces. *Journal of Non-Crystalline Solids*, 247:232–236, 1999.

[120] S. Suresh and A. E. Giannakopoulos. A new method for estimating residual stresses by instrumented sharp indentation. *Acta Mater.*, 46:5755–5767, 1998.

[121] J.R.M. Radok. Visco-elastic stress analysis. *Quarterly Applied Mathematics*, 15:198–202, 1957.

[122] L. Cheng, L. E. Scriven, and W. W. Gerberich. Viscoelastic analysis of micro- and nanoindentation. *Materials Research Society Symposium Proceedings*. 522:193–198, 1998.

[123] A. Strojny and W. W. Gerberich. Experimental analysis of viscoelastic behavior in nanoindentation. *Materials Research Society Symposium Proceedings*, 522:159–164, 1998.

[124] K. B. Yoder, S. Ahuja, K. T. Dihn. D. A. Crowson, S. G. Corcoran, L. Cheng, and W. W. Gerberich. Nanoindentation of viscolastic materials: Mechanical properties of polymer coatings on aluminum substrates. *Materials Research Society Symposium Proceedings*, 522:205–210. 1998.

[125] A. Flores and F. J. Balta Calleja. Mechanical properties of poly(ethylene terephthalate) at the near surface from depth-sensing experiments. *Philosophical Magazine A*, 78:1283–1297, 1998.

[126] X. Li, D. Diao, and B. Bhushan. Fracture mechanisms of thin amorpyous carbon films in nanoindentation. *Acta Materialia*, 45(11):4453–4461, 1997.

[127] X. Li and B. Bhushan. Evaluation of fracture toughness of ultra-thin amorphous carbon coatings deposited by different deposition techniques. *Thin Solid Films*, 355-356:330–336, 1999.

[128] J. Ding, Y. Meng, and S. Wen. Mechanical properties and fracture toughness of multilayer hard coatings using nanoindentation. *Thin Solid Films*, 371:178–182, 2000.

[129] T. W. Scharf, H. Deng, and J. A. Barnard. Mechanical and fracture toughness studies of amorphous SiC-N hard coatings using nanoindentation. *American Vacuum Society*, 15(3):963–967, 1997.

[130] J. M. Sanchez, S. El-Mansy, B. Sun, T. Scherban, N. Fang, D. Pantuso, W. Ford, M. R. Elizalde, J. M. Martinez-Esnaola, A. Martin-Meizoso, J. Gil-Sevillano, M. Fuentes, and J. Maiz. Cross-sectional nanoindentation: A new technique for thin film interfacial adhesion characterization. *Acta Materialia*, 47(17):4405–4413, 1999.

[131] S. A. S. Asif, K. J. Wahl, and R. J. Colton. The influence of oxide and adsorbates on the nanomechanical response of silicon surfaces. *Journal of Materials Research*, 15(2):546–553, 2000.

[132] S. G. Corcoran and R. J. Colton. Anomalous plastic deformation at surfaces: Nanoindentation of gold single crystals. *Physical Review B*, 55:R16057–R16060, 1997.

[133] A. Gouldstone, H.-J. Koh, K.-Y. Zeng, A. E. Giannakopoulos, and S. Suresh. Discrete and continuous deformation during nanoindentation of thin films. *Acta Materialia*, 48:2277–2295, 2000.

[134] J. E. Bradby, J. S. Williams, J Wong-Leung, M. V. Swain, and P. Munroe. Mechanical deformation of InP and GaAs by spherical indentation. *Applied Physics Letters*, 78(21):3235–3237, 2001.

[135] J. Woirgard, C. Tromas, J. C. Girard, and V. Audurier. Study of the mechanical properties of ceramic materials by the nanoindentation technique. *Journal of European Ceramic Society*, 18(15):2297–3005, 1998.

[136] C. Tromas, J. Colin, C. Coupeau, J. C. Girard, J. Woirgard, and J. Grilhe. Pop-in phenomenon during nanoindentation in MgO. *The European Physical Journal*, 8:123–128, 1999.

[137] C. Tromas, J. C. Girard, V. Audurier, and J. Woirgard. Study of the low stress plasticity in single-crystal MgO by nanoindentation and atomic force microscopy. *Journal of Materials Science*, 34:5337–5342, 1999.

[138] M. Oden, H. Ljungcrantz, and L. Hultman. Characterization of the induced plastic zone in a single crystal TiN(001) film by nanoindentation and transmission electron microscopy. *Journal of Materials Research*, 12:2134–2142, 1997.

[139] D. Caceres, I. Vergara, R. Gonzalez, E. Monroy, F. Calle, E. Munoz, and F. Omnes. Nanoindentation on AlGaN thin films. *Journal of Applied Physics*, 86(12):6773–6778, 1999.

[140] S. P. Timoshenko and J.N. Goodier. *Theory of Elasticity*. McGraw-Hill, Kogakusha, 1970.

[141] S. Kalpakjian. *Manufacturing Processes for Engineering Materials*. Addison-Wesley, Sydney, 1997.

[142] A. Kelly. *Strong Solids.* Clarendon Press Oxford, London, 1966.

[143] F.R.N. Nabarro. Fifty-year study of the Peierls-Nabarro stress. *Materials Science and Engineering*, A234-236:67–76, 1997.

[144] W. W. Gerberich, S. K. Venkataraman, H. Huang, S. E. Harvey, and D. L. Kohlstedt. The injection of plasticity by millinewton contacts. *Acta Metall. Materiala*, 43:1569–1576, 1995.

[145] J. S. Williams, Y. Chen, J. Wong-Leung, A. Kerr, and M. V. Swain. Ultra-micro-indentation of silicon and compound semiconductors with spherical indenters. *Journal of Materials Research*, 14(6):2338–2343, 1999.

[146] E. R. Weppelmann, J. S. Field, and M. V. Swain. Observation, analysis, and simulation of the hysterisis of silicon using ultra-micro-indentation with spherical indenters. *Journal of Materials Research*, 8(4):830–840, 1993.

[147] R. Nowak and M. Sakai. Energy principle of indentation contact: The application to sapphire. *Journal of Materials Research*, 8(5):1068–1078, 1993.

[148] R. Nowak, T. Sekino, S. Maruno, and K. Niihara. Deformation of sapphire induced by a spherical indentation on the (1010) plane. *Applied Physics Letters*, 68:1063–1065, 1996.

[149] D. E. Kramer, L.-C. Chen, C. J. Palmstrom, and W. W. Gerberich. Substrate effects on yield point phenomena in epitaxial thin films. *Materials Research Society Symposium Proceedings*, 522:89–94, 1998.

[150] A.B. Mann and J.B. Pethica. The role of atomic size asperities in the mechanical deformation of nanocontacts. *Applied Physics Letters*, 69:907–909, 1996.

[151] A. B. Mann and J. B. Pethica. The effect of tip momentum on the contact stiffness and yielding during nanoindentation testing. *Philosophical Magazine A*. 79:577–592, 1999.

[152] A. Nadai and A. M. Wahl. *Plasticity.* McGraw-Hill, New York, 1931.

[153] S. G. Roberts, P. Pirouz, and P. B. Hirsch. Doping effects on indentation plasticity and fracture of germanium. *Journal of Materials Science*, 20:1739–1747, 1985.

[154] S. G. Roberts, P. D. Warren, and P. B. Hirsch. Knoop hardness anisotropy on (001) faces of germanium and gallium arsenide. *Journal of Materials Research*, 1(1):162–176, 1986.

[155] J. Doerschel. Transmission electron microscope investigation of indentation induced dislocation configurations on the (001) GaSb face. *Zeitschrift fur Kristallographie*, 209:210–215, 1994.

[156] H. Harada and K. Sumino. Indentation rosettes and dislocation locking by oxygen in silicon. *Journal of Applied Physics*, 53:4838–4842, 1982.

[157] R. Nowak, T. Sekino, and K. Nihara. Surface deformation of sapphire crystal. *Philosophical Magazine A*, 74:171–194, 1996.

[158] E. B. Tadmor, R. Miller, R. Phillips, and M. Ortiz. Nanoindentation and incipient plasticity. *Journal of Materials Research*, 14:2233–2250, 1999.

[159] M. Nyberg, M. A. Nygren, G. M. Pettersson, D. H. Gay, and A. L. Rohl. Hydrogen dissociation on reconstructed ZnO surfaces. *Journal of Physical Chemistry*, 100:9054–9063, 1996.

[160] M. Dahan and J. Zarka. Elastic contact between a sphere and a semi infinite transversely isotropic body. *International Journal of Solids Structures*, 13:229–238, 1977.

Appendix A

Calibration

A calibration is needed to evaluate the machine compliance and the area function of the indenter. The machine compliance (C_f) is needed to evaluate the machine displacement. The displacement of the indenter, one of the outputs of the indentation test, is the sum of the penetration of the tip into the sample surface and the displacement of the machine itself. This machine displacement can be a combination of several displacements due, for example, to the sample holder, the tip holder, the frame of the machine, etc.. The machine-sample system can be modeled as two springs in series, with stiffness S for the sample and K_f=1/C_f for the machine, as shown in Fig. A-1, where

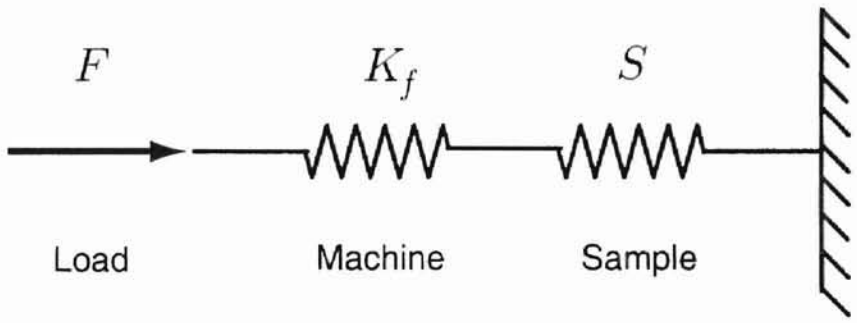

Figure A-1: Simple model of the machine and sample stiffness

$$\frac{1}{K_{tot}} = \frac{1}{K_f} + \frac{1}{S} \tag{A.1}$$

or in terms of the compliance

$$C_{tot} = C_f + C_s \tag{A.2}$$

The area function discussed in Chapter 2 is also obtained by calibration.

The calibration used in this study was described by Oliver and Pharr [50]. The material of the sample used during the calibration was fused silica for which its elastic modulus is well known to be 72 GPa and Poisson's ratio ν=0.170 [50]. Using Eqn. (2.3) the reduced modulus is then 69.6 GPa, where E_i=1141 GPa and ν_i=0.07 for the diamond indenter [50]. This value was checked at the end of the calibration. The method of Oliver and Pharr is an iterative one that does not require the knowledge of the elastic modulus of the sample.

The calibration was divided into two regions, one for high load 1000 - 10000 μN (corresponding to contact depths of 47 - 180 nm), and one for low load 50 - 1000 μN (4.8 - 47nm). Two area functions were determined and the machine compliance for the high load region, where it is more significant, evaluated.

The calibration steps for the high load region were as follows:

1. Nanoindentations were performed at 1000 μN intervals, beginning with 1000 μN and ending at 10000 μN where at each load the indentation was repeated three times.

2. For each indentation the Hysitron software plots the load-displacement curve considering the C_f that was input (in the calibration procedure C_f is set to zero). From the load-displacement curve, the region representing 20 - 95% of the unloading curve was fit to the power law relation Eqn. (2.1)

$$P = \alpha h^m \tag{A.3}$$

where

$$h = h_{\max} - h_f \tag{A.4}$$

This fit was made automatically by the Hysitron software which yields the following: α (μN/nm^m), $h_{\max}$ (nm), h_f (nm), m, $P_{\max}$ the maximum load in μN and h_c the contact depth in nm evaluated as:

$$h_c = h_{\max} - \varepsilon \frac{P_{\max}}{S} \tag{A.5}$$

where S is the contact stiffness evaluated as the slope of a linear line tangent to the unloading curve at the peak load, and ε which depends on the geometry of the indenter and was considered to be 0.75 [50]. All these values were recorded for each indentation.

3. The total compliance C_{tot} was determined by derivation of the power law:

$$C_{tot} = \frac{dh}{dP} = \frac{1}{\alpha m h^{m-1}} = \frac{1}{\alpha m \left(h_{\max} - h_f\right)^{m-1}} \tag{A.6}$$

4. The contact area was calculated with the standard area function:

$$A = 24.5h_c^2 + C_1 h_c + C_2 h_c^{1/2} + C_3 h_c^{1/4} + C_4 h_c^{1/8} + C_5 h_c^{1/16} \tag{A.7}$$

where the constant 24.5 is obtained geometrically considering an ideal Berkovich indenter, and C_1, C_2, C_3, C_4, C_5 result from step 9 (as an approximation for the first calculation of A: C_1=C_2=C_3=C_4=C_5=0).

5. From Eqn. (2.2) in Chapter 2

$$S = \frac{dP}{dh} = \frac{2}{\sqrt{\pi}} E_r \sqrt{A} \tag{A.8}$$

and Eqns. (A.1), (A.2)

$$\frac{1}{S} = C_{tot} - C_f \tag{A.9}$$

it was possible obtain:

$$C_{tot} = \left(\frac{\sqrt{\pi}}{2E_r}\right)\frac{1}{\sqrt{A}} + C_f \tag{A.10}$$

This equation can be seen to be a linear equation of the form:

$$y = mx + q \tag{A.11}$$

where y=C_{tot} and x=$1/\sqrt{A}$ were known from the steps 3 and 4. Plotting the value of y and x for each indentation and fitting a linear equation for all these points the value of m and q and respectively E_r and C_f were obtained. This is shown in Fig. A-2.

6. Knowing C_{tot} and C_f a new value for S could be obtained, not by the slope of the unloading curve, but using the previous equation:

$$S = \frac{1}{C_{tot} - C_f} \tag{A.12}$$

7. Then a new value for h_c was obtained with Eqn. (A.5).

8. As well, a new value for the contact area was evaluated by using Eqn. (2.2):

$$A = \frac{\pi}{4}\frac{1}{(E_r S)^2} \tag{A.13}$$

9. The value of h_c and A were then plotted as shown in Fig. A-3, and fitted by an equation of the kind described in step 4:

$$A = 24.5h_c^2 + C_1 h_c + C_2 h_c^{1/2} + C_3 h_c^{1/4} + C_4 h_c^{1/8} + C_5 h_c^{1/16} \tag{A.14}$$

so that the coefficients C_1, C_2, C_3, C_4, C_5 were determined.

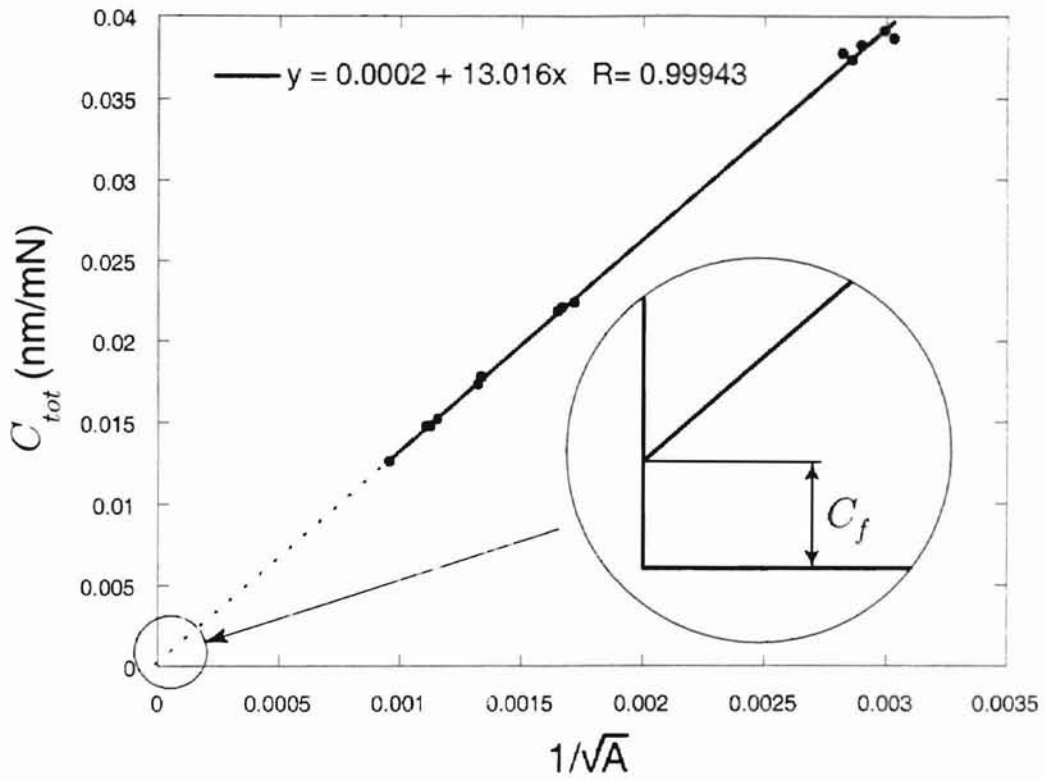

Figure A-2: C_{tot} vs. $1/\sqrt{A}$. From this plot C_f is obtained as the intersection of the linear fit with the y axis and E_r is obtained from the slope of the linear fit.

10. Then, the calculations are repeated from step 4 until C_f converged.

For the calibration of the instrument this cycle was repeated six times before the value of C_f converged to 0.2 nm/μN, E_r converged to 68.1 GPa and the five constants for the high load region, h_c = 47 - 180 nm are

$$
\begin{aligned}
C_1 &= 2.492 \times 10^3 \\
C_2 &= -2.0184 \times 10^5 \\
C_3 &= 2.1705 \times 10^6 \\
C_4 &= -4.7414 \times 10^6 \\
C_5 &= 2.6037 \times 10^6
\end{aligned}
$$

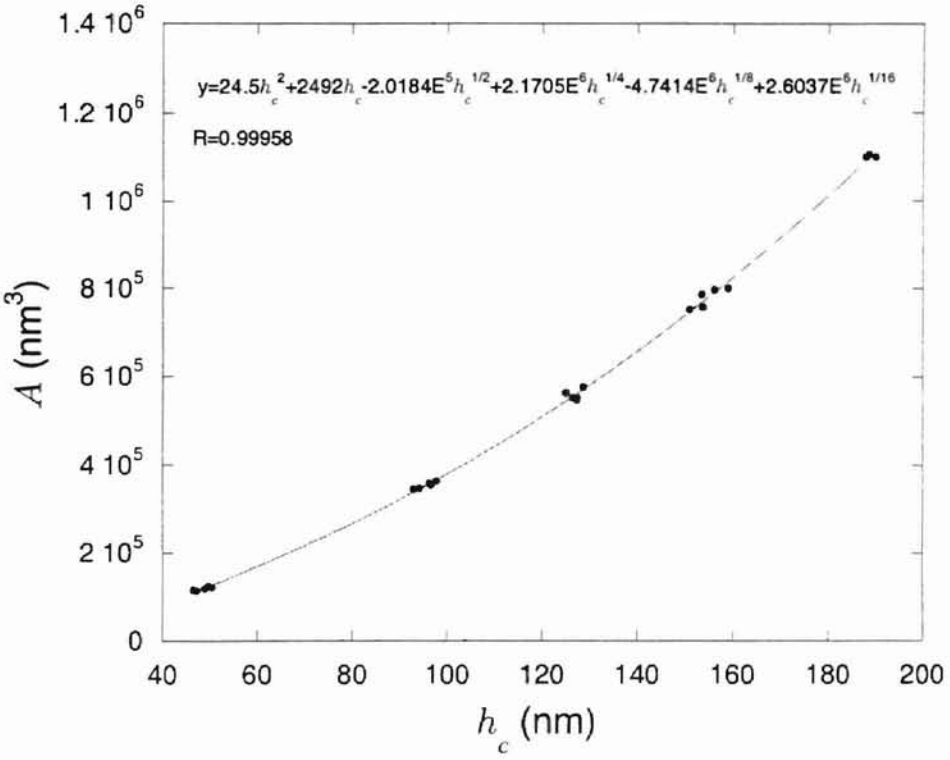

Figure A-3: Contact area vs. contact depth

and for the low load region, h_c = 4.8 - 47 nm are

$$\begin{aligned} C_1 &= 3.5173 \times 10^3 \\ C_2 &= -1.4112 \times 10^5 \\ C_3 &= 1.2712 \times 10^6 \\ C_4 &= -3.0037 \times 10^6 \\ C_5 &= 1.8792 \times 10^6 \end{aligned}$$

To confirm that the instrument was operating properly, an indentation into electropolished {100} aluminum was performed. and the results (E = 67.1 GPa) compared to those obtained of Oliver and Pharr [50] (E = 68.0 GPa). An example of a

load-displacement curve is shown in Fig. A-4.

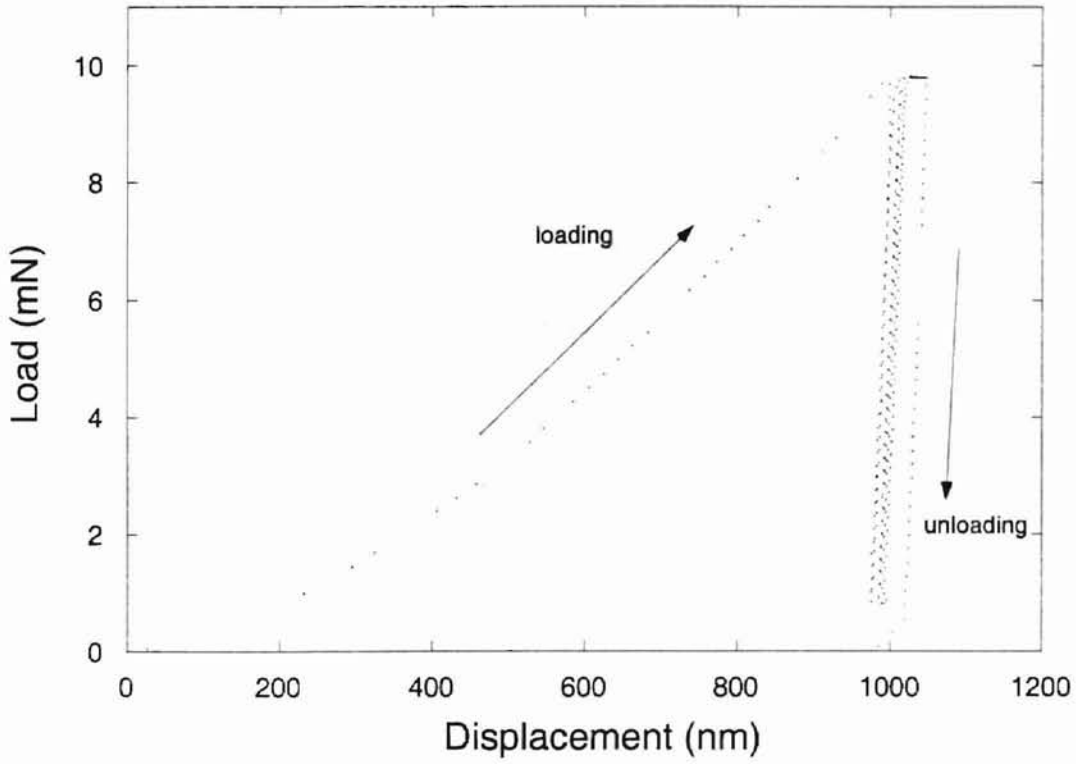

Figure A-4: Typical load-displacement of electropolished {100} aluminum

VITA 2

Rudy Ghisleni

Candidate for the Degree of

Master of Science

Thesis: INVESTIGATION OF THE SURFACE MECHANICAL PROPERTIES OF SINGLE CRYSTAL ZnO BY NANOINDENTATION

Major Field: Mechanical Engineering

Biographical:

Personal Data: Born in Osio Sotto, Bergamo, Italy on September 12, 1976, the son of Maurizio Ghisleni and Loredana Poli

Education: Graduated from I.T.I.S. "P. Paleocapa" High School, Bergamo, Italy in June 1995; attended 4 years of university in Italy before entering in a program of double degree: Laurea expected Summer 2002 from Politecnico di Milano, Milano, Italy, and Master of Science degree expected Summer 2001 from Oklahoma State University; Completed the requirements for the Master of Science degree with a major in Mechanical Engineering at Oklahoma State University in August, 2001.

Experience: Employed by Oklahoma State University, Department of Mechanical and Aerospace Engineering as graduate research assistant; Oklahoma State University, 2000 to present.

Professional Memberships: American Society for Precision Engineering; Honor Society of Phi Kappa Phi